INVESTIGATION INTO THE TRANSPORT PHENOMENA OF FERROFLUIDS IN SMALL-SCALE SYSTEMS

A thesis submitted
in partial fulfillment of the requirements
for the award of

Doctor of Philosophy

by

SUDIP SHYAM

DEPARTMENT OF MECHANICAL ENGINEERING
INDIAN INSTITUTE OF TECHNOLOGY GUWAHATI
GUWAHATI– 781039, INDIA
FEBRUARY 2021

DECLARATION

I, **Sudip Shyam**, would like to declare that the thesis titled "**Investigation into the Transport Phenomena of Ferrofluids in Small-scale Systems**" submitted to "**Indian Institute of Technology Guwahati**" for the degree of "**Doctor of Philosophy**" is a work of pure authenticity carried out under the supervision of **Dr. Pranab Kumar Mondal** and **Dr. Balkrishna Mehta**. To the best of my knowledge, the content of this thesis have not been submitted elsewhere for a degree. The contents of this thesis are free from any act of plagiarism. The investigations and observations reported in this thesis are carried out in the Department of Mechanical Engineering, Indian Institute of Technology Guwahati, during the period of July 2015 to May 2020.

Sudip Shyam
Research Scholar
Department of Mechanical Engineering
Indian Institute of Technology Guwahati
Guwahati-781039, Assam, India.

February 2021

CERTIFICATE

It is certified that the work contained in the thesis entitled "**Investigation into the Transport Phenomena of Ferrofluids in Small-scale systems**" by **Sudip Shyam** (Registration no. **156103017**) has been carried out under our supervision and that this work has not been submitted elsewhere for a degree.

Dr. Pranab Kumar Mondal
Assistant Professor
Department of Mechanical Engineering
Indian Institute of Technology Guwahati

Dr. Balkrishna Mehta
Assistant Professor
Department of Mechanical Engineering
Indian Institute of Technology Bhilai

February 2021

"Dedicated in loving memory of my father."

ACKNOWLEDGEMENT

Firstly, I would like to take this opportunity to express my earnest gratitude to my supervisors, Dr. Pranab K Mondal and Dr. Balkrishna Mehta, for accepting me as their Ph.D. student. Their continuous motivation, support, and guidance throughout my Ph.D. work helped me to continuously grow as a researcher. With every research meeting with Dr. Mondal, I felt motivated. His ability to face the incurred challenges with a never say no attitude, were the source of inspiration for me. Dr. Mehta's methodical way of guidance taught me how to develop an inquisitive mind and test every hypothesis from a scientific standpoint. I learned to struggle to get better and better every day by acquiring knowledge under their tutelage.

I am grateful to Dr. Asfer for his generous help during the course of my Ph.D. Discussion with him helped me in gaining in-depth knowledge of the μPIV measurement technique. I would like to thank my doctoral committee member, Prof. U. K. Saha, Dr. D. N. Basu, and Dr. R. Anandalakshmi, for their insightful comments and encouragement. The constructive inputs received from Dr. S. Mondal further helped me to grow intellectually. My sincere acknowledgment goes to Prof. A. Dass and Prof. S. K. Dwivedy, the former and present Head of the Mechanical Engineering department. I thank them for their encouragement, guidance, and support from the initial to final stages of my Ph.D. work.

I would also like to thank my labmates, especially Aritra, Rajkumar, Harshad, Abhijit, and Dr. Gorthi, for their constant technical and social support. My friends from Dibang hostel Ajit, Avnish, Bikash, Sambit, and many more have made my stay at IIT Guwahati memorable. Lastly, I am grateful to my mother, Mrs. Tapati Shyam, my brother Mr. Sankha Shyam, my sister in law Mrs. Puja Shyam, my beautiful niece Miss Sreeja Shyam, and my dear friend Himani. All of whom were a constant source of support and motivation in this endeavor.

Sudip Shyam

Indian Institute of Technology Guwahati

ABSTRACT

Ferrofluid is a type of magnetic liquid that is synthesized as a stable colloidal suspension of iron oxide particles in a carrier fluid. Ferrofluids have shown promising potential in several applications of emerging relevance, primarily due to its ability of being in control under the influence of a magnetic field. In the present study, some of the pertinent issues related to the transport phenomena of ferrofluid in small scale systems in the presence of a magnetic field are addressed. These include (a) exploring the thermal characteristics of ferrofluid flow in a heated channel in the presence of a constant and time-dependent magnetic field, (b) internal convections of a sessile ferrofluid droplet under the modulations of a time-dependent magnetic field, (c) mixing, and (d) evaporation characteristics of the ferrofluid droplet in a magnetically field-driven environment. All the problems as mentioned above have been systematically explored following comprehensive experimental techniques involving infrared thermography, bright field visualization, μPIV, and μLIF, respectively. Infrared thermography is performed for observing the thermal footprints of the ferrofluid flow. Bright field visualization is used to understand the qualitative behavior of the ferrofluid flow, while μPIV measurement is adopted for quantification of the internal flow dynamics. The experimental measurement technique consistent with μLIF is employed for quantification of the mass transfer occurring between fluids. In addition to that, numerical simulations have also been performed to support the experimental observations.

The prime focus of the first problem of interest is to gain deep insight into the energy transport characteristics of ferrofluid flow in a heated stainless steel tube under the influence of a constant and time-varying magnetic field. The study mainly focuses on the experimental investigations; however, to qualitatively support the experimental arguments, two-dimensional numerical simulations have also been performed. This study delineates the mechanism of augmentation of heat transfer through the interaction of available force fields, i.e., the interplay of magnetic force and inertia of the flow, and also discusses the effect of various time scales on the flow and thermal behavior. Major inferences of the study are (a) on the application of external magnetic (steady and time-dependent), heat transfer augments (b) there is a threshold frequency of external magnetic field at which the augmentation is maximum, and this frequency is the resultant outcome of advective time-scale and magnetic perturbation time-scale.

The second study reports the actuation of a sessile ferrofluid droplet over a hydrophobic substrate in the presence of a time-dependent magnetic field. During the ON cycle of the magnetic field, the bright field visualizations showed the migration of nanoparticles towards the contact line near the vicinity of the electromagnet, thus, resulting in aggregation of nanoparticles inside the droplet. Similarly, the aggregated nanoparticles are observed to disperse from the cluster during the OFF cycle of the magnetic field. Both migration and dispersion of nanoparticles result in a bulk motion inside the ferrofluid droplet during the ON and OFF cycle of the magnetic field. A critical frequency is observed beyond which a negligible dispersion of nanoparticles resulted inside the ferrofluid droplet during the OFF cycle of the magnetic field.

The third problem addressed in this thesis investigates the mixing of a ferrofluid droplet with a non-magnetic fluid in the presence of a time-varying magnetic field on an open surface microfluidic platform. The magnetic nanoparticles exhibit complex spatio-temporal movement inside the ferrofluid droplet domain under the influence of a time-dependent magnetic field, which, in turn, promotes the mixing efficiency in the convective mixing regime. Results demonstrate that the movement of magnetic nanoparticles in the presence of a time-periodic field strengthens the flow instability, which acts as an agent to initiate an augmented mixing in the present scenario. By performing numerical simulations, the onset of interfacial instability, mainly stemming from the susceptibility mismatch between the magnetic and non-magnetic fluids, has been reviewed and aptly demonstrated.

Finally, the evaporation kinetics of a sessile ferrofluid droplet in the presence of a time-dependent magnetic field is explored. The results showed that the droplet evaporation rate is augmented significantly in the presence of a time-dependent magnetic field, attributed primarily to the enhanced internal flow advection. The transient motion of the magnetic nanoparticles dictates the overall life-time of the evaporating ferrofluid droplet. At lower frequencies of the magnetic field, the magnetic nanoparticles move towards the magnet and agglomerates in a chain-like cluster formation, oriented according to the magnetic field lines. On the other hand, at higher frequencies, the magnetic nanoparticles do not possess sufficient time to travel the whole characteristics length (droplet diameter). Consequently, a critical frequency was found at which the perturbation time scale balances the advective time scale of the flow inside the droplet. On account of this balance between the time scales, the droplet experiences a minimum life-time. The evaporation kinetics of a ferrofluid droplet in the presence of a time-dependent magnetic field can be described through three distinguishable stages *viz*, the decreasing contact angle and variable radius zone (DCVR), the decreasing contact angle and decreasing radius zone (DCDR), and the late mixed zone.

Keywords: Ferrofluid, Magnetic field, Time-dependent, μPIV.

NOMENCLATURE

Abbreviation:

CMOS	Complementary metal oxide semiconductor
DCDR	Decreasing contact angle decreasing radius
DCVR	Decreasing contact angle varying radius
DI	De-ionized
DLS	Dynamic light scattering
FHD	Ferrohydrodynamics
FPS	Frames per second
IONP	Iron oxide nanoparticles
IR	Infrared
MHD	Magnetohydrodynamics
MNP	Magnetic nanoparticle
MP	Magnetophoresis
MR	Magnetoreheology
µ-PIV	Micro particle image velocimetry
µ-LIF	Micro laser induced fluorescence
PDMS	Polydimethylsiloxane
SS	Stainless steel
VSM	Vibration sample magnetometer

Notations:

$\bar{B}_r$	Remnant magnetic flux density (T)
$\bar{B}$	Magnetic flux density(T)
Bo	Bond number
Bo_m	Magnetic bond number
C	Concentration (mol/m^3)
C_p	Specific heat (J/kg K)
C_d	Drag coefficient
D^*	Non-dimensional dimaeter
D_h	Hydraulic diameter (m)
D_0	Initial diameter of the droplet (m)
F_d	Drag force (N), $F_d = 3\pi\eta D_p\left(U_p - U_{ff}\right)C_d$ (N)

F_g	Gravity force (N/m^3)
F_m	Magnetic force (N/m^3)
F_s	Surface tension force (N/m^3)
F_{mp}	Magnetophoresis Force (N), $F_{mp} = -V\mu_0(M \cdot \nabla H)H$ (N/m^3)
f	Frequency (Hz)
H^*	Non-dimensional height
$\bar{H}$	Magnetic field (A/m)
H_0	Initial height of droplet (m)
h	Heat transfer coefficient (W/m^{2}K)
I	Current (A)
J_e	Current density (A/m)
k	Thermal conductivity (Wm^{-1}K^{-1})
m	Moment (A-m^{-2})
$\bar{M}$	Magnetization (emu/g)
N	Number of turns
NA	Numerical Aperture
Nu	Nusselt number
q''	Heat flux (W/m^2)
Q_l	Heat lost (W)
U_{MNP}	Velocity of magnetic nanoparticles (m/s)
u_{cl}	Contact line velocity (m/s)
U_{max}	Maximum velocity (m/s)
U^*	Non-dimensional velocity
R	Radius of droplet (m)
Re	Reynolds number
T^*	Non-dimensional temperature
$\bar{T}$	Non-dimensional mixing time
T	Temperature (K)
T_0	Mixing time in the absence of an external field
T_E	Droplet evaporation time

T_M	Mean temperature (K)
T_W	Wall temperature (K)
T^*	Non-dimensional temperature
t	Time scales
t_m	Perturbation time scale
t_u	Advective time scale
t_v	Viscous time scale
V_0	Initial volume of the droplet (m^3)
V	Velocity components in y (m/s)
V^*	Non-dimensional volume
X^*	Non-dimensional axial length
X	Non-dimensional axial direction
Y	Non-dimensional transverse direction

Greek symbol:

α	Thermal diffusivity (m^2/s)
β	Thermal expansion coefficient (1/K)
η	Dynamic viscosity (Ns/m^2)
φ	Volume fraction
γ	Surface tension (N/m)
ρ	Density (kg/m^3)
μ_0	Permeability of free space (1.2566×10^{-6} m kg $s^{-2}A^{-2}$)
μ	Permeability (m kg s^{-2} A^{-2})
σ	Electrical conductivity of coil (s/m)
ζ	Non-dimensional time of operation of a magnetic field
θ^*	Non-diemnsional contact angle
θ	Contact angle (°)
χ	Magnetic susceptibility
$\psi(x,y)$	Cross-correlation function

ω_y Vorticity $(1/s)$, $\omega_y = \left(\frac{\partial w}{\partial x} - \frac{\partial u}{\partial z}\right)$

Subscript:

cr	Critical
e	Evaporation
eps	Electrostatic
ff	Ferrofluid
g	Gravity
nm	No magnet
m	Magnetic
mp	Magnetic particle
u	Advective
S	Surface tension
v	Viscous
vps	Vandar-waals

Non-dimensional number:

Bo	Bond number $(\rho g D_h^2/\gamma)$
Bo_m	Magnetic bond number $(\mu_0 \lvert H^2 \rvert R/\gamma)$
D^*	Non-dimensional diameter (D/D_0)
H^*	Non-dimensional height (H/H_0)
Nu	Nusselt number $(h \cdot D_h/k)$
θ^*	Non-dimensional contact angle (θ/θ_0)
Pr	Prandtl number $(\eta \cdot C_p/k)$
$\bar{T}$	Non-dimensional mixing time (t/T_0)
T^*	Non-dimensional temperature $\left(T - T_{ffi}\right)/q'' \cdot D_h/k_{ff}$
t^*	Non-dimensional time (t/T_E)
t_α	Diffusion time scale (D_h^2/α)
t_m	Perturbation time scale $(1/2f)$
t_U	Advective time scale (D_h/U)
t_v	Viscous time cale (D_h^2/v)

Re	Reynolds number$(\rho \cdot U \cdot D_h/\eta)$
V^*	Non-dimensional volume (V/V_0)
U^*	Non-dimensional velocity (U/U_{max})
We_m	Magnetic Weber number $(\mu_0 \lvert M^2 \rvert U/\gamma\, A_s)$
X^*	Non-dimensional axial length $(x/Re \cdot Pr \cdot D_h)$
X	Non-dimensional axial direction (x/D_h)
Y	Non-dimensional transverse direction (y/D_h)

LIST OF FIGURES

LIST OF TABLES

CONTENTS

Chapter 1

INTRODUCTION

Controlled manipulation of the fluid flow field is critical for a variety of engineering applications such as passive pumping, mixing, electronic cooling, chemical reactions, bioassays, and many more. A fluid flow domain can be actively regulated by employing a variety of approaches such as the utilization of magnetic force, electric force, acoustic force, light energy, and many more. In this chapter, the importance of magnetofluidics is outlined, followed by a general introduction of ferrofluid. In the next section, a brief review of the literature pertaining to the transport characteristics of ferrofluid in the presence of a magnetic field is discussed. Finally, the research gaps, aim, and outline of the present thesis are delineated based on the conclusions drawn from the review of the literature.

1.1 BACKGROUND

In modern technologies, a flow domain, especially in the micro/nanoscale, is mostly regulated by employing various external forcing such as electric, optic, acoustic, and magnetic forces. Efforts on the explorations of implications of magnetofluidics are rare compared to electrofluidics, optofluidics, and acoustofluidics. While the fact is true that we can have precise control of the flow phenomena using the electric/optic/acoustic field, but magnetic fields have some serious advantages over the electric/optics/acoustic-based manipulation technique. The electric field is very sensitive to contamination, and also it has an inevitable issue of Joule heating effect. At the same time, the optical/acoustic concept requires expensive external systems. In contrast, manipulation of the flow field via a magnetic field is cheap, independent of any surface charges/ion concentration alterations, and in most cases, does not induce any heating. Due to these mentioned reasons, manipulation of fluid flow in miniaturized fluidic domains using magnetic forces has attracted growing interest among researchers in recent years (Ganguly et al. 2004; Zhu et al. 2011; Zhu and Nguyen 2012; Nguyen 2012). The term magnetofluidics traditionally refers to the case when an external magnet is used to regulate/manipulate the flow. Researchers have explored the flexibility of magnetofluidics in a variety of engineering applications such as sensing, actuation, mixing,

passive pumping, heat transfer enhancement, and many more (Ganguly et al. 2004; Zhu and Nguyen 2012; Nkurikiyimfura et al. 2013; Manukyan and Schneider 2016; Ray et al. 2017).

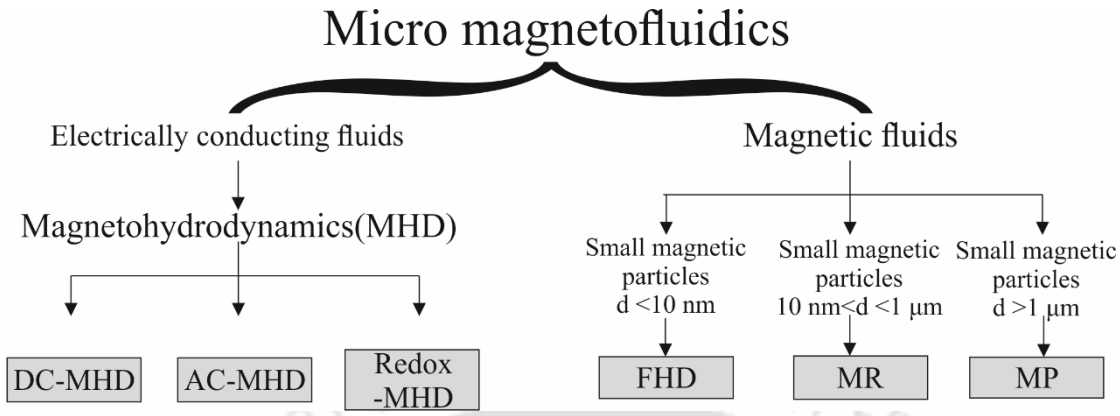

Fig. 1.1 Schematic depicts the classification of micro-magnetofluidics and its representative applications (Nguyen 2012)

The paradigm of magnetofluidics, precisely micro-magnetofluidics, can be classified according to the type of fluid used as magnetohydrodynamics (MHD), ferrohydrodynamics (FHD) magnetorheology (MR), and magnetophoresis (MP), as can be seen from Fig. 1.1 (Nguyen 2012). In magnetohydrodynamics (MHD), the working fluid is electrically conducting. When the magnetic fluid is electrically non-conducting, magnetofluidics can be further classified into three subgroups depending on the size of magnetic nanoparticles in the carrier fluid. If the size of the magnetic nanoparticles is less than 10 nm, it is referred to as ferrohydrodynamics. For such cases, the thermal energy of the particles dominates over the magnetic energy, and the fluid possesses paramagnetic nature. These types of magnetic fluids are mainly referred to as ferrofluid. While for the particle size greater than 10 nm and less than 1 μm, the fluid is referred to as magnetorheological fluid. As such, the large enough size of the particles ensures a steady reaction to an external magnet, thereby changing the viscosity of the fluid. For the particle sizes of few orders of microns, the particles should be treated as an individual entity, leading to a separate paradigm altogether and known as magnetophoresis.

1.2 FERROFLUID: GENERAL INTRODUCTION

The branch in science which deals with ferrofluids is known as ferrohydrodynamics (Rosensweig 1984; Odenbach 2002; Stefan Odenbach 2006). Ferrofluid is a stable colloidal suspension of magnetic particles in a non-magnetic carrier fluid. These particles are coated with a stabilizing dispersion agent, i.e., a surfactant, which prevents agglomeration of the nanoparticles by virtue of steric repulsion, as shown in Fig. 1.2 (Stefan Odenbach 2006).

The magnetization of ferrofluid is dependent on the applied magnetic field flux density and its thermophysical properties. Thus, a change in any of these quantities changes the body force distribution in the fluid and, eventually, giving rise to convections in the flow domain under the influence of a non-uniform magnetic field. Ferrofluid usually does not retain any magnetization, and thus, often is classified as superparamagnetic fluid.

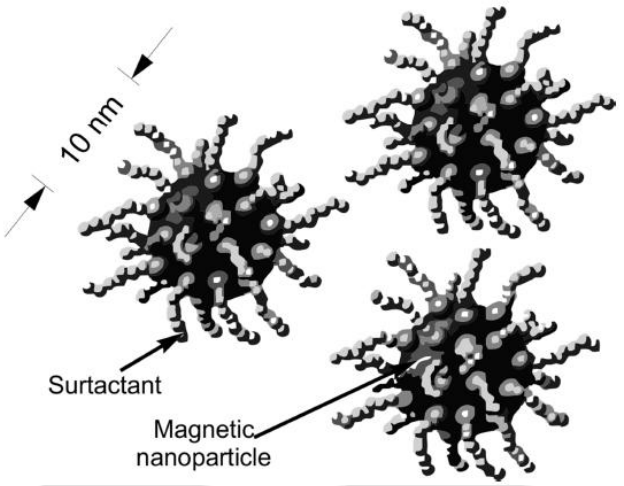

Fig. 1.2 Magnetic nanoparticles with surfactant (Stefan Odenbach 2006)

1.3 APPLICATION OF FERROFLUID

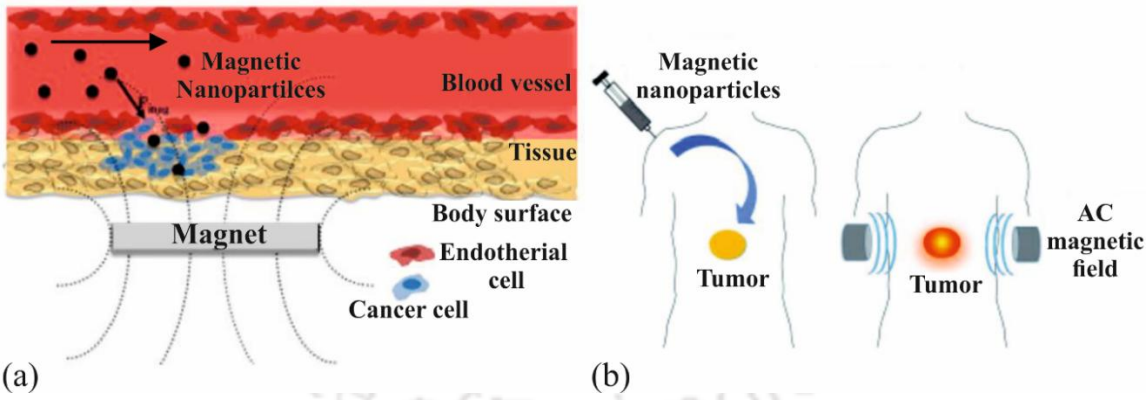

Fig. 1.3 (a) Transportation of drug-loaded magnetic nanoparticles (MNPs) to the cancer cell through the endothelial layer during magnetic drug targeting (MDT) (Grillone and Ciofani 2017); (b) Generation of heat from magnetic nanoparticles (MNPs) in the presence of AC magnetic field during magnetic hyperthermia (Andrade et al. 2011).

The prospect of precise control of flow has led to the development of a wide variety of possible applications of these liquids in various fields ranging from mechanical engineering to biomedical engineering. Ferrofluid has been extensively used as liquid seals around the spinning drive shafts of the hard disk. Because of its friction-reducing capacity, ferrofluids find applications in semi-active and passive dampers. They are commonly used in

loudspeakers to remove heat from the voice coil and passively dampen the movement of the cone. In the biomedical application, ferrofluids are used as contrast agents in Magnetic Resonance Imaging. Research is also going on to explore the suitability of ferrofluid in targeted magnetic hyperthermia and magnetic drug targeting. Figure 1.3 shows the schematic representation of magnetic drug targeting and magnetic hyperthermia.

1.4 MOTIVATION FOR THE PRESENT WORK

The present work attempts to address a few questions related to the energy, momentum, and species transport of ferrofluid in the presence of a magnetic field. The primary focus of the research is to explore the characteristics of the thermohydrodynamic behavior of ferrofluid when perturbed by a magnetic field. The rationale behind this topic is the tremendous potential of ferrofluid for non-invasive flow manipulation and heat transfer enhancement. Maintaining the primary theme of the work, we divide the overall study into four individual objectives. Firstly, we explore the role of ferrofluid in heat transfer augmentation under the influence of a steady and time-dependent magnetic field. In the next part of the work, we investigate the dynamics of the internal convections generated inside the ferrofluid flow field in the presence of a magnetic field.

The third part of the report explores the mixing characteristics of the ferrofluid droplet with another non-magnetic droplet under the modulations of a time-varying magnetic field. The last part of the work deals with understanding the implications of the generated convective patterns of the ferrofluid droplet domain on its evaporation characteristics. Albeit, the flow dynamics of ferrofluid in the presence of a magnetic field have been explored in the past. However, a clear picture of its transport characteristics is still lacking. For instance, the role of the various time scales on the thermal and hydrodynamic behavior of the flow is hardly explored. Moreover, the internal convective features of ferrofluid, as modulated by a magnetic field, demand an extensive investigation. Also, the role played by these maneuvered internal dynamics on the overall lifetime of the droplet has remained to be answered as well. In this dissertation, an attempt is made to explore all these unanswered questions through experimental investigations, supported by numerical simulations.

1.5 LITERATURE REVIEW

Ferrofluid is a suspension of ferri/ferro magnetic particles ranging from 5 to 15 nm in a suitable carrier fluid. This fluid is considered as a new class of smart fluid whereby fluid properties can be altered using an external magnetic field. This smart fluid was invented at a

lab in NASA by Steven Pappel while controlling and directing liquid rocket fuel in outer space. Pioneer work in this domain was done by Rosensweig (1988) decades back. He worked on the synthesis of the stable colloids and began commercial utilization of ferrofluid in 1968. Traditional usage of ferrofluids, as already mentioned (see Section 1.3), were limited to multistage rotary seals, exclusion seals, inertia dampers, loudspeakers, to name a few. The main advantage of ferrofluid is that they possess magnetic properties comparable with ferromagnetic particles and flowability like any other fluids. These unique properties ensure effective control of the fluid flow by the application of an external magnetic field. Owing to these advantageous features, ferrofluids have shown promising potential in various engineering fields such as mechanical, thermal, and biomedical related applications (Hiergeist et al. 1999; Nakatsuka et al. 2002; Shuchi et al. 2005; Philip et al. 2007).

In 'Section 1.4', the global motivations of the studies addressed in this thesis as the exploration of the transport (energy, momentum, and species) characteristics of ferrofluids under the influence of an externally applied magnetic field in small-scale systems are outlined. In this section, we present a contextual literature review pertaining to the primary theme of the present work. The summarized review of the state of the art literature are presented in the following broad categories:

- Thermal characteristics of ferrofluid in the presence of a magnetic field
- Internal hydrodynamics of a ferrofluid droplet as modulated by a magnetic field.
- Magnetically actuated micromixing.
- Evaporation of a ferrofluid droplet in a magnetic forcing ambiance.

1.5.1 Thermal characteristics of ferrofluid in the presence of a magnetic field

The transport of energy and momentum in miniaturized devices is limited because of the flow being predominantly laminar. Several heat transfer augmentation techniques were developed over the years (Tuckerman and Pease 1981; Bau et al. 2001; Oddy et al. 2001). Among these several methods, the one that showed promising results and had good practical suitability is the use of nanofluid for heat transfer enhancement. Numerous experimental and numerical studies have been conducted by studying the transport phenomena of different nanofluids in miniaturized fluidic pathways (Pak and Cho 1998; Wang and Mujumdar 2007; Godson et al. 2010; Roy et al. 2012; Shaker et al. 2014). Many of these studies have focused on a particular type of magnetic nanofluid, also known as a ferrofluid, which can be manipulated under the influence of a magnetic field.

On perturbation by a magnetic field, the physical properties of ferrofluid get altered. Due to this unique feature, ferrofluid finds application in various fields such as bioengineering, electronic packing, and thermal engineering, to name a few (Rosensweig 1984; Hiergeist et al. 1999; Nakatsuka et al. 2002). It is worth mentioning here that following both the experimental as well as numerical investigations; several researches have explored as well as established the promising potential of ferrofluid as a means for heat dissipation (Ganguly et al. 2004; Shuchi et al. 2005; Xuan et al. 2007; Wright et al. 2007; Philip et al. 2007; Parekh and Lee 2010; Lajvardi et al. 2010; Gavili et al. 2012; Şeşen et al. 2012; Aminfar et al. 2013).

Ganguly et al. (2004a) numerically investigated the convective heat transfer enhancement of single-phase ferrofluid flow under the action of magnetic line dipoles. Constant temperature boundary conditions were applied to the walls of the channel. Local vortex was observed near the cold wall primarily due to the asymmetry in the thermal boundary layer and spatial non-uniformity in the magnetic susceptibility (temperature dependant) of ferrofluid (Fig. 1.4). Augmentation in the energy transport of the flow field was observed mainly due to the presence of the recirculation zone. The heat transfer augmentation also depends on the net magnetizing current and relative placement of the line dipoles. Philip et al. (2007) and Gavili et al. (2012), in their investigations, have shown that the thermal conductivity of ferrofluid changes by 300 % and 200 %, respectively, under the influence of a magnetic field.

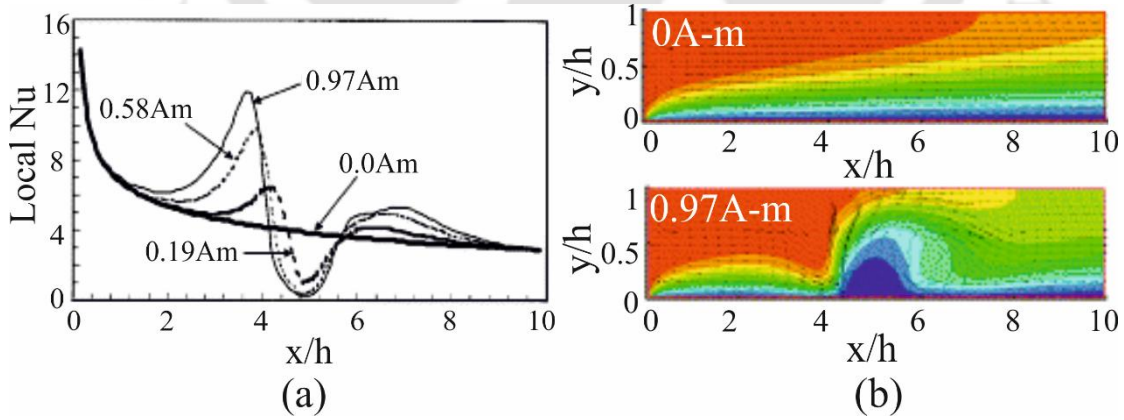

Fig. 1.4 (a) Variation of the local Nusselt number along the length of the channel in the presence of a magnetic field,(b) Distribution of the non-dimensionalized velocity and temperature profiles for channel flow in the presence and absence of magnetic field. (Ganguly et al. 2004)

Although the reported literature showed enhancement in heat transfer characteristics, the mechanism of heat transfer has remained a debatable issue. Azizian et al. (2014) explored the heat transfer characteristics and pressure drop of magnetite nanofluid in the laminar flow

regime (Re<830) under the effect of external magnetic fluid. The authors explored the role of magnetic field strength, gradients, and magnet configurations on the underlying transport of heat. Substantial enhancement in heat transfer was observed at high magnetic field strength. As reported, the augmentation in heat transfer gets further amplified at higher Reynolds numbers. They attributed the reason behind this augmentation in heat transfer to the accumulation of nanoparticles at the walls nearby the vicinity of the magnet. This agglomeration of nanoparticles further increases the local thermal conductivity of the fluid, and thereby, enhancing the overall magnitude of heat transfer. Also, as reported, the agglomeration kinetics and the fluid flow profile have a contributory effect on the convective heat transfer augmentation.

Asfer et al. (2016a) experimentally investigated the ferrofluid flow phenomena in a heated stainless steel tube in the presence of permanent magnets. They reported that magnetic force could have a supportive or resistive effect on convective heat transfer depending on the (a) ratio of the inertia force/magnetic force, and (b) the interaction of the ferrofluid aggregate deposited at the wall (adjacent to the magnetically active region) with the bulk fluid flow. It was shown that ferrofluid, under the influence of a magnetic field, forms a chain-like structure, thereby enhancing its thermal conductivity (as shown in Fig. 1.5).

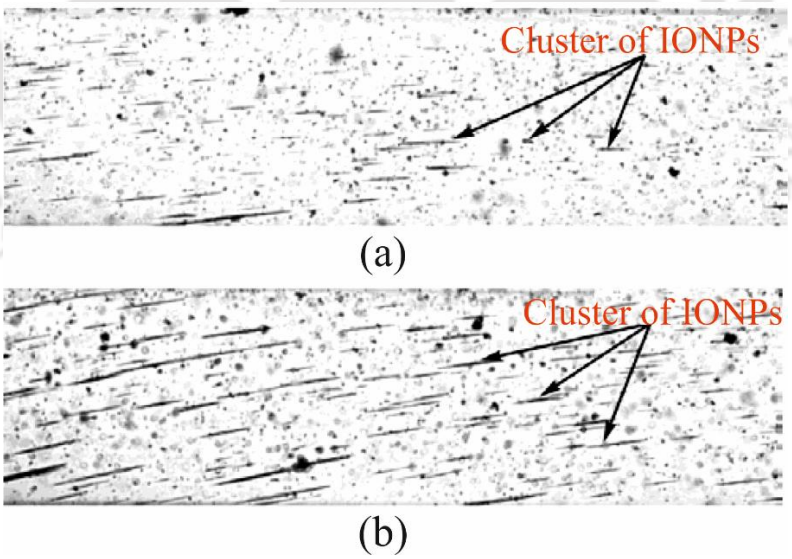

Fig. 1.5 Clustering of iron oxide nanoparticles (IONPs) within the ferrofluid in the presence of a magnetic field from bright-field microscopic visualization, when the magnetic field flux density ($\bar{B}$) is maintained as: (a) $\bar{B} = 0.1\,T$, and (b) $\bar{B} = 0.2\,T$ (Asfer et al. 2016)

While most of the reported investigations were pertained to constant magnetic field case, very sparse literature are available where the effect of time-dependent magnetic field on convective heat transfer is explored. A few researchers have shown enhancement in the heat

transfer coefficient when the ferrofluid flow domain was perturbed by a time-dependent magnetic field (Murray 2008; Goharkhah and Ashjaee 2014; Goharkhah et al. 2015b, 2016; Yarahmadi et al. 2015). Murray (2008) experimentally explored the implication of a time-varying magnetic field on the ferrofluid flow in a heated channel. The author showed that the heat transfer coefficient increases by 267 % in the presence of a time-varying magnetic field. Goharkhah et al. (2015, 2016) studied the laminar convective heat transfer characteristics of ferrofluid flow in a heated tube under the influence of both constant and time-dependent magnetic fields following experimental investigations and numerical simulations. On the application of a steady and time-dependent magnetic field, the overall augmentation in the heat transfer coefficient increases by 24.9% and 37.3%, respectively (when compared to the base case of convective flow without magnetic field). Singh et al. (2018**)** numerically studied the convective heat transfer characteristics of ferrofluid flow under the influence of a steady and time-varying magnetic field. They observed that on perturbation by a constant magnetic field, the heat transfer augmentation is primarily due to the presence of the recirculation zone. However, when the time-varying magnetic field disturbs the flow field, the underlying mechanism of heat transfer enhancement depends on the interplay between the involved time scales in the flow domain.

1.5.2 Internal hydrodynamics of a ferrofluid droplet as modulated by a magnetic field

Controlled actuation of droplets on a planar surface using different actuation parameters such as electrostatic forces (Pollack et al. 2002; Velev and Bhatt 2006), thermocapillary (Ting et al. 2006), acoustics (Cheung and Qiu 2011), and magnetism (Beyzavi and Nguyen 2009; Tan et al. 2010) have been the subject of theoretical and experimental investigations among the researchers for the last decade. Compared to different actuation concepts, droplet manipulation using magnetism offers several advantages. Droplets can be manipulated from a safe distance using a magnetic field in a non-invasive manner. Furthermore, magnetic field-based manipulations are relatively more tolerable to changes in liquid properties. On the contrary, electric field-based manipulation is highly dependent on the conductivity and permittivity of the working fluid (Zhang and Nguyen 2017). Ferrofluid, for its superparamagnetic nature, has been a viable option for the magnetic field-based manipulation of droplets. The presence of iron oxide nanoparticles in ferrofluid provides the ability to control/actuate the flow under the influence of a magnetic field. Due to its superparamagnetic characteristics, in the absence of a magnetic field, the magnetic nanoparticles are randomly

oriented, with the overall magnetization of ferrofluid being zero. However, with the application of a magnetic field, the nanoparticles in ferrofluid exhibit a magnetic moment oriented in the direction of the applied magnet.

Over the past decade, several studies related to ferrofluid based mixing (Tsai et al. 2009; Fu et al. 2010; Zhu and Nguyen 2012; Kitenbergs et al. 2015; Varma et al. 2016; Maleki et al. 2019), spreading/wetting on a substrate(Ahmed et al. 2018a, b; Souza et al. 2019), evaporation or drying pattern (Jadav et al. 2017; Saroj and Panigrahi 2019) in the presence of magnetic field are reported in the literature. The hydrodynamics of ferrofluid in the presence of the magnetic field plays an important role, where the magnetic nanoparticles migrate in the direction of the applied magnetic forcing, which in turn induces a flow known as magnetoconvetion inside the fluid. This magnetoconvection may result in enhanced mixing between fluids or controlled spreading/evaporation of ferrofluids under the modulations of a magnetic field.

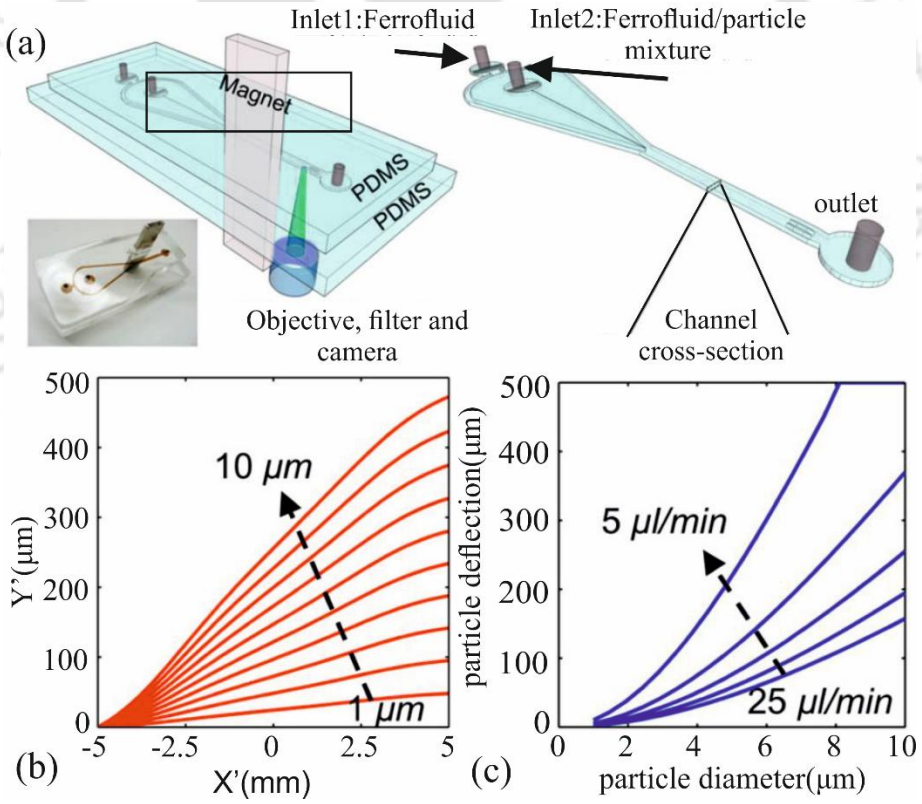

Fig. 1.6 (a) Schematic representation of the microfluidic system with a permanent magnet and a microchannel. Non-magnetic microparticles and ferrofluid mixture were introduced into the microfluidic channel Inlet 2 and hydrodynamically focused by the ferrofluid sheath flow from Inlet 1; (b) Simulated trajectories of particles in the microchannel at a constant flow rate of 5 μl/min. (c) Simulated deflections of particles from the inlet to the outlet at different flow rates when the particles are at the center-plane of the microchannel (Zhu et al. 2011).

Quantitative measurements of convection or velocity of nanofluids (e.g., ferrofluids) can be obtained experimentally using either μ-PIV or PTV technique. The μ-PIV technique provides the velocity information by tracing seeding particles added to nanofluid, whereas the PTV technique provides the velocity information by tracing the individual nanoparticles of nanofluid. Very few studies related to velocity measurements of nanofluids using μ-PIV or PTV technique are available in the literature (Yang et al. 2007; Etgar et al. 2010; Walsh et al. 2010; Anoop and Sadr 2012). Anoop and Sadr (2012) studied the near-wall velocity measurements of nanofluids (silicon dioxide particles of 10 to 20 nm in water) using nano-Particle Image Velocimetry (nPIV). The authors reported the near-wall velocity to be similar to that of the base fluid, i.e., water. Walsh et al. (2010) carried out a μ-PIV investigation of nanofluids through a clear-walled Teflon tube and reported normalized velocity profiles for different volumetric concentrations of nanofluids. The authors reported good agreement with the analytical model predicted by the Hagen-Poiseuille theory for the flow of nanofluids. A few literatures are available on the experimental quantification of flow patterns of nanofluids; detailed measurement of the flow pattern of ferrofluid at the microscale is very sparsely explored.

Nguyen et al. (2005) carried out a μ-PIV study of oil-based magnetic fluid in a PMMA microchannel in the presence of a permanent magnet. They reported the vector field in the middle and near the wall of the channel. However, during the measurements, the negative magnetophoresis acting on the seeding particles in the magnetic fluid resulting from the magnetic field produced by the permanent magnet was not considered. Yang et al. (2007) reported the motions of magnetic nanoparticles under the external magnetic field produced by a permanent magnet in a rectangular microchannel (500 × 500 μm^2 cross-section, 54 mm long), using particle tracking velocimetry (PTV).

For flow field measurements using μ-PIV, tracers, or seeding particles are first added to the fluid, and then the measurements were taken by illuminating the whole flow domain. The seeding particles are, in general, non-magnetic in nature and faithfully follow the fluid. However, non-magnetic particles such as the seeding particles, when placed in a diluted ferrofluid subjected to a magnetic field, behave as particles with negative susceptibility and exhibit negative magnetophoresis analogous to buoyancy in a gravitational field (Černák et al. 2004). Hence the assumption of seeding particles following the fluid during μ-PIV measurements doesn't hold good in the case of measurement of a magnetic fluid in the presence of a magnetic field. Zhu et al. (2011) carried out both analytical and experimental

studies on the transport of non-magnetic particles in ferrofluid under the influence of a permanent magnet. They reported greater deflection of the particles in the direction away from the magnet with either increasing size of the particles or decreasing the flow rate of ferrofluid through the microchannel (see Fig. 1.6).

1.5.3 Magnetically actuated micromixing

With the advent of miniaturization, droplet-based microfluidics, which is ubiquitous in protein crystallization, biosensor, immunoassays, DNA-replication, cell-based assays, biomolecular extractions, to name a few, has emerged as an effective approach for precise manipulation of a discrete volume of fluid samples and analytes in recent years (Berry et al. 2011; Bogojevic et al. 2012; Mary et al. 2008; Shamsi et al. 2014; Tice et al. 2003; White et al. 2013; Zhang et al. 2011). One promising application of droplet-based microfluidics finds enormous relevance to the micro-mixing technology, typically used in on-chip biochemical and biological analysis. The paradigm of droplet-based micromixing can be classified into two different types, namely open surface, and closed surface micromixing. Open surface droplet-based micromixing offers a few advantages over the closed surface microfluidic environment, such as simple fabrication, interfacial convenience, and free of any blockage such as bubble clogging (Long et al. 2009; Lin et al. 2017). Droplet-based mixing in the open surface microfluidic platform can be accomplished using two approaches viz., passive approach, and active approach. The passive approach entirely sticks to the molecular diffusion between the phases to be mixed and can be tuned by altering the surface morphology (for example, patterned wettability controlled surface) towards achieving the desired controllability (Xing et al. 2011; de Groot et al. 2016). While the active approach, which is more prevalent due to its reconfigurable flexibility, primarily relies on external force fields such as electric field, magnetic field, acoustic waves, and light energy for maneuvering the droplet flow field (Shang et al. 2017).

Of all these active approaches, utilization of the magnetic field has evolved as a promising technology in the paradigm of droplet-based mixing in microfluidic platforms, attributed primarily to its inherent advantageous features. A few such notable features include biocompatibility, ease of incorporation, low cost, less invasive, no induction heating, precise manipulation of the contact line, and many more (Nguyen 2012; Zhang and Nguyen 2017; Huang et al. 2017; Liu et al. 2018). It is worth mentioning here that researchers have exploited the flexibility of magnetic manipulation in the open surface microfluidic framework for achieving controlled mixing (Biswal and Gast 2004; Franke et al. 2009; Lee et al. 2009; Roy

et al. 2009; Martin et al. 2009; Sing et al. 2010; Vilfan et al. 2010). Ferrofluid is a colloidal suspension of nanoparticles in a non-magnetic carrier medium (Rosensweig 1984; Odenbach 2002). The nanoparticles are usually stabilized by surfactants such that they exhibit continuum behavior in the presence of a strong magnetic field. The rapid response of the nanoparticles to the magnetic field offers tremendous flexibility in stirring/mixing related applications in lab-on-a-chip (LOC) systems (Wang et al. 2008; Tsai et al. 2009; Zhu and Nguyen 2012; Hejazian et al. 2016; Nouri et al. 2017).

Zhu and Nguyen (2012a) explored both numerically and experimentally, the mixing phenomena of a magnetically active fluid in a microfluidic chamber in the presence of a uniform magnetic field. The authors reported that the application of magnetic field ensures magnetization mismatch, resulting in the development of flow instabilities, and the consequence of this phenomenon results in an enhanced mixing. The authors discussed critical parameters such as magnetic flux density, flow ratio, viscosity ratio, etc., on the mixing efficiency.

The flow instability gets further aggravated under the influence of the time-periodic magnetic field owing to the various involved spatio-temporal scales such as advective time scale, viscous time scale, perturbation time scale, and many more. It may be mentioned in this context here that a few researchers have explored the implications of the time-periodic magnetic field on the mixing characteristics between two fluids as well (Wang et al. 2008; Wen et al. 2009). Wang et al. (2008) explored the performance of a magnetic particle-driven micromixer. The time-periodic magnetic field perturbs the flow domain by ensuring transient disturbances in the flow domain. The effect of magnetic force, actuation frequency, and channel geometry are explored. Figure 1.7 shows the micromixer configurations and also the variation of the average mixing efficiency for the various magnetic field frequencies. Authors (Wang et al. 2008) have shown that the critical frequency of the magnetic field depends on the lateral dimensions of the micromixer and the applied magnetic force.

Albeit several underlying issues of the magnetic field modulated micromixing analysis have been well explored, see Refs. (Wang et al. 2008; Roy et al. 2009; Tsai et al. 2009; Wen et al. 2009; Zhu and Nguyen 2012; Gao et al. 2015; Hejazian et al. 2016; Munaz et al. 2017; Nouri et al. 2017), the phenomenon of magnetophoresis, which is effectively used in manipulating microflows, on the droplet-based micromixing is sparsely studied. It may be mentioned in this context here that in the paradigm of droplet-based mixing, the rotating magnetic field has been used in a synergetic way for augmenting the mixing appreciably (Roy

et al. 2009; Gao et al. 2015; Munaz et al. 2017). Roy et al. (2009) investigated the role of magnetic stirring on a sessile droplet in the presence of a rotating magnetic field. Magnetic stirring occurs as a consequence of the self-assembled chains of the magnetic microspheres in the presence of a rotating magnetic field. They parametrically explored the role of fluid viscosity, magnetic microsphere loading, magnetic field, RPM. A critical Mason number was observed at which maximum mixing was taking place.

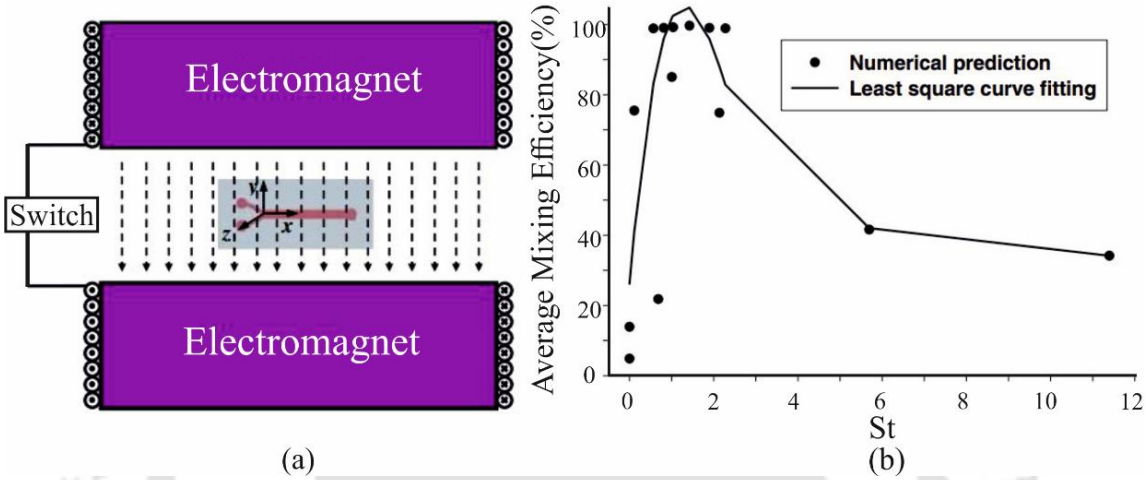

Fig. 1.7 (a) Schematic represents the micro-mixer along with the electromagnets. (b) Plot depicts the variation of the average mixing efficiency for the various Strouhal number (St) (Wang et al. 2008).

1.5.4 Evaporation of a ferrofluid droplet in a magnetic forcing ambiance

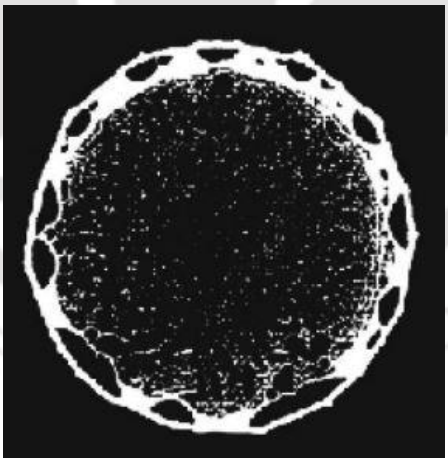

Fig. 1.8 Plot depicts the deposits of a drop containing microspheres, dried in an open atmosphere (Deegan 2000).

Evaporation of colloidal liquid has attracted significant attention to the researchers owing to its wide range of engineering applications such as surface patterning, drug delivery, coating technology, ink-jet printing, electronic cooling, to name a few (Chon et al. 2007; Brutin et al. 2011; Erbil 2012; Sefiane 2014). As explored by a series of experimental investigations, when a colloidal droplet containing nanoparticles evaporates, capillary flow is

induced in the droplet domain (Deegan et al. 1997, 2000; Deegan 2000). It is worth mentioning here that because of this capillary flow, the particulates are drawn towards the droplet periphery, leading to the formation of the famous coffee ring pattern, as can be seen from Fig. 1.8. The coffee ring pattern, which is a ring-like deposition at the droplet periphery, is undesirable in many engineering processes. Note that the formation of a coffee ring pattern is an unsought phenomenon for controlled evaporation kinetics as well. Considering this aspect, researchers have investigated different ways to suppress the coffee ring formation (Eral et al. 2011; Yunker et al. 2011; Mampallil et al. 2012; Das et al. 2017). It is essential to mention here that the presence of nanoparticles leads to an enhancement in the evaporation kinetics of the nanofluid droplet, attributed mainly to the pinning of the three-phase contact line by the nanoparticles. As reported in the literature, this augmented evaporation decreases the overall life-time of the droplet (Moffat et al. 2009; Orejon et al. 2011).

As already discussed, ferrofluid is a colloidal suspension of magnetic nanoparticles coated with surfactant and dispersed within a carrier liquid. In the presence of a magnetic field, the dispersed nanoparticles align themselves with the applied field, giving a magnetic response. However, when the magnetic field is removed, the Brownian motion rapidly scatters the aligned nanoparticles, eliminating the chance of permanent magnetization and rendering superparamagnetic characteristics to the fluid (Neuringer and Rosensweig 1964; Rosensweig 1984; Müller and Liu 2001; Odenbach 2002; Hernández-Contreras and Ruíz-Estrada 2003; Elfimova et al. 2013). Note that because of this feature, ferrofluid is widely used in many industrial applications such as cell separation (Saliba et al. 2010; Hejazian et al. 2015), chemical synthesis (Ferraro et al. 2015), droplet generation, and breakup (Wu et al. 2013),(Katsikis et al. 2015; Zhang and Nguyen 2017) electronic cooling,(Ganguly et al. 2004; Goharkhah and Ashjaee 2014), etc. In spite of these wide ranges of real-time engineering applications, research endeavors focusing on the evaporation of this magnetically active fluid in the presence of the magnetic field remains sparsely explored. Important to mention, in a colloidal droplet, the presence of the disperse phase alters the interfacial properties, which, in turn, affects the evaporation kinetics of the droplet non-trivially (Wi et al. 2011).

The presence of paramagnetic particles creates ferromagnetic advection within the droplet under the influence of a static magnetic field. It is worth adding here that this ferromagnetic advection enhances the evaporation kinetics of the droplet (Jaiswal et al. 2018). Jadav et al. (2017) explored the role of a static magnetic field on the evaporation characteristics of a sessile ferrofluid droplet. In the absence of an external magnetic field, the

ferrofluid droplet exhibits coffee ring formation. However, beyond a critical magnetic field strength, the ferromagnetic advection becomes essential for the complete suppression of the coffee ring pattern.

1.6 RESEARCH GAPS

A thorough scrutiny of the existing literature unveiled that although a significant amount of available literature reported enhancement in convective heat transfer characteristics when a time-dependent magnetic field perturbs the ferrofluid flow domain, the mechanism of enhanced heat transfer is not extensively investigated. As such, an overall experimental understanding about the role played by the frequency of the time-dependent magnetic field on the augmentation process is still lacking. In addition, the role of the various time scales on the flow momentum and energy transport remains to be comprehensively explored. Moreover, the experimental investigations reported in the literature are not extensive, primarily due to the limitations of the measurement techniques used in the referred study. In the presence of a magnetic field, the ferrofluid flow and thermal characteristics no longer show symmetric behavior, even if the geometric symmetry exists in the flow domain. For example, temperature and velocity remain fixed at all the points in peripheral direction for given axial and radial co-ordinate during convective flow in a circular tube, but the application of an external field may disrupt this symmetry. During non-symmetric thermal and flow conditions, using point measurement probes like thermocouple or any such sensor may lead to error in the pertinent calculations and restricts the outcome of the experimental studies.

A careful review of the available literature survey reveals that no work is reported in which the internal dynamics of the ferrofluid droplet are explored in the presence of a time-dependent magnetic field. The internal hydrodynamics of the ferrofluid droplet is likely to exhibit fascinating features due to the complicated local dynamics owing to the non-uniform distribution of the magnetic nanoparticles inside the droplet. The relative distribution of the magnetic nanoparticles nearby the magnetically active contact line plays a vital role in modifying the local forces. Moreover, the time-dependent motion of the magnetic nanoparticles will ensure various time scales such as advective, viscous, and perturbation time scale govern the local dynamics of the ferrofluid droplet. Insights into the internal hydrodynamics of the ferrofluid droplet could shed light on intricate details, which might be useful in understanding its subsequent evaporation and spreading dynamics in the presence of an external magnetic field.

In addition to exploring the internal hydrodynamics of the ferrofluid droplet in the presence of a time-dependent magnetic field, issues relating to the mixing characteristics of the droplet remains to be fully explored. A few literatures have shown that a rotating magnetic field ensures a significant augmentation of mixing in the droplet domain. However, the application of a rotating magnetic field in practice complicates the design as well as the fabrication process of the open surface droplet-based micromixer. This aspect, to be precise, limits the use of the rotating magnetic field in the area of open surface micro-mixing platform. The droplet-based micro-mixing under the influence of the time-dependent magnetic actuation could be an interesting proposition, attributed to the rich physical interplay of various spatio-temporal scales involved, as well as to its immense consequences on the efficient mixing following flow instabilities. For instance, the transient motion of the magnetic nanoparticles may trivially/non-trivially manipulate the droplet flow dynamics. As such, this maneuvered flow domain may augment the mixing characteristics of the magnetic fluid with another non-magnetic droplet.

A review of the existing literature suggests that there has been some emphasis on understanding the evaporation kinetics of a ferrofluid droplet under the influence of a static magnetic field. Careful maneuvering of the motion of the magnetic nanoparticles (MNPs) in the ferrofluid droplet under the influence of a time-dependent magnetic field could offer a controlled avenue in altering its evaporation kinetics. Important to mention, the kinetics of magnetic particle convection in the presence of a time-dependent magnetic field, with its implication on the droplet evaporation, remains unexplored till date.

1.7 AIM OF THE PRESENT WORK AND PROBLEM DEFINITIONS

From the above discussions, it may be inferred that several aspects of ferrofluid dynamics are yet to be investigated in the purview of magnetofluidic based transport. Accordingly, the scope of the present dissertation is outlined as follows.

1.7.1 Effect of magnetic field on the convective heat transfer characteristics of ferrofluid flow in a heated channel

- The first problem investigated here aims to explore the convective heat transfer characteristics of ferrofluid flow in a heated stainless steel tube under the influence of a magnetic forcing environment. Flow and thermal fields have been perturbed by a steady and time-varying magnetic field. For measuring the wall temperature, InfraRed Thermography (IRT), a field measurement technique, has been employed. For the

detailed thermal footprints of ferrofluid in the magnetically active zone, microthermal visualizations have also been performed. In addition, bright field visualization is carried out for a qualitative understanding of the internal hydrodynamics of the ferrofluid flow in the presence of a magnetic field.

1.7.2 Effect of time-dependent magnetic on the internal hydrodynamics of a sessile ferrofluid droplet

- The second problem investigates the internal hydrodynamics of a sessile ferrofluid droplet in the presence of a time-dependent magnetic field. It is revealed that the transient motion of the magnetic nanoparticles is likely to exhibit some fascinating features because of the presence of complicated local dynamics owing to the dynamical change of the driving force. Bright field visualizations and μ-PIV measurements were carried out in order to understand the internal hydrodynamics of the ferrofluid droplet.

1.7.3 Effect of time-varying magnetic field on the mixing characteristics of a sessile ferrofluid droplet with a non-magnetic droplet

- The third problem addressed here extends the second problem in an effort to investigate the non-trivial effect of the magnetic field on the mixing dynamics of the ferrofluid droplet with a non-magnetic droplet. A new method of generating strong convection inside the ferrofluid droplet under the modulation of a time-periodic magnetic field is explored. The ferrofluid droplet (base) is placed in between two alternatively acting electromagnets. The results revealed that the transiences in nanoparticles induce a magneto-convective flow, which, in turn, promotes the mixing of the base droplet with the non-magnetic sister droplet being injected from the top. Bright field visualization, micro-particle image velocimetry, and micro-laser induced fluorescence are used for qualitative and quantitative understanding of the mixing characteristics of the ferrofluid droplet. In addition, numerical simulation was also carried out to gain insight into the intricate physics of the concentration flow field.

1.7.4 Effect of time-dependent magnetic field on the evaporation dynamics of a sessile ferrofluid droplet

- The fourth problem addressed here extends the third problem in a sense that the effects of magneto-convective induced non-trivialities on the evaporative characteristics of the droplet are studied in a pinpointed manner. The evolution of the ferrofluid droplet

in a controlled atmosphere, when perturbed by a time-dependent magnetic field with various frequencies, is investigated. To explore the motion of the magnetic nanoparticle motion, bright field visualization is carried out. Whereas micro-particle image velocimetry (μ-PIV) is employed to explore the motion of the bulk liquid of the ferrofluid droplet. The droplet morphological evolution is captured with a CMOS camera.

1.8 OUTLINE OF THE THESIS

The remaining part of the present thesis is organized as follows:

- In **Chapter 2**, the experimental methodology adopted in the present work is aptly discussed. Also, the synthesis and characterization of the ferrofluid solution are elaborated in Chapter 2.

- In **Chapter 3**, the convective heat transfer characteristics of ferrofluid flow in a heated stainless steel tube as modulated by a steady and time-varying magnetic field is discussed.

- In **Chapter 4**, the role of the magnetic field on the internal convections of the ferrofluid droplet is elaborately discussed.

- In **Chapter 5**, the fundamental issues concerning the mixing dynamics of a ferrofluid droplet with a non-magnetic droplet are discussed in detail.

- In **Chapter 6**, the evaporation characteristics of a sessile ferrofluid droplet as modulated by a time-varying magnetic field are presented.

- Finally, in **Chapter 7**, based on the inferences drawn in the preceding chapters, some important conclusions are presented, and the scope of further works in the context of the theme of the present thesis are also highlighted.

Chapter 2

EXPERIMENTAL METHODOLOGY

Various experimental measurement techniques such as goniometry, infrared thermography, micro-particle image velocimetry, micro-laser induced fluorescence, bright field visualizations, etc., were employed in this research investigation. In this chapter, detailed discussions of the various experimental approaches are discussed. In addition to that, the image processing involved in the quantification of the droplet morphology is also elaborated. Also, the fabrication of the electromagnet and the preparation of the PDMS substrate is discussed. Lastly, the synthesis of ferrofluid and its characterization were discussed in detail.

2.1 INTRODUCTION

Several problems addressed in the present dissertation explores the transport phenomena of ferrofluid in small-scale systems following experimental investigations and supported by theoretical analysis in pertinent cases. The involved experimental methods primarily deal with the measurement of temperature, velocity, and mass transfer. The thermal characteristics of the flow field are measured with the help of an infrared camera. Micro particle image velocimetry (μ-PIV) and micro laser induced fluorescence (μ-LIF) are employed for the quantification of velocity and mass transfer, respectively. The temporal evolution of the contact angle of the droplet is measured with the help of a goniometer. While the change in the droplet diameter, height is observed with the help of a CMOS camera. The recorded images are further processed using an in-house developed code to extract the required information. In this chapter, we discuss all the experimental methodologies involved in greater detail.

2.2 MEASUREMENT OF DROPLET MORPHOLOGY

Exploring the evolution of the droplet morpholgy is of great importance from the perspective of droplet evaporation, particularly in understanding the role of various forces acting at its contact line on the overall evaporation process. The morphological evolution of the ferrofluid droplet is quantified by the changes in the contact angle, diameter, and height of the droplet. The Goniometer (Make: ACAM-NSC), schematic of which is shown in Fig.

2.1(a), is used to measure the contact angle of the droplet. Note that the set-up consists of a droplet-dispensing module, a white LED light, a diffuser, and a CMOS camera. A sessile droplet of the required volume is dispensed into the treated substrate with the help of the droplet-dispensing module (speed range: 0.038-16µl/s). The white LED light, together with the diffuser, is used to illuminate the droplet volume. The images are captured with the CMOS camera, having a resolution of 744 x 480 pixels[2]. These captured images are post-processed further to extract information from it, such as the change in contact angle (θ), diameter (D), height (H) of the droplet.

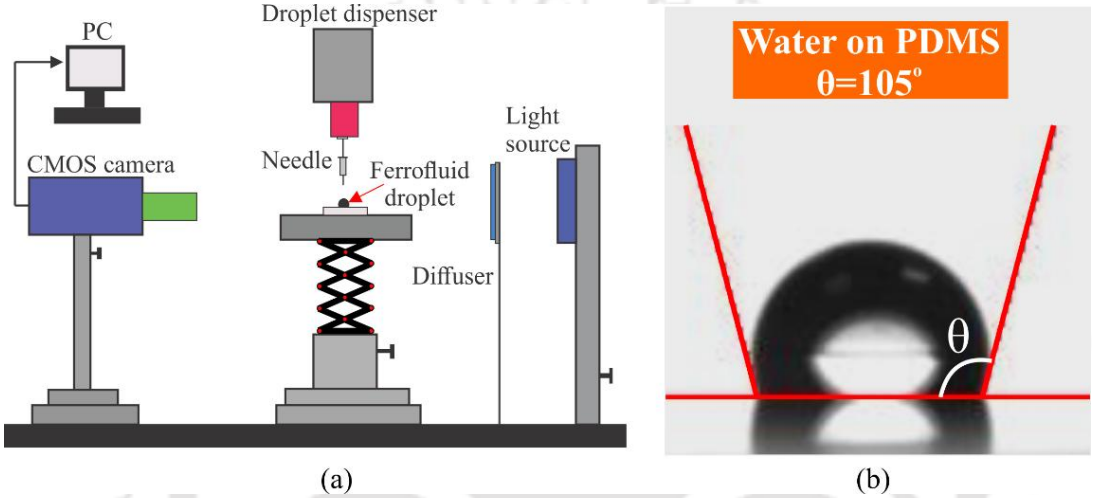

Fig. 2.1 (a) Schematic representation of the contact angle measuring system. (b) Plot shows the contact angle of water on a PDMS coated substrate. The contact angle of water on a PDMS substrate is around 105°

2.2.1 Determination of contact angle

The captured side view images are processed in ACAM-NSC software to obtain the required contact angle. The contact angle (θ) is measured by contour recognition based on the greyscale analysis of the images. The baseline is determined, and the droplet shape was fitted. The droplet shape of our sample is determined by the tangential (polynomial approximation) method. In this method, the contact angle was found by fitting a tangent to the shape of the contact line. The mean between the two measured values of contact angle (left and right) is taken as the required contact angle exhibited by the droplet. The accuracy of the contact angle measurements was around ±0.3°. Figure 2.1(b) shows the contact angle of a sessile water droplet on a PDMS surface, measured with the help of the ACAM-NSC software.

2.2.2 Determination of diameter and height of the droplet.

As mentioned before, the images captured using the CMOS camera were further subjected to post-processing for extraction of information such as the change in diameter, height, etc., of the droplet. Initially, unsharp masking is carried out on the captured droplet images employing ImageJ software (Schneider et al. 2012). The unsharp masking algorithm ensures to have a sharpening of the droplet images. The sharpened images are further converted to 8-bit binary image. The binary image typically contains pixels intensity values as either '0' or '255'. The images are then outlined, i.e., only the edges are detected. Following this, the pixel information of the images is fed to an in-house developed code for determining the respective temporal changes in height, diameter, and contact line velocity of the droplet. In Fig. 2.2, we show a schematic of all the sequences involved in the image processing methodology.

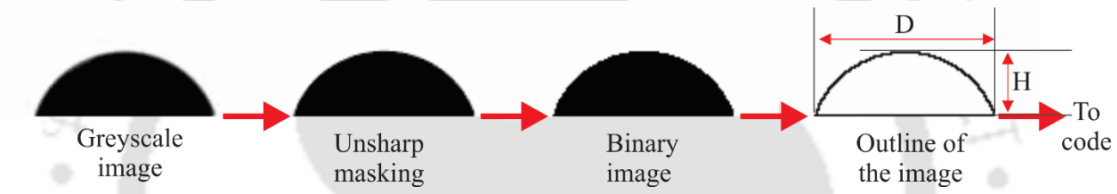

Fig. 2.2 Plot illustrates the sequence of the image processing steps involved for extracting information such as diameter, height, contact line velocity from the droplet images.

2.3 INFRARED THERMOGRAPHY

Infrared thermography (IR) exhibits several advantageous features in comparison to conventional temperature measurement approaches such as thermocouples, RTD, pyrometer, etc. Since conventional approaches provide thermal information of a point in a flow domain, the situations where the flow exhibits high spatial gradients in both axial and lateral dimensions, the conventional system may prove erroneous in capturing the accurate information. In comparison, the infrared camera can accurately map a two-dimensional thermal flow field, even in situations where high gradients in the flow parameters are involved. Therefore, in this work, an infrared thermal imaging camera (FLIR® A655sc) has been employed for quantification of the thermal field. The IR camera has a spectral range of 7.5-14 μm, 16-bit signal digitization, and maximum frames per second of 200 for the resolution of 640 × 120 pixels^2 (refer to section A.1 for details regarding the IR camera). The recorded thermograms are post-processed with the help of ResearchIR software. In the succeeding sub-section, the practical consideration and the emissivity corrections of the adopted infrared thermography is discussed in detail

2.3.1 Practical consideration

An object whose emissivity is low, thermal mapping of its temperature via infrared camera becomes highly unreliable. For an opaque low emissivity surface, reflections will be higher, and the role of the 'Narcissus effect' on the thermogram cannot be ignored (Chauvet et al. 2010). In thermography, the 'Narcissus effect' describes the black spot that is visible whenever a cooled thermal camera is directed to a flat reflective surface where it 'sees itself.' Since the interior of the camera is cooled, and the objective is transparent to the detected IR radiation, the image of the objective of an IR camera in operation detects a cool object. Thus, infrared thermography should be carried out for an object with higher emissivity.

Likewise, when the temperature of the object is similar to the ambient temperature, the noise involved in comparisons to the useful signal on the infrared thermograms may be substantial. Therefore, in practice, the object temperature should be at least 15ºC greater than the background temperature for a reliable thermal reading.

2.3.2 Emissivity corrections

As already discussed in the preceding discussions that emissivity plays a vital role in infrared thermography. There are two standard approaches available for mapping the emissivity of the object, as discussed next. In the first approach, a high emissivity material with good thermal conductivity is pasted over a small portion of the object whose emissivity is to be mapped. The object is then heated to a temperature of at least 50ºC, higher than the ambiance. After a certain amount of time, when a steady-state is reached, the temperature of the material (of known emissivity) is read from the software. In the next step, the area of investigation is moved to the object whose emissivity is to be mapped. With all other parameters remaining the same, the value of emissivity is tuned in the software in such a way that the temperature in the area of investigation matches with the temperature of the materials of know emissivity.

While in the other method, thermocouples are employed to measure the temperature of the object whose emissivity is to be measured. Once the temperature of the thermocouple is attained, the emissivity value is tuned in such a way that the object temperature matches the temperature of the thermocouple. In the present work, the latter method is used for mapping the emissivity of the object.

2.4 MICRO PARTICLE IMAGE VELOCIMETRY

Micro particle image velocimetry (μ-PIV) measurement technique is used for quantification of the velocity of the fluid flow field. A typical μ-PIV experimental set-up is shown in Fig. 2.3. It consists of three main components: (a) an inverted microscope, (b) a fluorescent light source, and (c) a camera. The microscope is used for magnification of the area of interrogation. While the fluorescent light source is used for excitation of the seeded tracer particles. The primary role of the camera is to capture the images of the tracer particles. For μ-PIV measurements, the fluid flow field is seeded with fluorescent microspheres with a dilution of approximately 1:20 (v/v). The above seeding particle concentration was chosen as it provided acceptably low noise levels when compared to the useful signal. The microfluidic platform was kept over the stage of the inverted microscope, and the droplet was illuminated by monochromatic light of a wavelength of 530 nm from below the microscope stage through a 10X objective lens (NA = 0.40). As a consequence, the excitation stage of the fluorescent particles is reached, and in turn, these particles emit light at a peak wavelength of 590 nm. An epifluorescent prism filter is used on the optical path to eliminate the background light. As such, only the emitted light from seeding particles reaches the camera of the μ-PIV system for further analysis.

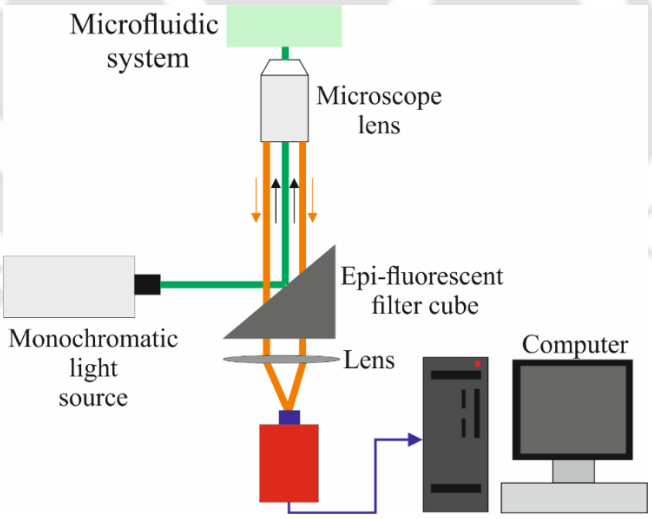

Fig. 2.3 Schematic of the μ-PIV experimental set-up. All the components are described in the text appropriately.

2.4.1 Data processing

A cross-correlation algorithm is used for the extraction of velocities from the captured images. Figure 2.4 shows the various steps involved while performing the cross-correlation algorithm. In the first step, pre-processing of the captured grayscale images of the tracer

particles is carried out. Pre-processing ensures easy detection of the seeded tracer particles in the fluid flow domain. In step-2, the capture images are divided into small interrogation windows. Each interrogation window contains at least 10-15 tracer particles, with each particle measuring around 2-3 pixels. The cross-correlation algorithm is performed in two consecutive images, as can be seen from step-3 in Fig. 2.4. The cross-correlation at an interrogation window of size $M \times N$ is given by:

$$\psi(x,y) = \sum_{n=1}^{N-1} \sum_{m=1}^{M-1} f(m,n) \cdot g(m+x, n+y) \qquad (2.1)$$

where $f(m,n)$ and $g(m,n)$ are the grey level distribution of the first and second exposures respectively, and $\psi(x,y)$ is the value of the cross-correlation function for a displacement vector of dx.

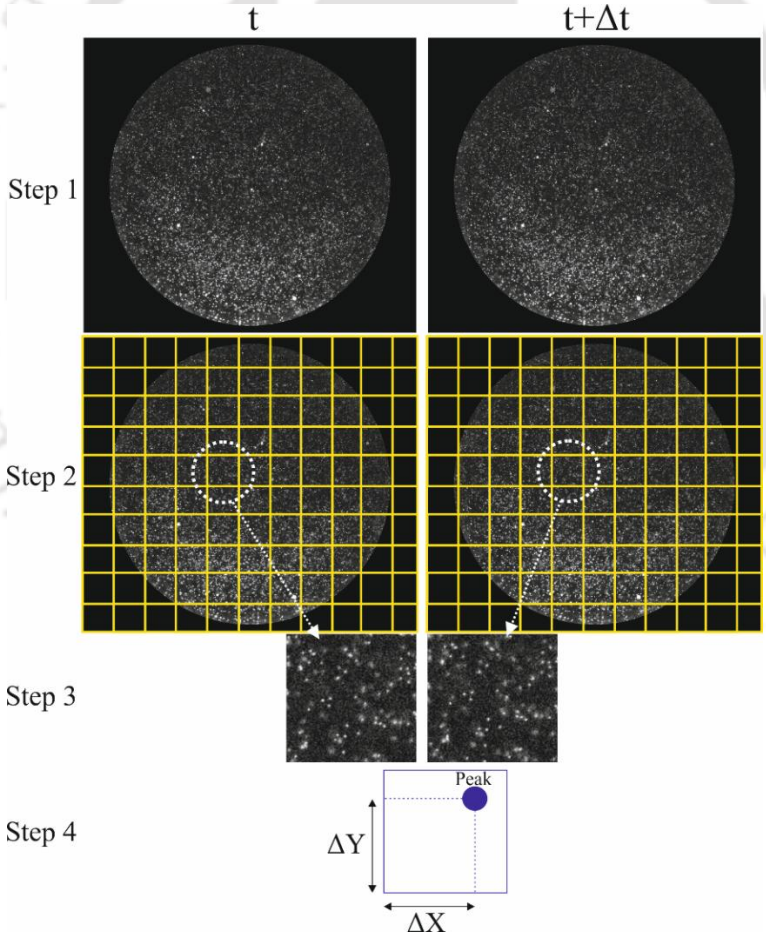

Fig. 2.4 Schematic representation of the various steps involved in the evaluation of velocity of the fluid flow domain following the micro-PIV measurement technique.

The maximum peak value of the cross-correlation function indicates the displacement of the particles, as shown in step 4 of Fig. 2.4. The velocity is obtained by dividing the

displacement with the time-interval between the two consecutive images, i.e., Δt. Each interrogation window gives a velocity vector. Eventually, a velocity field is achieved in the fluid flow domain. In the present study, double images were captured per realization in such a way that seeding particles moved approximately 1/4th size of the interrogation window used for correlation between two consecutive images. Before carrying out the cross-correlation algorithm, raw µ-PIV images were overlapped using ImageJ software (Schneider et al. 2012). Image overlapping prior to correlation was carried out to increase the number of seeding particles per interrogation window resulting in easy peak detection. A cross-correlation algorithm with interrogation size 64×64 pixels^2 and 50% overlapping between interrogation windows was used to calculate the instantaneous velocity vector field inside the droplet.

2.5 GENERATION OF MAGNETIC FIELD

Two different electromagnets were fabricated as per requirements for the problems investigated in the present thesis. For perturbing the heated ferrofluid flow domain, a 'C' shaped electromagnet is fabricated. In contrast, a cylindrical shaped electromagnet is fabricated for magnetically disturbing the ferrofluid droplet domain. In Fig. 2.5, we show the schematic representation of these two typical shaped electromagnet. The electromagnets are produced by winding 26 SWG (Standard wire gauge) enamel coated copper wires (~ 40 turns per cm) on a mild steel core. Note that the electromagnets are kept at a predefined distance from the periphery of the fluid domain. The electromagnet is activated by supplying current from a DC power source (Make: Aplab). For generating time-dependent magnetic fields, we have developed an in-house digital circuit to supply pulsed current to the electromagnet. The magnetic field is measured at the surface of the electromagnet facing the droplet by a Gaussmeter (Make: SES Instruments).

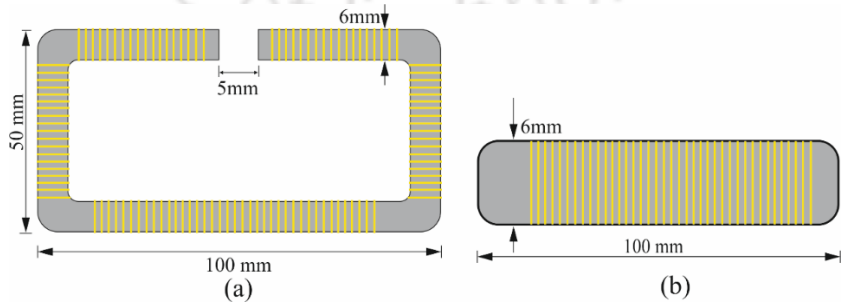

Fig. 2.5 Schematic representation of the electromagnet having (a) 'C' (b) Cylindrical, shaped structure. The 'C' shaped electromagnet is used for perturbing the ferrofluid flow domain, while the cylindrical-shaped electromagnet is used for perturbing the ferrofluid droplet domain.

2.6 PREPARATION OF SUBSTRATE

Microscopic glass slides (Make: Struers) of 1.1 mm thickness and 27×46 mm^2 in size were used as a substrate. The glass slides were coated with a thin cured PDMS layer to prepare the final hydrophobic substrate. The PDMS solution was prepared by mixing silicone elastomer (Make: SYLGARD 184) with a curing agent in the ratio of 10: 1. The solution was de-gasified in a vacuum chamber. The degassed solution was then poured onto the glass substrate and coated by a spin coater (Make: Apex instruments) at $3400\ RPM$ for the $50\ s$. It may be mentioned here that the spinning effect results in a thin as well as uniform deposition of the PDMS layer on the substrate. The prepared glass substrate was then placed on a hot air oven for around 3 hours at a constant temperature of 80 °C. The ferrofluid solution forms a contact angle of $\theta_{ferrofluid}$~65° on the PDMS substrate. The magnetic nanoparticles are coated with surfactant (Lauric acid) essentially to prevent any interparticle agglomeration in the ferrofluid solution. Note that the coated surfactant layer lowers the contact angle of the ferrofluid solution to the aforementioned value, as witnessed in Fig. 2.6 mentioned above.

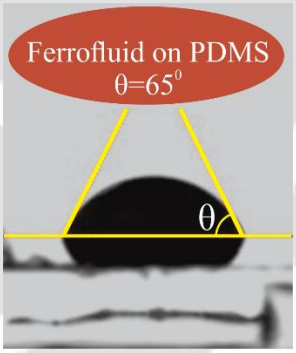

Fig. 2.6 Plot illustrates the static contact angle of a sessile ferrofluid droplet on the treated PDMS substrate.

2.7 SYNTHESIS AND CHARACTERIZATION OF FERROFLUID

Iron oxide nanoparticle (IONPs) were synthesized chemically by the co-precipitation method from an aqueous mixture of Fe^{+3}/Fe^{+2} in the molar ratio of 2:1 by using concentrated ammonium hydroxide solution in an inert atmosphere of nitrogen. After the co-precipitation of magnetic nanoparticles, lauric acid was added as a stabilizer. After 30 min of reaction, the temperature was elevated to 100-110 °C in order to remove the excess water and ammonium hydroxide. Next 1 gm of the solution, as received above, was added to 6.0 gm of n-hexane to form an organic dispersion. For the aqueous phase transfer, the prepared dispersion was added to 20 mL of aqueous solution of sodium lauryl sulphate (10–60% (w/w). The mixture was subjected to sonication twice for 2 min at 90% amplitude with a Sonificator (Make: Branson)

in an ice-cooled bath followed by the evaporation of n-hexane under continuous stirring at 80 °C for three hours. The water loss was compensated by adding 2 mL of water every 30 min to obtain a stable water-based ferrofluid solution.

The magnetization curve of the water-based ferrofluid for the volume fraction (φ) of 4.34%, and 0.5% is shown in Fig. 2.7(a)-(b). Both the plots illustrate the super-paramagnetic characteristic of the ferrofluid solution. The nanoparticles have an average size of around 50 ± 2 nm, as shown in Fig 2.7(c) as measured by the dynamic light scattering (DLS) technique. The absolute zeta potential of the ferrofluid was found to be 53 mV (Fig. 2.7(d)), and for an absolute value of zeta potential higher than 25–30 mV, it is generally accepted that the particles are electrostatically stable (Xu 2002).

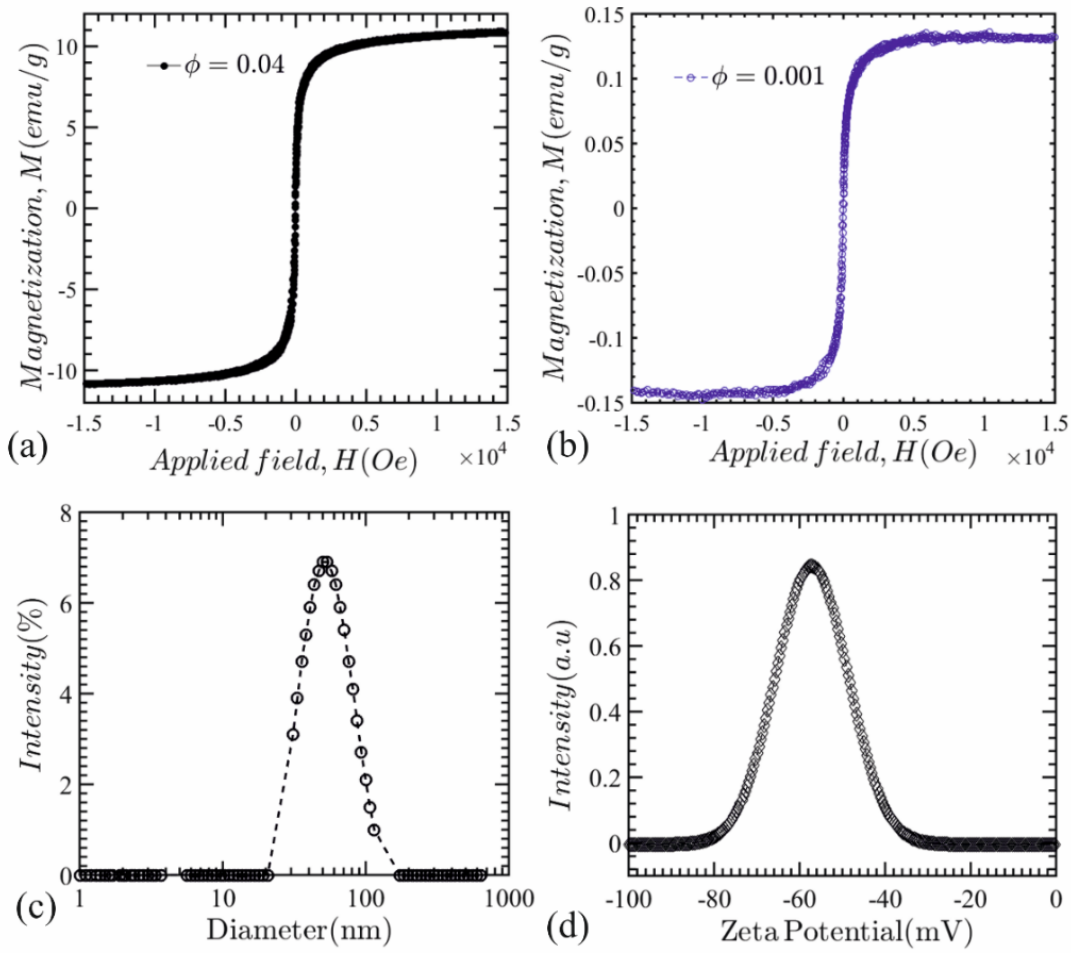

Fig. 2.7 Plot showing the hysteresis loop of the prepared ferrofluid sample as measured by the Vibrating sample magnetometer (VSM) for the magnetic particle volume fraction of (a) 4.3%, (b) 0.1%. The ferrofluid exhibits no hysteresis and is superparamagnetic in nature; The plot depicts the (c) particle size distribution, and (d) zeta potential of ferrofluid solution

2.8 SUMMARY

In this chapter, elaborate discussions are made pertaining to the experimental techniques deployed to address the problems considered in the present thesis. In addition to that, the fabrication of the electromagnet and substrate preparation is aptly discussed. At the end of this chapter, the synthesis and characterization of the ferrofluid solution are described in detail. The magnetic nanoparticles in the ferrofluid are found to be superparamagnetic in nature. In the forthcoming chapters, results pertaining to the problems considered in the purview of this dissertation will be discussed in detail.

Chapter 3

EFFECT OF MAGNETIC FIELD ON THE CONVECTIVE HEAT TRANSFER CHARACTERISTICS OF FERROFLUID FLOW IN A HEATED CHANNEL

This chapter explores the energy transport characteristics of ferrofluid flow in the presence of a steady and time-dependent magnetic field. The thermohydrodynamics of ferrofluid flow in a heated stainless steel tube on perturbation by an external electromagnet is thoroughly investigated. For quantification of the thermal characteristics of the flow field, infrared thermography is employed, while bright field visualization technique is used for a qualitative understanding of the behavior of the magnetic nanoparticles. Possible distinctive features of the motion of the magnetic nanoparticles in the presence of a steady and time-dependent magnetic field and its ultimate consequence on the enhancement of energy transport are highlighted.

3.1 INTRODUCTION

Perturbing the ferrofluid flow domain by a steady and time-varying magnetic field can be an effective proposition in augmenting its convective heat transfer characteristics (Ganguly et al. 2004; Goharkhah et al. 2015a, 2016; Asfer et al. 2016). This chapter reports the convective heat transfer characteristics of ferrofluid flow inside a circular stainless steel tube under uniform heated wall conditions. The flow Reynolds number (Re) is kept fixed to the value of 66. Flow and thermal fields have been perturbed by a steady and time-varying magnetic field. In constant magnetic field cases, experiments have been carried out for magnetic flux density ($\bar{B}$) values of 0 G, 700 G, and 1080 G. The heat transfer coefficient obtained for $\bar{B} = 1080$ G has been found to be higher among those. Hence, in the time-varying magnetic field case, magnetic field flux density has been kept constant to 1080 G, and the frequency of the time-dependent magnetic field (f) has been varied from 0.1 Hz to 5.0 Hz. For measuring the wall temperature, InfraRed Thermography (IRT), which is a field measurement technique, has been employed. To get the detailed thermal footprints of ferrofluid in the magnetically active zone, microthermal visualizations and quantifications

have also been performed. Numerical simulations were conducted to gain detailed insights into the intricate physics involved.

3.2 MATERIALS AND METHODS

3.2.1 Experimental setup

To study the thermohydrodynamics of ferrofluid flow under the effect of a constant and time-dependent magnetic field, an experimental set up is fabricated, schematic of which is shown in Fig. 3.1. The test section consists of stainless steel (SS) tube of an inner diameter of 1.6 mm and an outer diameter of 2.0 mm, which stands on a PMMA platform. An initial unheated length of 150 mm is kept in order to ensure that the flow reaches its hydrodynamically, fully developed conditions. The heated length has been kept at 280 mm so that thermally developed flow can be established in some parts of the heated domain of the tube. Uniform wall heat flux condition is maintained by using Joule heating with a DC power supply of power rating of 0-32 V and 0-30 A (Make: Aplab). Digital Multimeter (accuracy ±0.1 V and ±0.01 A) has been incorporated with the DC source to measure the electrical power input to the SS tube. The magnetic field is provided with the help of C shaped electromagnet. Details of the electromagnet design and fabrication are appropriately discussed in section 2.5 of chapter 2. The electromagnet stands on an internally threaded acrylic platform, such that the height can be adjusted with the help of a screw-based arrangement. The current flowing in the electromagnet is controlled by an in-house designed electronic circuit such that a constant current flows through it when a constant magnetic field has to be applied while the flow of current can be modulated by the desired frequency to apply a time-dependent magnetic field to the flow domain.

An infrared thermal imaging camera (FLIR® A655sc) has been employed to measure the temperature field of the outer wall of heated SS Tube. Details of the infrared thermography technique adopted are elaborately discussed in section 2.3 of chapter 2. A very thin black coating (thermal conductivity, k ~ 0.15 W/m-k) of high emissivity (ε ~ 0.98) is used at the outer surface of the SS tube for reliable IR measurements. The emissivity correction of the coated surface has been done before the actual experiments by independently measuring the surface temperature. All the experiments were carried out in a dark room to minimize the surrounding radiation. IR camera was focused on measuring the heated length of 100 mm (i.e., 640 pixels for 100 mm) out of a total 280 mm heated length. It was ascertained beforehand that the zone recorded from the IR camera lies in a thermally developed zone. The

spatial resolution was found to be 0.015 mm per pixel in the axial direction and 0.2 mm per pixel in the transverse direction. In the case of a constant magnetic field, wall temperatures were recorded after reaching the steady-state. In time-varying magnetic field cases, thermograms were recorded after the establishment of the periodic nature of temperature. In the time-dependent magnetic field case, the acquisition rate has been varied according to the modulation frequency of the magnetic field. The acquisition rate was chosen such that at least 20 images have been captured for one time-period of magnetic field modulation.

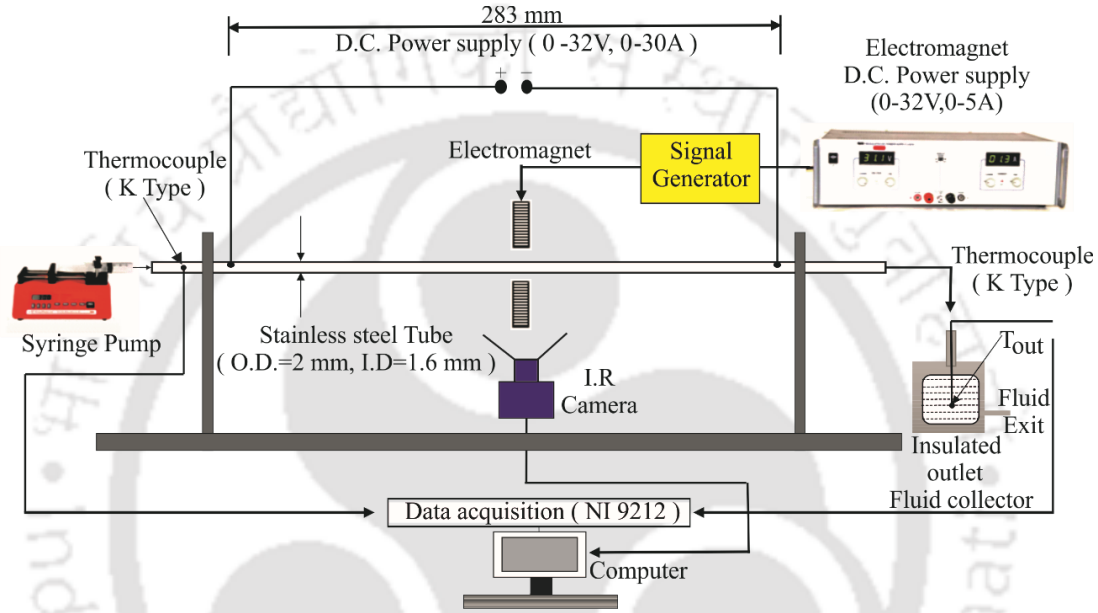

Fig. 3.1 Schematic of the fabricated experimental set-up. All the components are aptly discussed in the text.

Table 3.1 Thermophysical properties of the ferrofluid and DI-water

	Density ($Kg\ .m^{-3}$)	Specific heat ($J\ .(Kg.K)^{-1}$	Thermal conductivity $W.(m.K)^{-1}$	Viscosity Pa-s
DI- water	995	4180	0.6	0.009
Ferrofluid	1137.6	3425	0.7	0.00106

Two K-type thermocouples (bead diameter=0.1 mm) are used for measuring the inlet and outlet temperature. An insulated chamber is fabricated to record the outlet temperature. At the outlet, the thermocouple bead is inserted into the chamber such that the bead remains immersed in the flow. The temperature readings are recorded with the help of data acquisition cards (Temperature module NI 9212) and software platform NI® LabVIEW 2017. The acquisition rate has been chosen as 2 Hz, 20 Hz, and 200 Hz for the magnetic field frequency of 0.1 Hz, 1 Hz, and 5 HZ, respectively. The water-based ferrofluid used in the experiments consists of iron nanoparticles with a volume fraction of 4.64 % (v/v). The synthesis and

characterization of the water-based ferrofluid are discussed in section 2.6 of chapter 2. The thermophysical properties of ferrofluid are listed in table 3.1.

3.2.2 Data reduction

The spatio-temporal data obtained with the help of the IR camera and thermocouple are used to calculate the steady, time-averaged Nusselt number and non-dimensional wall temperature. The local Nusselt number along the stream length is calculated as:

$$\left.\begin{aligned} Q_{in} &= V \cdot I - Q_l \\ Nu &= \left(\frac{q'' \cdot D_h}{(T_w - T_m) \cdot k_{ff}}\right) \end{aligned}\right\} \tag{3.1}$$

Where $q'' = Q_{in}/(\pi \cdot D_h \cdot l)$, is the heat flux along the flow direction. V is the potential drop across the heated length, and I is the current supplied, and l is the length of the heated zone. Q_l is the heat lost to the ambient by the heated SS tube. The heat lost to the ambient atmosphere is independently calculated by running dry tube heat transfer experiments. When the SS tube is given some heat in dry condition, i.e., no fluid is flowing inside the tube, at steady state, the given heat will be equal to the heat lost to the ambiance, and the outer surface temperature of the SS tube is recorded. Repeating this experiment for various heat input, a calibration curve has been obtained for heat loss and surface temperature. With the help of this calibration, heat input in the actual experiments were found.

The non-dimensional wall temperature is given by:

$$T^* = \left(\frac{(T - T_{ffi})}{q'' \cdot D_h/k_{ff}}\right) \tag{3.2}$$

Where T_{ffi} is the ferrofluid inlet temperature. It must be noted that local measurement of the bulk mean mixing temperature of the fluid, T_m is complicated. Therefore, the best possible option is to apply the energy balance to calculate the outlet bulk mean mixing temperature by knowing the inlet bulk mean temperature. In the present study, it has also been noted that measuring the fluid temperature at the outlet by the thermocouple does not represent the actual bulk mean temperature at that location.

3.2.3 Numerical method

Figure 3.2(a) presents the schematic diagram of the computational domain in which the simulations are performed. Single-phase ferrofluid is assumed to flow through a two-

dimensional channel. The third dimension of the channel is assumed to be much larger than its other two dimensions. Uniform heat flux is applied to the wall, and two-line dipoles are placed adjacent to the top and bottom wall, which provides the external magnetic field. The position of the dipoles is chosen specifically to replicate numerically, the magnetic field that is used in the experiment, where, because of the C shaped structure of the magnet, one pole is above the SS tube, and another pole is below the SS tube and thus justifying the chosen position of the line dipoles. Since the third dimension is ignored, the resulting field is reduced to a two-dimensional flow field, which can be expressed in polar coordinate as below (Ganguly et al. 2004):

$$\bar{H}(r,\theta) = m\left(\frac{\sin\theta}{r^2}\hat{e}_r - \frac{\cos\theta}{r^2}\hat{e}_\theta\right) \tag{3.3}$$

where $\bar{H}$ is the vector of the magnetic field strength, m denotes the magnetic dipole moment, which determines the strength of the dipole, and r and θ are respectively the radials and peripheral directions of polar coordinate in which $\hat{e}_r$ and $\hat{e}_\theta$ are unit vectors. The ferrofluid is assumed to be electrically non-conducting such that it does not induce any electromagnetic current on the flow. The stray electric field effects are neglected, and it is assumed that the variation in the magnetic field due to temperature gradients within the ferrofluid is negligible. The assumed magnetic field complies with Maxwell's equation in the static form:

$$\nabla \times \bar{H} = 0 \tag{3.4}$$

$$\nabla \cdot \bar{B} = 0 \tag{3.5}$$

The magnetic flux density and magnetic field are given by,

$$\bar{B} = \mu_0(\bar{H} + \bar{M}) + \bar{B}_r \tag{3.6}$$

Here the magnetization vector and the magnetic field vector are related by,

$$\bar{M} = \chi\bar{H} \tag{3.7}$$

The magnetic susceptibility is a function of temperature and is given by,

$$\chi_m = \chi_0(T) = \frac{\chi_0}{1 + \beta(T - T_0)} \tag{3.8}$$

and thus Eq. (3.5) can be written as,

$$\nabla \cdot (\mu_0(1 + \chi_m)\bar{H} + \bar{B}_r) = 0 \tag{3.9}$$

The Kelvin body force, which the ferrofluid experiences in a spatially non-uniform magnetic field, is given by,

$$\bar{F}_m = (\bar{M} \cdot \nabla)\bar{B} \tag{3.10}$$

On proper substitution, Eq. (3.10) can be written as,

$$\bar{F}_m = \frac{1}{2}\mu_0\chi_m(1+\chi_m)\nabla(\bar{H}\cdot\bar{H}) + \mu_0\chi_m\bar{H}(\bar{H}\cdot\nabla\chi_m) \tag{3.11}$$

The flow domain is incompressible, Newtonian, and has constant thermophysical properties; thus the resulting continuity, momentum, and energy equations can be written as,

$$\frac{\partial\rho}{\partial t} + \nabla.(\rho\bar{u}) = 0 \tag{3.12}$$

$$\frac{\partial(\rho\bar{u})}{\partial t} + (\bar{u}.\nabla)\bar{u} = -\nabla P + \nabla\{\eta(\nabla\bar{u} + \nabla\bar{u}^T)\} + \bar{F}_m \tag{3.13}$$

$$\rho c_p\left(\frac{\partial T}{\partial t} + \bar{u}\cdot\nabla T\right) = k\nabla^2 T \tag{3.14}$$

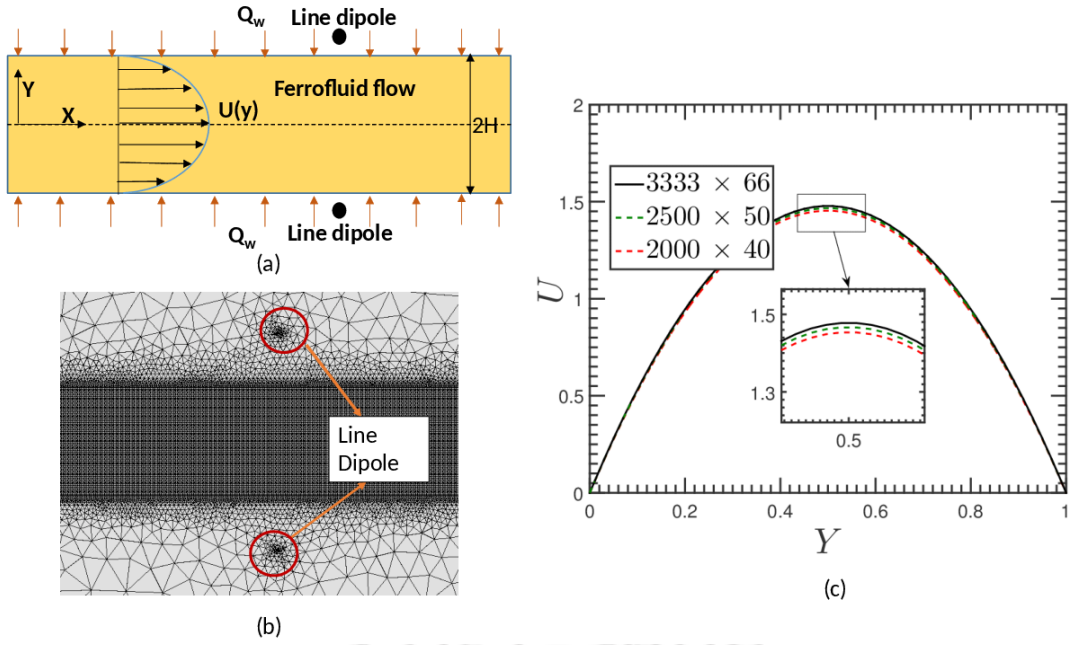

Fig. 3.2 (a) Schematic of the computational domain;(b) A typical mesh of the computational domain;(c) Grid independency test.

The governing equations are solved in commercially available Finite element software, COMSOL® Multiphysics. A fine structured and unstructured, non-uniform grid has been used in the computational domain, as can be seen from Fig. 3.2(b). A structured mapped grid is used on the fluid flow domain such that it is finer near the walls of the fluid domain, so as to capture the gradient in temperature and velocity accurately. For the rest of the computational domain, an unstructured triangular grid is used. Figure 3.2(c) shows the grid independence test. It can be seen that on increasing the grid size from 2500×50 to $3333 \times$

66, negligible changes are observed. Hence, 2500×50 is chosen as the requisite grid size. Generalized alpha is used as the time-stepping method, with the amplification of a high frequency of 0.75. A direct nonlinear MUMPS solver is used for simulating the present work. Absolute tolerance of 10^{-6} was used in the present problem. For the transient case, the time resolution was such that a one-time period was divided into 80 subsequent time steps, such that the intricate flow physics is accurately captured. The time-averaged Nusselt number is calculated, taking the average of 40 distinct complete cycles.

3.3 RESULTS AND DISCUSSION

3.3.1 Validation of the experimental result

Infrared thermography is used to study the thermohydrodynamics of ferrofluid flow in the stainless steel tube. Now to gain confidence in our experimental data, the obtained results are validated with correlations of Churchill and Ozoe (Churchill and Ozoe 1973) for hydrodynamically developed and thermally developing flow under uniform wall heat flux condition. The correlation is given by:

$$\frac{Nu_{x,h}+1}{5.364} = \left[1+\left(\frac{220}{\pi}X^*\right)^{-10/9}\right]^{3/10} \tag{3.15}$$

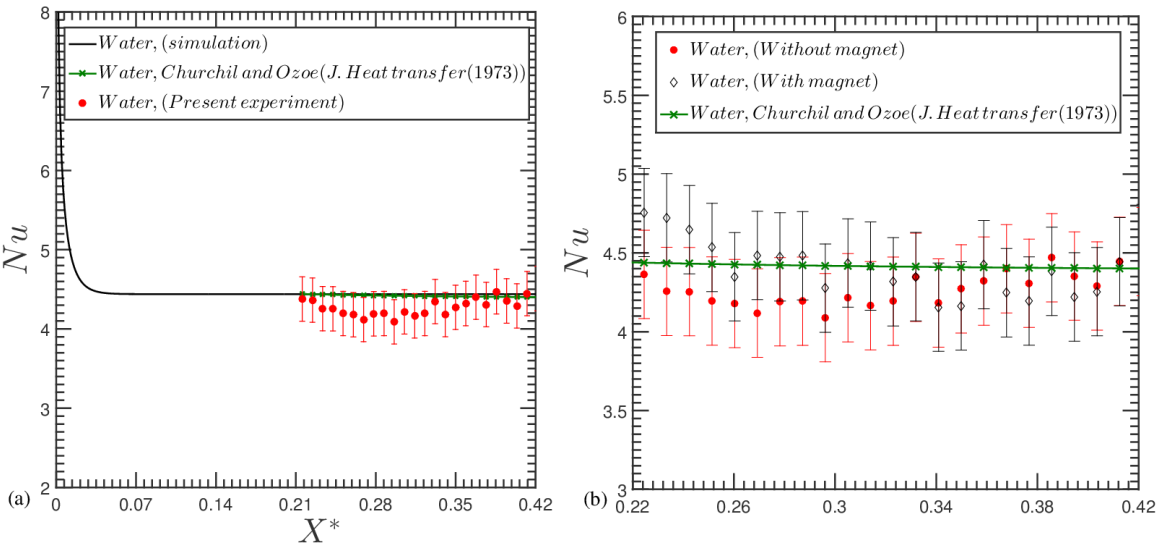

Fig. 3.3 (a) Axial variation of the local Nusselt number (Nu) calculated both numerically and experimentally. Plot also shows the local Nu variation as calculated using Eq. 3.15 proposed by Churchill and Ozoe (Churchill and Ozoe 1973); (b) Variation of local Nusselt number variation for water with and without magnet.

Figure 3.3(a) shows the axial variation of the Nusselt number of the convective flow of DI-water for the present experiment, correlation of Churchill and Ozoe (Churchill and Ozoe 1973), and numerical simulation conducted in COMSOL® Multiphysics. A good agreement

of the experimental results with the uncertainty $\pm 7\%$ has been found with the correlation and numerical simulation, as can be seen from Fig. 3.3(a). These experimental data are evidence of the successful implementation of the measurement and data analysis techniques utilized in the present study, especially the IR Thermography (IRT). This further instills confidence to estimate the heat transfer characteristics of the ferrofluid flow under the influence of a constant and time-dependent magnetic field. The experiments were repeated with DI- water for both with and without a magnetic field to confirm that there is no interference of the applied magnetic field on the IRT readings. As can be observed from Fig. 3.3(b), a similar Nusselt number can be seen for both cases.

3.3.2 Distribution of magnetic field lines

In order to have a better understanding of the dynamics of ferrofluid flow in the heated channel under the external magnetic field, the spatial distribution of the magnetic force, and the Kelvin body force, 2D numerical simulations have been carried out in COMSOL® Multiphysics. Though the numerical simulations are not the direct representatives of the present experimental conditions, still, it can be helpful in the qualitative mapping of the magnetic field. As already shown in Fig. 3.2(a)-(b), two-line dipoles are placed adjacent to the top and bottom wall of the flow domain. Figure 3.4(a)-(b) shows the variation of the magnetic flux density and the body force along the centerline of the channel. Figure 3.4(a) shows the variation of the magnetic flux density, $\bar{B}$, B_x, B_y. It can be seen that the X-component is minimal while the Y-component (B_y) dominates the flow field. Also, the resultant magnetic field, the $\bar{B}$ field is maximum at the location of the dipole, i.e., along the line of action of the magnetic dipole. As magnetism supports the superimposition theory, at the line of action of the dipole, the effect of the magnetic field is added up because of the presence of the line dipole adjacent to the top and bottom wall. Therefore, the maximum magnetic force is realized along the line of action of the magnetic field.

Figure 3.4(b) shows the variation of the Kelvin body force along the centerline of the channel. Here, it can be seen that the flow physics is primarily governed by F_X. It can also be noticed that in some regions, the direction of Kelvin body force is aligned with the flow inertia, while in some regions, both the forces oppose each other. For the flow taking place in $+X$-direction, it is clear that in the upstream of the magnetic line dipole, F_X supports the flow, while in downstream of the magnetic line dipole, F_X opposes the flow. Therefore, the inference can be drawn that the net effect of the magnetic field is to retain the flowing fluid

within the magnetically active zone of the line dipole. The effect of this behavior of the body force will be discussed in detail in the subsequent section.

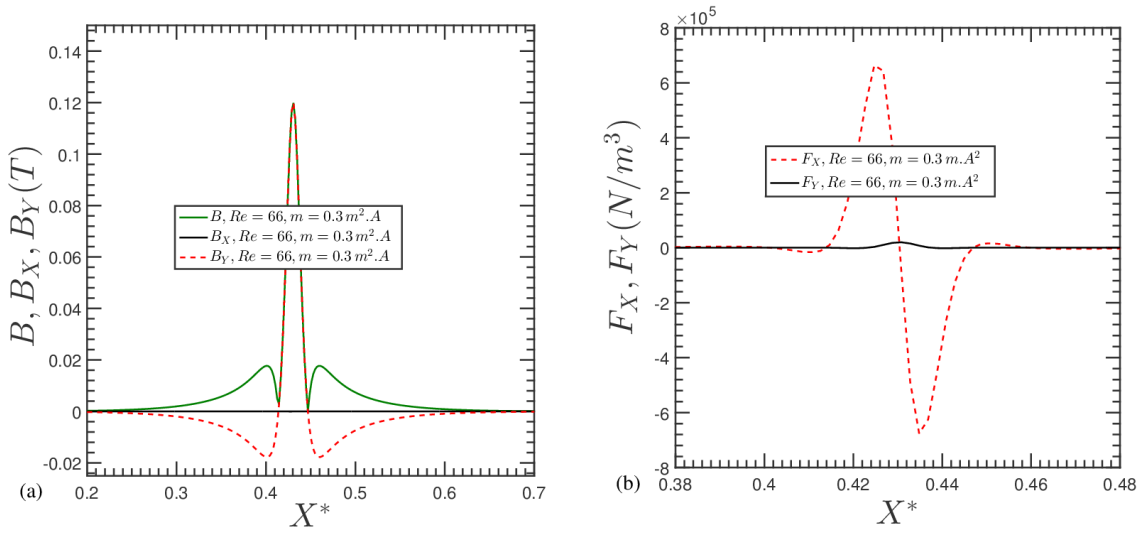

Fig. 3.4 Distribution of (a) magnetic flux density (B) and (b) magnetic force components (F_X and F_Y) along the centerline of the channel.

3.3.3 Convective heat transfer characteristics in presence of constant magnetic field

After gaining confidence in the experiments conducted for convective heat transfer using DI-water as working fluid and getting insight information regarding the magnetic field intensity and Kelvin body forces, experiments were conducted to investigate the convective heat transfer characteristics of ferrofluid under the influence of a constant magnetic field. As already mentioned, the flow Reynolds number was kept constant to the value of Re = 66. Different magnetic flux density values of 0 G, 700 G, and 1080 G were used in the experiments.

A. Effect of ferrofluid flow in the absence of a magnetic field

Axial variation of the Nusselt number for ferrofluid and water in the absence of a magnetic field is shown in Fig. 3.5. This exercise is executed to detect the effect of the thermophysical properties of ferrofluid on the heat transfer. The experimental results obtained for the ferrofluids were compared with experimental results of water (as shown in Fig. 3.3), simulations, and correlation as given in Eq. (3.15). A reasonably good agreement can be seen between the theoretical predictions (Eq. 3.15) and experimental results for the convective flow of ferrofluid in the heated SS tube in the absence of a magnetic field.

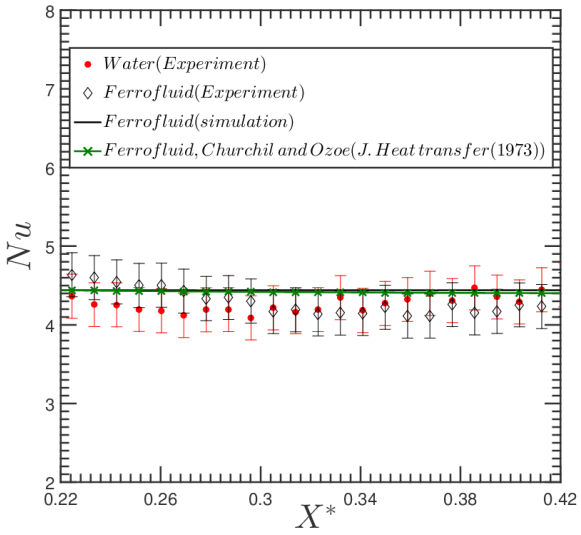

Fig. 3.5 Comparison of Nusselt number for water and ferrofluid along the non-dimensional length for Re = 66 in the absence of a magnetic field.

Similar results were reported by Rea et al. (2009). Therefore, it can be re-confirmed from Fig. 3.5 that nanofluid (base fluid + magnetic/non-magnetic nanoparticles) with enhanced thermo-physical properties hardly alters the single-phase convective heat transfer characteristics. Subsequently, it will be shown that under the effect of external body forces, indeed, the heat transfer characteristics get modified.

B. Effect of magnetic field intensity

Figure 3.6(a) shows the thermograms of stream-wise variation of the tube wall temperature for constant magnetic field intensities of 0 G, 700 G, and 1080 G. The IRT measurements clearly show that the flow and thermal field gets disturbed by the application of external magnetic field and disturbances are directly related to the intensity of the magnetic field which is visible in the thermograms in Fig. 3.6(a). Quantitatively, the effect of the magnetic field on the convective flow of ferrofluid in terms of axial variation of *Nu* and non-dimensional wall temperature T^* has been shown in Fig. 3.6(b)-(c).

It is interesting to note from Fig. 3.6(b)-(c), the disturbance created in the flow field by the external magnetic field has also been reflected in the thermal footprints of the wall. In Fig. 3.6(c), axial variation of non-dimensional temperature has been demonstrated wherein it is found that for $\bar{B}$ = 1080 G, the wall temperature is lowest among the discussed cases while it is highest for $\bar{B}$ = 0 G. The similar variation has also been obtained in *Nu* for various magnetic field intensities, as shown in Fig. 3.6(b). In the case of $\bar{B} = 0$ G, there are no external disturbances which can alter the thermal and hydrodynamic boundary layer. Hence, both the

boundary layers get established similar to the classical convective flow under uniform wall heat flux conditions. On the contrary, applying an external magnetic field of a given intensity introduces the Kelvin body force, which interacts with the flow inertia resulting in the modification of thermal and hydrodynamic boundary layers. The MNP's will be attracted towards the magnetic poles and may get attached to the wall surface, forming a hump-like structure that acts as a bluff body. The existence of hump in the flow field leads to the generation of secondary flows as well as the recirculation bubble in the downstream resulting in enhanced transport of momentum and heat. In one of the earlier studies, it has been shown that magnetic nanoparticles, under the influence of magnetic force, form a chain-like cluster dispersed in the bulk fluid as well as on the hump (Asfer et al. 2016). These chain-like structures play an important role in thermal and momentum transport.

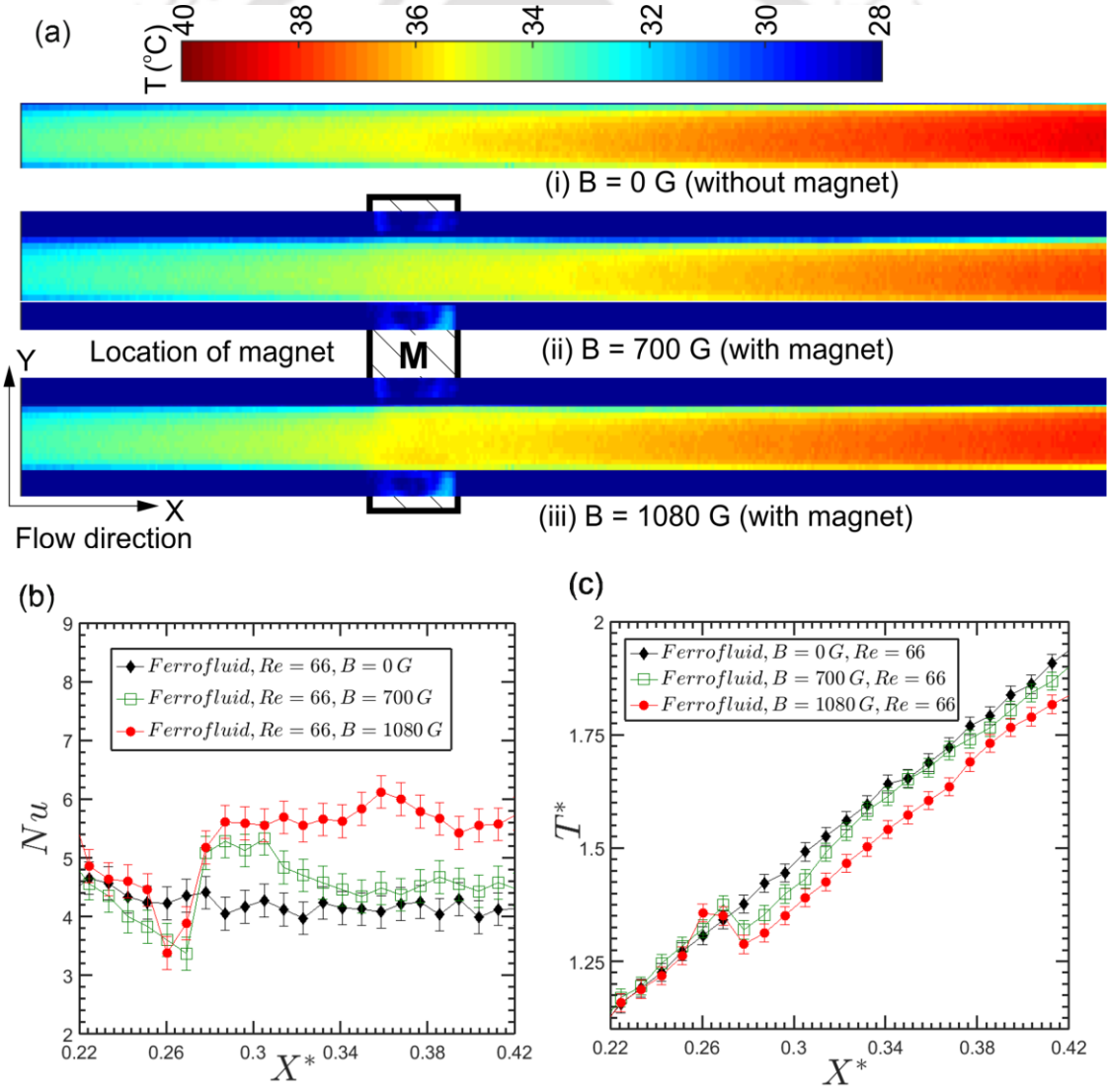

Fig. 3.6 (a) IRT measurements of the heated SS tube when (i) B=0 G, (ii) B=700 G, (iii) B=1080 G for Re=66; Variation of (b) Nusselt number; and (c) non-dimensional wall temperature along the non-dimensional length when the flow field is perturbed by an electromagnet

C. Mechanism of heat transfer under the influence of a constant magnetic field

The available explanations in reported literature for the augmentation of convective heat transfer of ferrofluid under the applied magnetic field are not very coherent. Some of the studies suggested that particle migration enhanced thermophysical properties might be the reasons for augmentation (Ahuja 1975; Wen and Ding 2004; Sommers and Yerkes 2010) while few studies attributed thermomagnetic convection as the dominating mechanism for augmentation (Ganguly et al. 2004; Lajvardi et al. 2010). At the same time, it has been mentioned that thermomagnetic convection is dominant only when a high thermal gradient exists in the flow field, resulting in the occurrence of the magnetic susceptibility gradient. Typically, in most of the single-phase convective heat transfer situations, working temperatures are not so high enough to produce magnetic susceptibility gradients. Thus, the role of thermomagnetic convection in the augmentation of heat transfer can be ignored (very small, if any) in the physical situation of lower operating temperatures, such as in the present case. Philip et al. (2007, 2008) concluded with the help of non-equilibrium molecular dynamic simulations that under the influence of a magnetic field, the ferrofluid forms a chain-like cluster. Similar clustering of the magnetic nanoparticles was also experimentally observed by Asfer et al. (2016). A later study proposed that these chain-like clusters disturb the bulk flow, which in turn leads to augmentation in heat transfer (Asfer et al. 2016).

With this background of information, we attempted to qualitatively visualize the wall thermal footprints and fluid flow domain. To get the thermal footprints of wall temperature in the vicinity of the magnetically active zone, a close-up lens IR lens (1.5x zoom) was used. Figure 3.7(a)-(b) shows the IR thermogram of B = 0 G and 1080 G, and Fig. 3.7(c) shows the image of the flow visualization of ferrofluid flow under the influence of a constant magnetic field. For the sake of clarification, the IR thermogram can be divided into three zones (i) the zone before the magnetic field (BMF), (ii) the zone at the magnetic field (AMF), (iii) the zone after the magnetic field (ATMF). Distinct changes can be seen in the thermal field of $\bar{B}$ = 0 G and $\bar{B}$ = 1080 G in all three zones mentioned above.

The visual inspection of the IR thermogram and bright field image clearly shows the deposition of magnetic nanoparticles (MNPs) on the wall in the vicinity of the magnetically active zone. In addition to that, the inset of Fig. 3.7(c) shows the structure of the deposited chain-like cluster of particles. There might be a tendency to form a similar chain-like cluster of nanoparticles that are dispersed in the bulk fluid. Therefore, the possibilities of modification in the flow field can be enumerated as (a) formation of the hump with irregular

spikes on the surface because of clustering of MNPs, (b) chain-like clustering of the dispersed MNPs in the bulk fluid, (c) imbalance of the resultant forces and couples in the flow field due to the interaction of inertia and magnetic forces. Therefore, the formation of irregular spiked-hump disturbs the flow field by giving rise to secondary flow, enhancing the transport of momentum and energy. Moreover, the dispersed cluster of MNPs can transport the energy efficiently in the bulk medium. Due to the interplay of inertia and magnetic forces in 3D space, those dispersed clusters may feel the imbalance of forces and couples during the flow. Random motion of the dispersed clusters can be generated as a result of the imbalance in forces and couples. This random motion may act as an add-on mechanism to transport of momentum and thermal energy, which is usually unavailable in laminar flow.

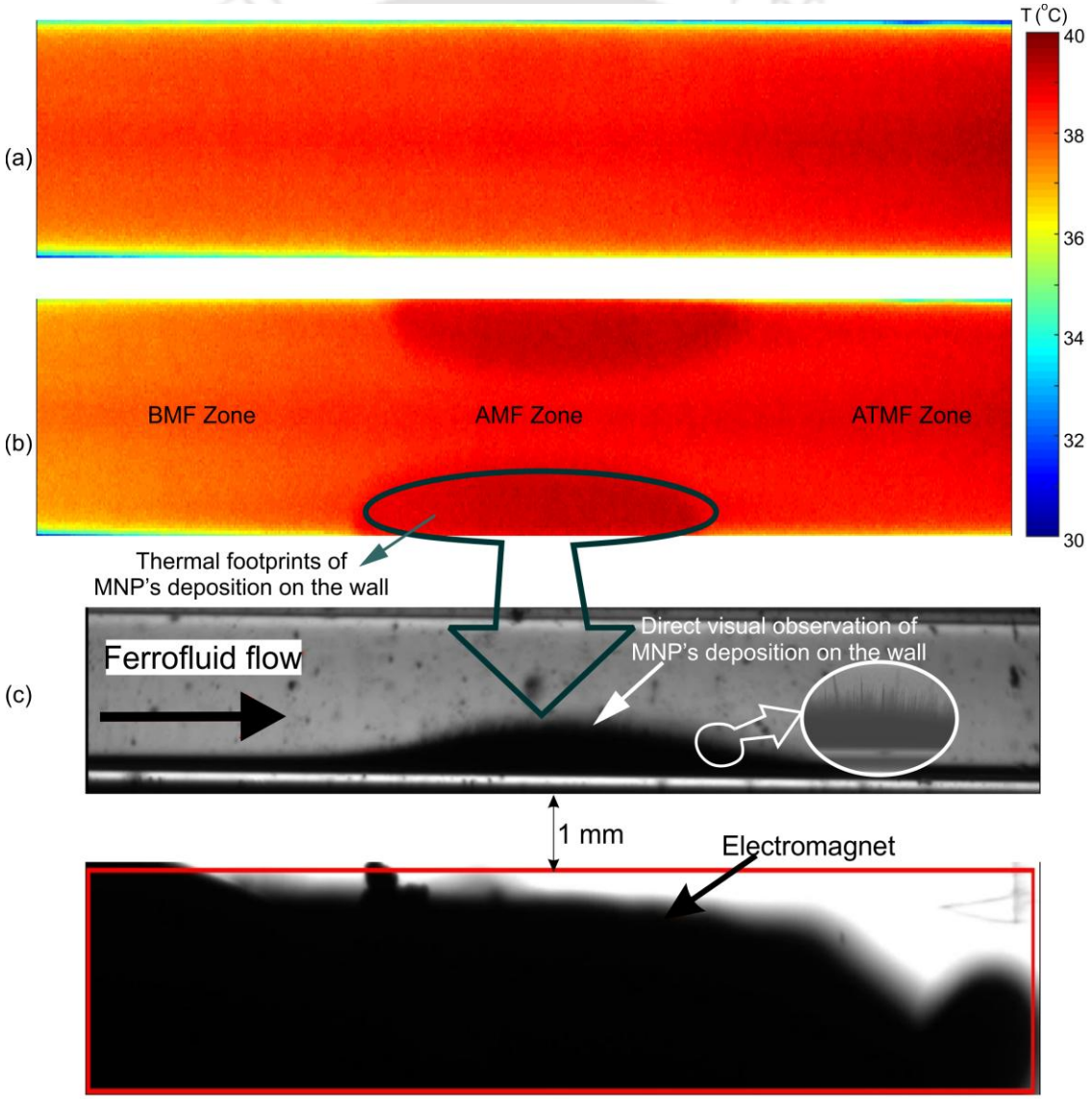

Fig. 3.7 IR thermogram taken with close up IR lens for (a) B=0, (b) B=1080 G for Re=66 (c) Qualitative bright field visualization of ferrofluid flow in a glass capillary.

3.3.4 Convective heat transfer characteristics in presence of time-dependent magnetic field

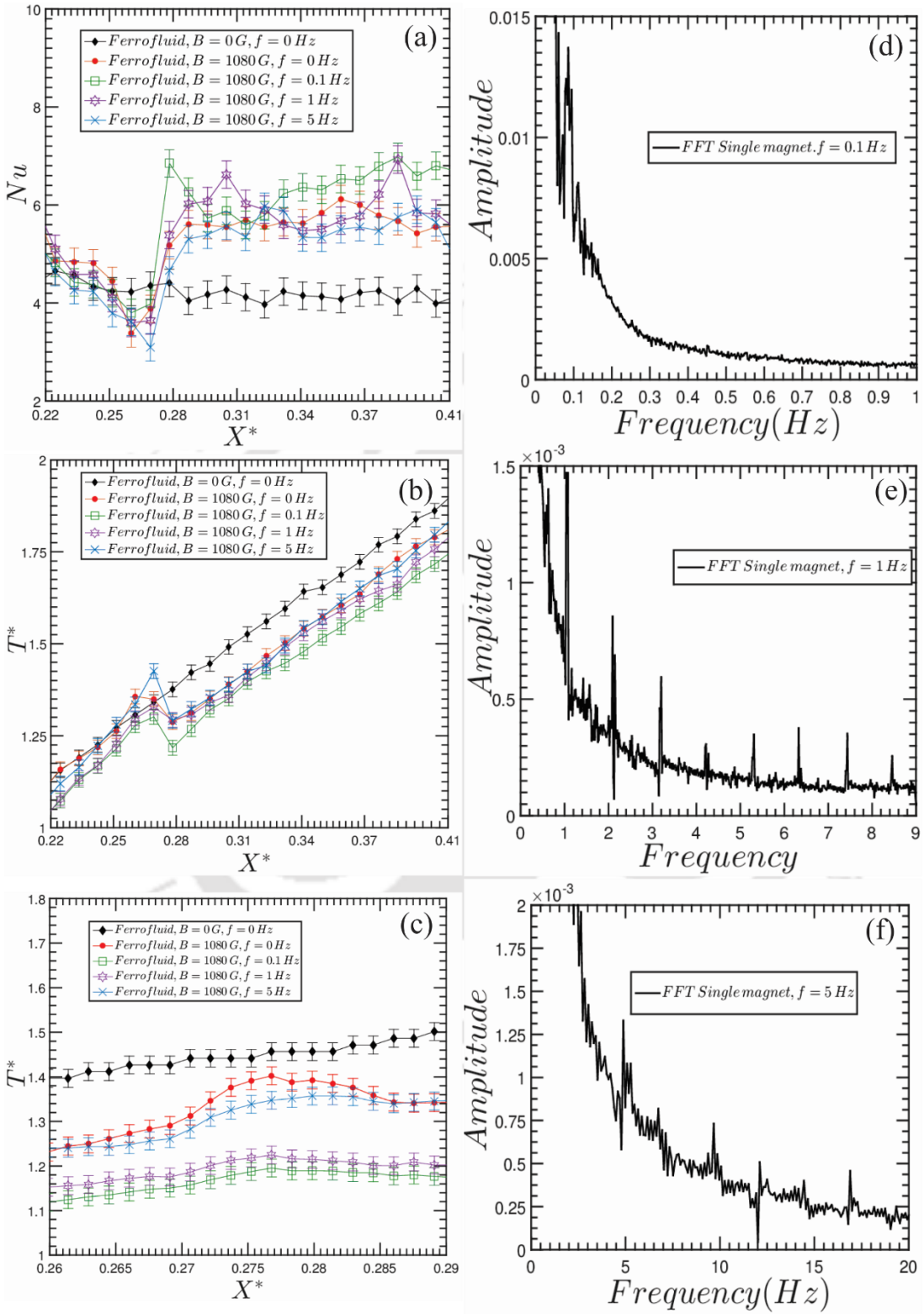

Fig. 3.8 (a) Time-averaged Nusselt number for various frequency; (b) Time-averaged Non-dimensional wall temperature along the non-dimensional length; (c) Close-up view of Non-dimensional wall Temperature taken by close-up IR lens, along the non-dimensional length; Fast Fourier transform of the outlet temperature, for the magnetic field frequency of (d) 0.1 Hz; (e) 1 Hz; (f) 5 Hz.

In the previous section, it has been shown that the application of a constant magnetic field during the convective flow of ferrofluids are advantageous for the enhancement in heat transfer. Flow modifications, in terms of formation of hump and generation of secondary flow, along with the force field interaction (inertia and magnetic force), are the possible reasons to increase the heat transfer. An intuitive question may be posed that what will be the effect of the magnetic field when it is modulated with some frequencies? By doing so, the thermal and hydrodynamic boundary layer is continuously perturbed, which in turn, may give rise to different flow and thermal fields. Also, due to the transient nature of the flow, various involved time scales govern the evolution of the thermal and hydrodynamic flow field. The involved time scales are mainly the magnetic perturbation time scale $(1/f)$, diffusion time scale (L_c^2/α), advective time scale (L_c/U_{av}), and viscous time scale (L_c^2/υ). The time scales involved in the current experimental study have been listed in Table 3.2. Therefore, in this section, the effect of a time-dependent magnetic field, for *Re* = 66 and $\bar{B}$ = 1080 G, on the convective flow of ferrofluid, will be discussed. The frequency of the square wave time-dependent magnetic field (On/Off type) used in the present experiments are 0.1 Hz, 1 Hz, and 5 Hz, respectively.

Table 3.2 Experimental timescales involved in seconds.

Time scale(s)	f=0.1 Hz	f=1 Hz	f=5 Hz
Advective timescale,(L_c/U_{av})	7.71	7.71	7.71
Diffusion timescale, (L_c^2/α)	430000	430000	430000
Magnetic perturbation timescale, $(1/f)$	10	1	0.2
Viscous timescale, (L_c^2/υ)	84000	84000	84000

Table 3.3 Numerical timescales involved in seconds.

Time scale(s)	f=0.5 Hz	f=1 Hz	f=5 HZ	f=10 HZ	f=15 HZ	f=20 HZ
Advective timescale (L_c/U_{av})	1.03	1.03	1.03	1.03	1.03	1.03
Diffusive timescale (L_c^2/α)	4970	4970	4970	4970	4970	4970
Magnetic perturbation timescale, $(1/f)$	2	1	0.2	0.1	0.067	0.05
Viscous timescale, (L_c^2/υ)	950	950	950	950	950	950

With this background, the results of time-dependent magnetic field experiments are shown in Fig. 3.8(a)-(f). Figure 3.8(a)-(c) shows the axial variation of time-averaged Nusselt

number, non-dimensional wall temperature, and zoomed view of non-dimensional wall temperature near the magnetically active zone for different frequencies of the magnetic field. These results are also compared with constant magnetic field cases for $\bar{B}$ = 0 G and 1080 G. It can be seen from the figure that the time-averaged Nusselt number is maximum for a magnetic field frequency of 0.1 Hz while it is a minimum for 5 Hz. Time-averaged Nu values for 5 Hz is almost similar to the case of a constant magnetic field. Additionally, it can also be noted that Nu values are always higher than that of the no magnetic field case, i.e., $\bar{B}$ = 0 G.

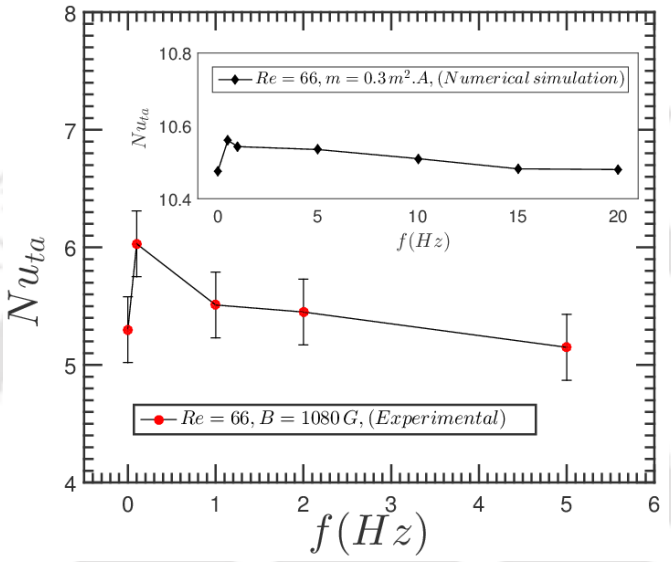

Fig. 3.9 Average Nusselt number for various frequency

As shown earlier, the particles have the tendency to deposit in the vicinity of the magnet location during the flow; now, if the magnetic field is turned off, the deposition might get flushed away due to the shearing action of flow inertia. Therefore, by switching the magnetic field On and Off continuously with some frequencies, the nanoparticles may get deposited during the On cycle and may get flushed away during Off-cycle depending upon the time scales and resultant of magnetic and inertia forces. In other words, both hydrodynamic and thermal boundary layers are getting renewed within the On-Off cycle. To gain insight into the flow dynamics, a clear understanding of the interplay between the involved timescales is required. Interaction of magnetic and inertia force can also be viewed from the corresponding time scale perspective.

For the present study, considering L_c~0.28 m, μ~0.00106 $Pa.s$, α~1.7 × $10^{-7} m/s$, Re~66, the advective time scale, the diffusion time scale, and the viscous time scale of the flow were found out to be around 7.71 s, 460000 s, and 74000 s respectively, as already mentioned in Table 3.2 appropriately. Whereas the perturbation time scale varies

as $10\,s$, $1\,s$, and $0.2\,s$ for the magnetic field frequency of $0.1\,Hz$, $1\,Hz$, and $5\,Hz$ respectively. From this perspective, it can be clearly identified that among the four mentioned time scales in Table 3.2, only the magnetic perturbation time scale and advective time scales are primarily governing the flow and thermal field. If we see the physical phenomena taking place during the On-Off cycle, the effective flushing of deposited particles can only take place during the Off-cycle because the inertia force dominates the flow field. On the other hand, the re-development of hump starts during the On-cycle. Therefore, if the advective time scale is either smaller or at most equal to the time duration of the Off-cycle, then only the hump developed in the previous On-cycle will completely be sheared-off by the flow inertia. This renewal of hump formation and simultaneous mixing of the sheared-off particle in the bulk fluid enhances the momentum and thermal transport. From Table 3.2, it can be observed that in the present experiments, the time duration of Off-cycle of the magnetic perturbation time scale is 5 seconds for $f = 0.1\,Hz$ while the advective time scale is 7.7 seconds. These two time scales are comparable for $f = 0.1\,Hz$ as compared to the other frequencies, i.e., flow inertia is capable in shearing-off the deposition in large proportion at f = 0.1 Hz. Unlike, at higher frequency values of 1Hz and 5 Hz, the hump cannot be sheared-off during the Off-cycle because the advective time scale is significantly higher than the magnetic perturbation time scale. This particular fact confirms the observation of experimental data where the time-averaged Nusselt number is maximum for the magnetic field frequency of $0.1\,Hz$ while it is minimum for $5\,Hz$. The same phenomena are also evident in non-dimensional wall temperatures, as shown in Fig. 3.8(b)-(c). Just to confirm the dominating frequency in the flow field, Fast Fourier Transform (FFT) of the outlet fluid temperature is done and presented in Fig. 3.8(d)-(f). It is found that the dominating frequency of the flow field is corresponding to the applied magnetic field frequency.

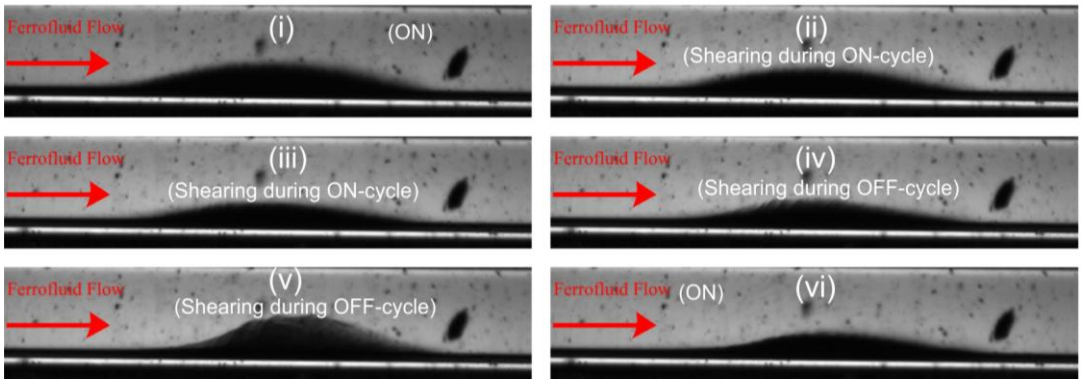

Fig. 3.10 Velocity vectors with non-dimensionalized temperature contours at (a)f = 0.5 Hz, (b) f = 10 Hz for Re=66, m=0.3 m^2-A (c) Time stamps (i-vi) of bright field visualization of ferrofluid flow under alternating magnetic field

Due to the limitations of the designed circuit, the experiments could not be performed for the frequency value of higher than $5\,Hz$. To overcome the limitations of experimental methodologies and to gain insight into the flow and thermal behavior of the ferrofluid flow at higher magnetic field frequencies, two-dimensional numerical simulations were carried out. Although, three-dimensional simulations would have provided a detailed quantitative understanding of the flow dynamics. However, the involved computational cost of such complex coupled flow phenomena could be substantial. Particularly for this reason, in the present numerical investigation, we consider a two-dimensional flow between parallel plates in the presence of two-line dipoles (placed adjacent to the top and bottom wall). The adopted numerical strategies were highlighted appropriately in section 3.2.3. Numerical simulations were performed for magnetic field frequencies of 0.5 Hz, 1 Hz, 5 Hz, 10 HZ, 15 Hz, and 20 Hz. The involved time scale for the numerical simulations can be seen in Table 3.3. It is mandatory to mention here that in simulations contribution of thermomagnetic convection has been neglected. Figure 3.9 shows the variation of the time-averaged Nusselt number for various frequencies of the magnetic field for both numerical simulation and present experimental study. The results of the numerical simulations are given in the inset of Fig. 3.9. A qualitatively similar pattern can be seen for both experimental and numerical studies. It can be observed that for fixed flow Reynolds number Re = 66 and magnetic field intensity $\bar{B}$ = 1080, a threshold frequency exists for which the time-averaged Nusselt number will be maximum. A typical bright field visualization of ferrofluid flow in a glass capillary tube under the influence of a time-dependent magnetic field has been shown in Fig 3.10 (i-vi). The shearing-off and downstream translation of the deposited hump can be clearly seen.

Wall thermal footprint during the flow of ferrofluid under the influence of a time-dependent magnetic field is shown in Fig. 3.11(a)-(c). Aggregation of the MNPs can be clearly noticed at the wall for all three frequencies of the magnetic field. Thermal visualization also reveals that overall wall temperature is lowest for $f = 0.1\,Hz$ while highest for $f = 5\,Hz$ amongst the considered cases here. This result is corresponding to the data presented in Fig. 3.8(b), where the axial variation of the wall temperature has been shown for all three frequencies of the magnetic field. It is necessary to mention that because of the higher thermal inertia of the tube wall, the temporal response of temperature cannot be captured accurately. That is why no qualitative change in the thermal footprints have been found with different time stamps. To get the temporal temperature response, the wall thickness of the tube has to be further lower. This puts the limitation on data generated from the present set-up.

To further understand the intriguing phenomena, the temporal variation of the line averaged wall temperature (i.e., Averaged in the transverse Y-direction) for various frequencies of the magnetic field is shown in Fig. 3.12(a)-(c). The location of the line is chosen in such a way that each one of them belongs to the BMF, AMF, and ATMF zone at their respective non-dimensional locations (X^*) as 0.2635, 0.2772, and 0.2910. Figure 3.12(a) shows the temporal variation of the line averaged temperature for magnetic field frequency of 0.1 Hz. As mentioned previously, the location $X* = 0.2635$ belongs to the BMF zone i.e., the upstream zone of the magnetic field, $X* = 0.2772$ belongs to the AMF zone, i.e., at the centerline of the magnetic field, and $X* = 0.2910$ belongs to the ATMF zone, i.e., the downstream zone of the magnetic field. Now, it can be clearly observed from the figure that there is a rise in wall temperature at the AMF zone because of the deposition of MNPs, and the mode of heat transfer from the wall to deposition is mainly conduction dominated.

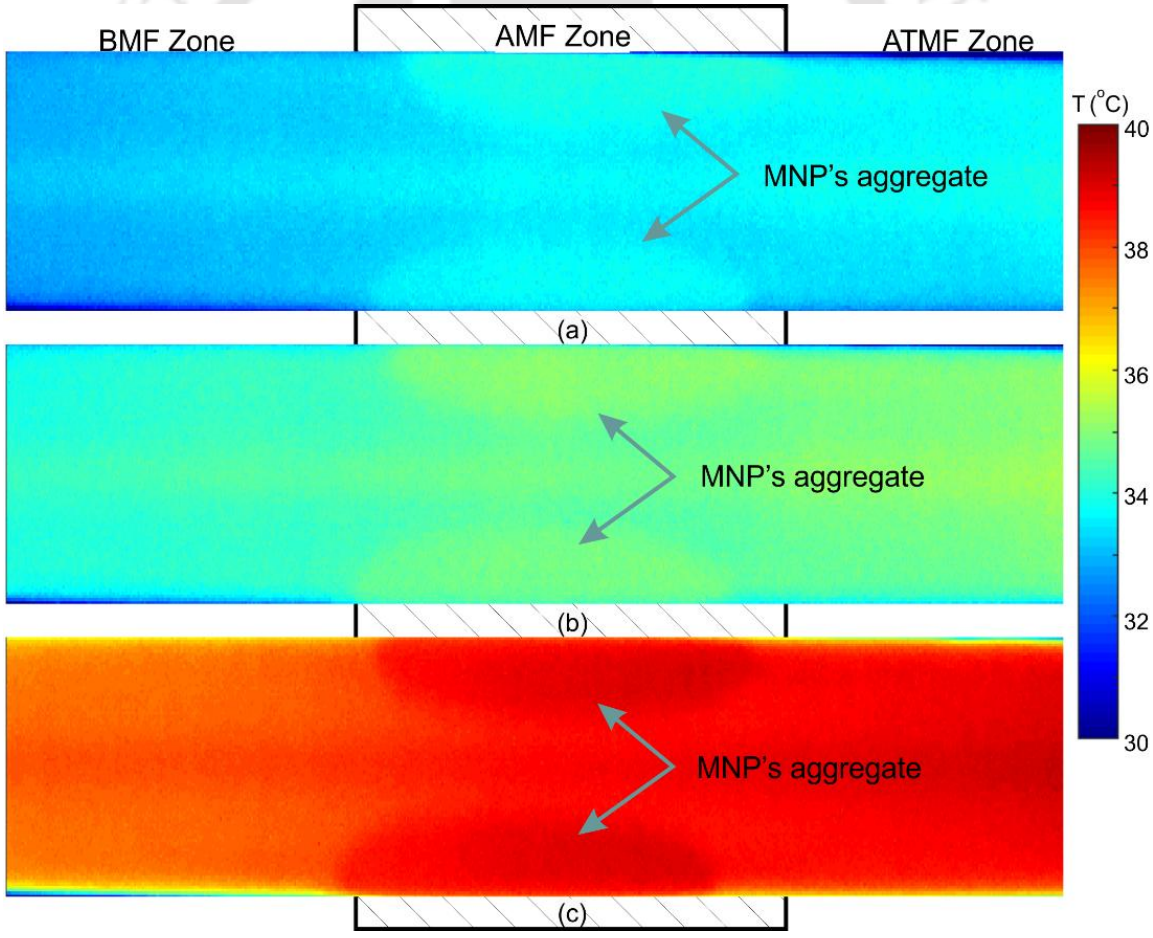

Fig. 3.11 IR thermogram take with close up IR lens for (a) f=0.1 Hz; (b) 1 Hz; (c) 5 Hz; for B=1080 G,Re=66.

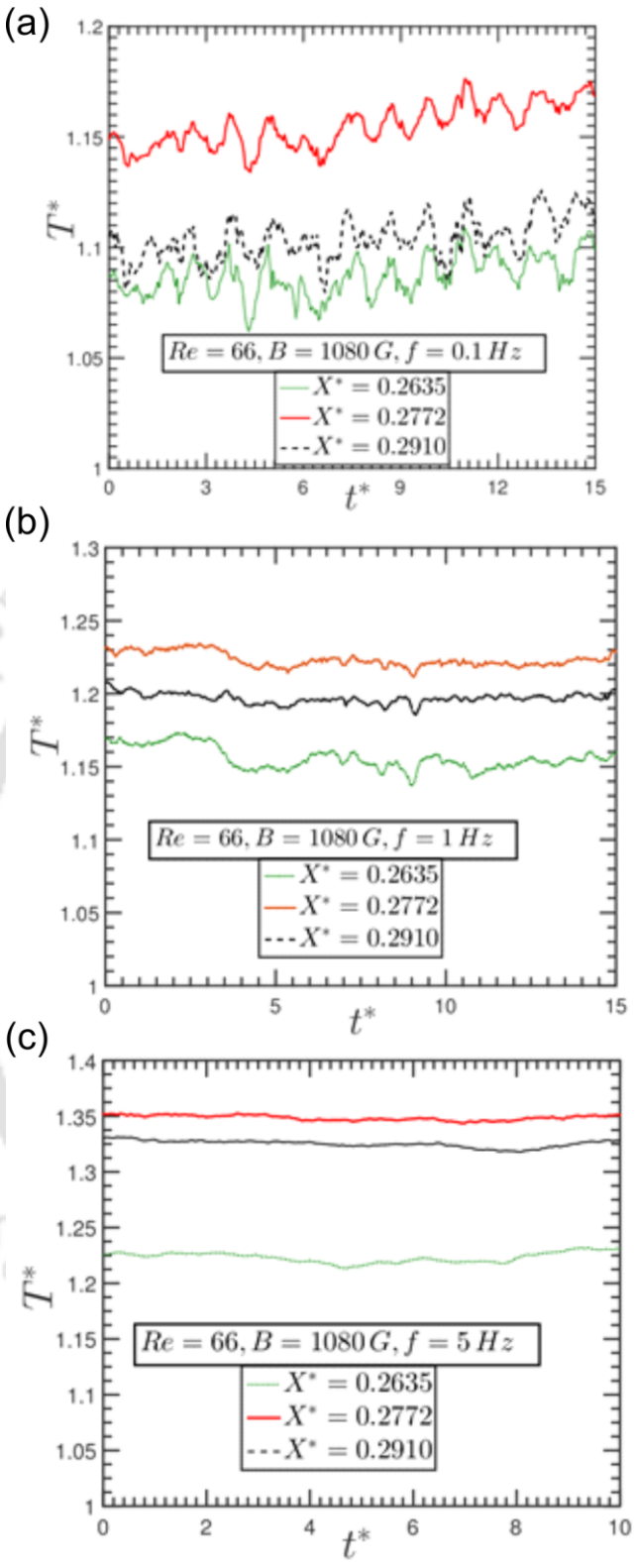

Fig. 3.12 Transverse direction averaged wall temperature at various location for (a) f=0.1 Hz; (b) 1 Hz; (c) 5 Hz; for $\bar{B}$=1080 G, Re=66.

In the downstream locations of the AMF zone, a significant drop in the wall temperature has been observed. This can be attributed to the formation of a recirculation bubble at the downstream location, which falls in the wake of the spiked hump. Similar

observations can be done for the other cases of 1 Hz and 5 Hz shown in Fig. 3.12(b)-(c), but the magnitude of the wall temperature is higher for these cases as compared to the frequency of 0.1 Hz. Thus, it can be conditionally concluded that providing intermittent perturbation to the flow and thermal domain of the ferrofluid under the influence of a magnetic field leads to enhancement in the heat transfer. At the same time, monotonically increasing the perturbation frequency does not lead to any heat transfer augmentation. In such a case, the role of the interplay among the involved timescale should be given paramount importance in order to gain a deep insight into the heat transfer dynamics of the flow field.

3.4 SUMMARY

In many mini/microscale applications, because of the geometrical constraint, the flow remains laminar and has limited thermal energy transport characteristics. Perturbations of the single-phase flow by means of an external magnetic field can be an effective strategy for augmentation in heat transfer. In the present study, the convective heat transfer characteristics of single-phase ferrofluid flow in heated stainless steel tube under the influence of constant and alternating magnetic field has been studied experimentally as well as numerically. The major conclusions of the study are as follows:

- No augmentation of heat transfer is seen for the ferrofluid flow in the absence of a magnetic field compared to its carrier fluid, i.e., water. The negligible influence of the thermophysical properties of ferrofluid is seen on the convective heat transfer characteristics in the absence of a magnetic field.
- When the constant magnetic field is applied externally to the flow field, a hump-like structure develops results in the generation of secondary flow. At the immediate downstream location, a drop in wall temperature has been observed, which leads to enhancement in heat transfer takes place. By the application of a constant magnetic field, the enhancement in the heat transfer as compared to no magnetic field case was found to be 23%.
- The possible mechanism for improvement in thermal behavior can be enumerated as (a) formation of the hump with irregular spikes on the surface because of clustering of MNPs, (b) chain-like clustering of the dispersed MNP's in the bulk fluid, (c) imbalance of the resultant forces and couples in the flow field due to the interaction of inertia and magnetic forces.

- When the flow field is perturbed by a time-dependent magnetic field, the augmentation process governed by the interplay of the involved time scale, mainly the advective time scale and the magnetic field perturbation time scale. For a given *Re* and $\bar{B}$. There has to be a threshold frequency at which the maximum heat transfer can be observed. In the present study, maximum enhancement in the heat transfer was approximately found to be 39 % for the magnetic field frequency of 0.1 Hz.

Chapter 4

EFFECT OF TIME-DEPENDENT MAGNETIC FIELD ON THE INTERNAL HYDRODYNAMICS OF A SESSILE FERROFLUID DROPLET

In this study, the internal hydrodynamics of a ferrofluid droplet in the presence of a magnetic field driven ambiance is explored. A sessile ferrofluid droplet is kept on a PDMS substrate and subsequently perturbed by a time-dependent magnetic field. Both bright-field visualization and μ-PIV measurement techniques are employed for investigating the internal dynamics of the magnetically perturbed ferrofluid droplet. Through the bright field visualization, we explore the transient motion of the magnetic nanoparticles, while via μ-PIV, we investigate the implications of the magnetic nanoparticles motion on the convective features of the flow. An important finding of the magnetic nanoparticles motion as a combined function of the magnetic flux density and applied frequency of the magnetic field is highlighted, which is unique to the scenario of time-dependent magnetic perturbations.

4.1 INTRODUCTION

Exploring the internal hydrodynamics of a magnetically perturbed ferrofluid droplet is of critical importance from the perspectives of droplet evaporation, spreading, mixing, and many more (Roy et al. 2009; Ahmed et al. 2018a; Saroj and Panigrahi 2019). In this chapter, the internal hydrodynamics of a sessile ferrofluid droplet in the presence of a time-dependent magnetic field is experimentally explored. Both bright-field visualizations and μ-PIV measurements were employed to investigate the flow characteristics of the ferrofluid droplet in the presence of a magnetic field. A time-dependent magnetic field with different actuation frequencies was allowed to perturb the ferrofluid droplet. The magnetic field flux density was maintained constant at 340 G, while the frequencies were varied from 0.1 Hz to 3Hz. The results are presented as such; initially, we explored the motion of the magnetic nanoparticles in the presence of a magnetic field. In the later part of the chapter, we discuss the implication of the MNPs motion on the bulk liquid of the ferrofluid droplet domain via μ-PIV measurement technique.

4.2 MATERIALS AND METHODS

4.2.1 Fabrication of hydrophobic substrate and electromagnet

The preparation of the PDMS substrate is elaborately explained in section 2.6 of chapter 2. For the contact angle measurements of droplets, a goniometer imaging set-up (Make: Acam-NSC) was used (refer to section 2.2 of chapter 2 for details). The contact angle of water on the PDMS coated glass slide was found to be 105 ± 0.8°, whereas for untreated surface, i.e., for glass slide, it was found to be 44 ± 0.6°. Similarly, the contact angle was found to be 65°, and 34° for ferrofluid on the PDMS coated glass slide and the untreated glass slide, respectively. An electromagnet was kept at a distance of 1.5 mm from the droplet, as shown in Fig. 4.1(a)-(b). The details regarding the fabrication of the electromagnet are elaborately discussed in section 2.5 of chapter 2. Time-dependent magnetic field of strength $\bar{B}$ = 340 G and actuation frequencies $f = 0.1, 0.5, 1.0$, and 3 Hz were applied to the ferrofluid droplet. Figure 4.1(c) shows the evaporation of the ferrofluid droplet in the presence of no magnetic field up to $t = 400$ s. The role of evaporation in the present study was found to be negligible, as can be observed from Fig. 4.1(c).

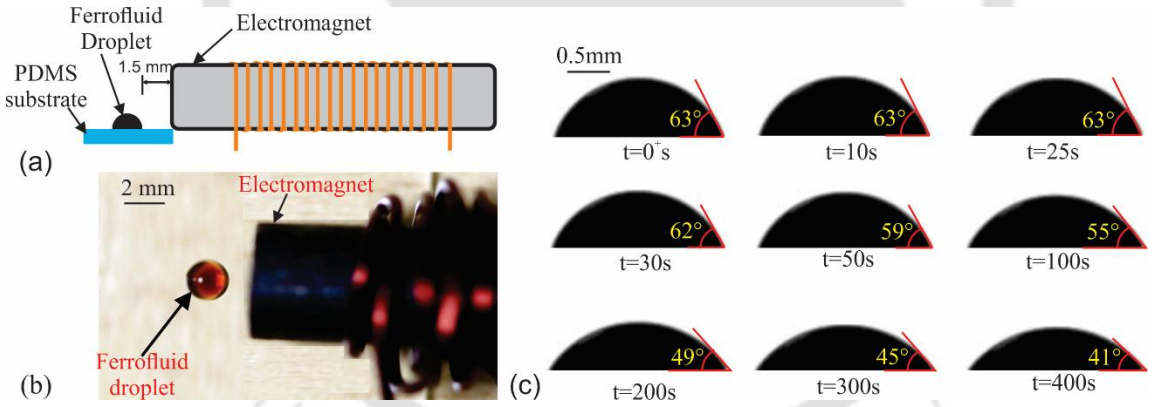

Fig. 4.1 (a) Schematic of the droplet - electromagnet arrangement, (b) The fabricated electromagnet along with the sessile droplet on a PDMS coated substrate, and (c) Snapshots showing the rate of evaporation of the ferrofluid droplet in the absence of magnetic field.

4.2.2 Bright-field imaging and μ-PIV system

Bright field visualizations of internal convection of the ferrofluid droplet were carried out using an inverted microscope (Leica: DM IL LED), as shown in Fig. 4.2. The droplet – electromagnet set up was kept over the stage of the inverted microscope, and the droplet was illuminated from below the microscope stage through a $10X$ objective lens (NA = 0.40) using a mercury lamp. Under bright-field visualizations mode, nanoparticles of ferrofluid appeared as black particles with a white background. To visualize the chain-like cluster of nanoparticles during aggregation, a higher magnification objective lens 20X (NA = 0.4) was used.

Similarly, during µ-PIV measurements of internal convection of ferrofluid droplet, an inverted microscope with a fluorescent light source was used, as shown in Fig. 4.2. Figure 4.2 shows the schematic of the µ-PIV system. The µ-PIV system is discussed in detail in section 2.4 of chapter 2. For the µ-PIV measurements, the ferrofluid droplet was seeded with 1 µm diameter fluorescent microspheres (Molecular Probes Inc.). The above seeding particle concentration was chosen as it provided acceptably low noise levels under the present illumination conditions. The droplet–electromagnet set up was kept over the stage of the inverted microscope, and the droplet was illuminated by a monochromatic of wavelength of 530 nm from below the microscope stage through a 10X objective lens (NA = 0.40). The details regarding the capture of images and the µ-PIV methodology are discussed in detail in section 2.4 of chapter 2.

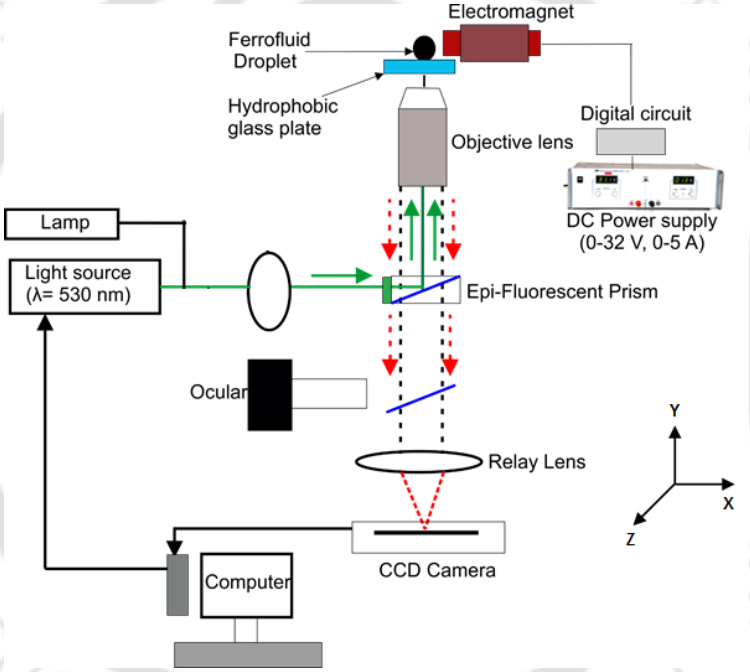

Fig. 4.2 Schematic of the bright field imaging/µ-PIV set up

Similarly, the details of the preparation and characterization of the ferrofluid solution are sufficiently mentioned in section. 2.7 of chapter 2. In the present study, the volume fraction of magnetic nanoparticles in ferrofluid is maintained at 0.5%. The various thermophysical properties of the ferrofluid are mentioned in Table 4.1.

Table 4.1 Thermophysical properties of water and prepared ferrofluid

	Density ($Kg\ m^{-3}$)	Specific heat ($J\ (Kg\ K)^{-1}$)	Thermal conductivity ($W\ (m\ K)^{-1}$)	Viscosity (Pa s)
Water	995	4180	0.6±0.05	0.0009
Ferrofluid	1022	3425	0.7±0.05	0.00106

4.3 RESULTS AND DISCUSSION

4.3.1 Magnetic flux density distribution

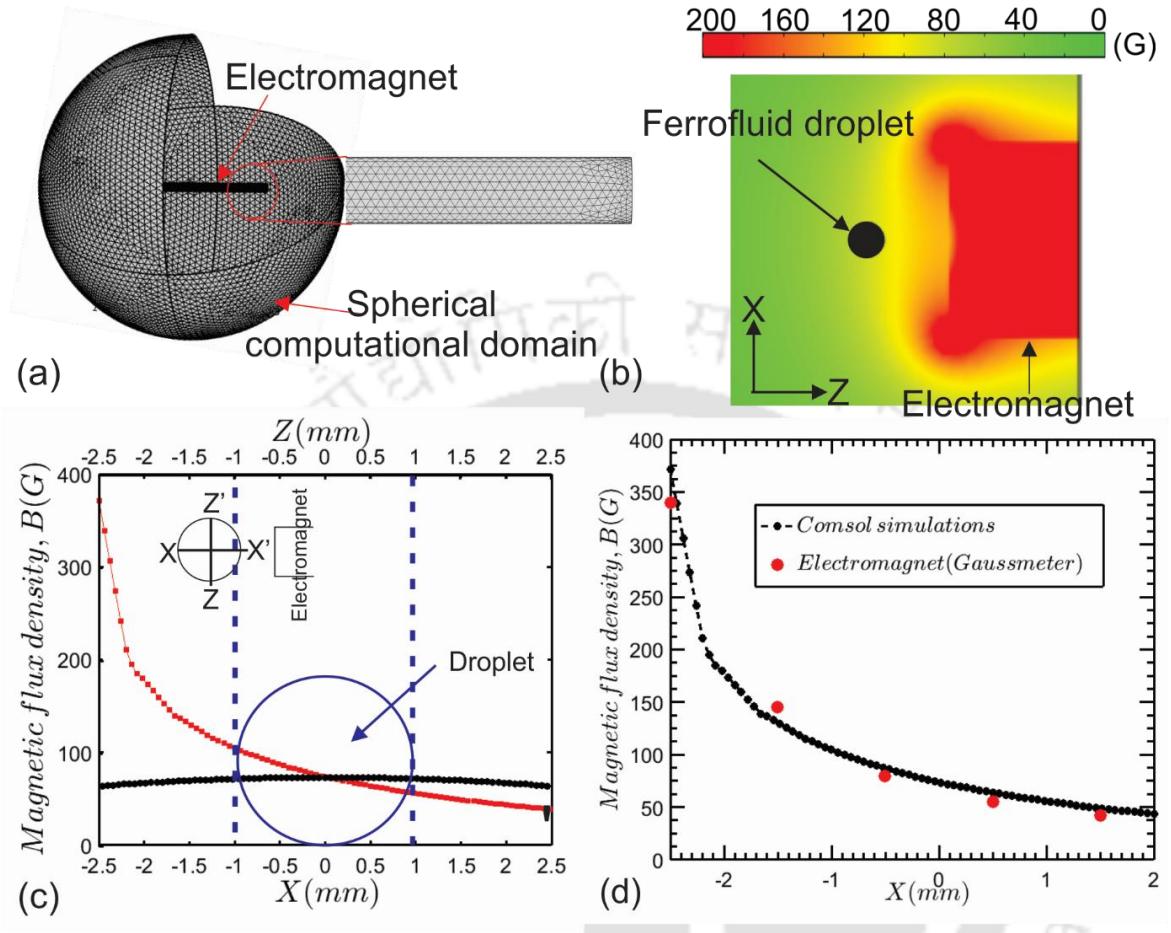

Fig. 4.3 (a) Meshing of the computational domain of the magnetic field (b) Distribution of magnetic flux density ($\bar{B}$) around the droplet region (c) variation of magnetic flux density along the diameters ($X - X'$ and $Z - Z'$) of the droplet and (d) validation of simulation results with measurements from gauss meter.

The distribution of magnetic flux density ($\bar{B}$) in the droplet region was simulated using the COMSOL Multiphysics®. The governing equations and parameters used for the simulation of the magnetic field are presented in Table 4.2. A free tetrahedral mesh of maximum element size of 1 mm, with a total of 2.1×10^6 elements, was used in the present simulations, as can be seen from Fig. 4.3(a). A stationary MUMPS solver with absolute tolerance of 10^{-6} was used for simulating the magnetic field generated by the electromagnet. Figure 4.3(b) shows the simulated magnetic flux density distribution around the droplet. Along the diameter $Z - Z'$ of the droplet, the magnetic flux density was found to be nearly constant, whereas a magnetic field gradient was present along the diameter $X - X'$ of the droplet as shown in Fig. 4.3(c). In order to validate the simulation results, the magnetic flux density produced by the electromagnet was measured using a gaussmeter and was compared

with the simulation results, as shown in Fig. 4.3(d). A good match between the two validates the various parameters and equations used for the simulation of the magnetic field.

Table 4.2 Governing equations and parameters used for COMSOL simulation of the magnetic field

Governing Equations	$\sigma(\partial \bar{A}_m/\partial t) + \nabla \times (\mu_0^{-1} \cdot \mu_r^{-1} \cdot \bar{B}) - \sigma \bar{u}_c \times \bar{B} = \bar{J}_e$ $\bar{B} = \nabla \times \bar{A}_m$ $\bar{J}_e = (N\bar{I}/a_{coil})$
Current (I)	$1.5\ A$
Cross section area of coil (a_{coil})	$2.82 \times 10^{-5}\ m^2$
Number of turns (N)	200
Electrical conductivity of coil (σ)	$5.96 \times 107\ s/m$
Relative permeability of air (μ_r)	1

4.3.2 Scaling analysis

Various scaling analysis were carried out in the present work. The first scaling analysis was carried out for the translational motion of the ferrofluid droplet towards the electromagnet from the position where it was originally deposited on the PDMS coated glass slide. In the presence of a magnetic field, the resultant of surface tension and magnetic force acting on the droplet determines the translational motion of the droplet towards the electromagnet. For the present study above, two forces were evaluated by calculating the Weber number ($We_m = \mu_0|M^2|U/\gamma\, A_s$) and magnetic Bond number ($Bo_m = \mu_0|H^2|R/\gamma$), respectively. Weber number was found to be $We_m \sim 10^{-3}$ as compared to $Bo_m \sim 0.146$, indicating higher dominance of surface tension compared to the magnetic force resulting in a negligible shape change of droplet with no translational velocity towards the electromagnet. The droplet was therefore observed to actuate at the same position in the presence of a magnetic field where it was initially deposited on the PDMS coated glass slide.

A second scaling analysis was carried out to find the amount of negative magnetophoresis acting on seeding particles in ferrofluid in the presence of a magnetic field during µ-PIV measurements. The negative magnetophoresis is usually encountered by a non-magnetic body like seeding particles dispersed in a magnetic medium like ferrofluid in the presence of a magnetic field (Liang et al. 2013; Zhu et al. 2014). Zhu et al. carried out an analytical study on the transport of non-magnetic particles in a diluted ferrofluid in the presence of a magnetic field produced by a permanent magnet (Zhu et al. 2011). They reported that the deflection of non-magnetic particles due to negative magnetophoresis could be minimized with the use of diluted ferrofluids and low strength of the applied magnetic field. The negative magnetophoretic force (F_{mp}) and viscous drag force (F_d) acting on seeding

particles under the present experimental conditions were calculated and the ratio between the two was found to be $\frac{F_{mp}}{F_d} \sim 10^{-7}$, indicating negligible deflection of seeding particles due to negative magnetophoresis. Therefore seeding particles were observed to follow the bulk flow faithfully inside the droplet in the presence of magnetic field during the μ-PIV measurements.

4.3.3 Internal hydrodynamics of ferrofluid droplet in the absence of magnetic field

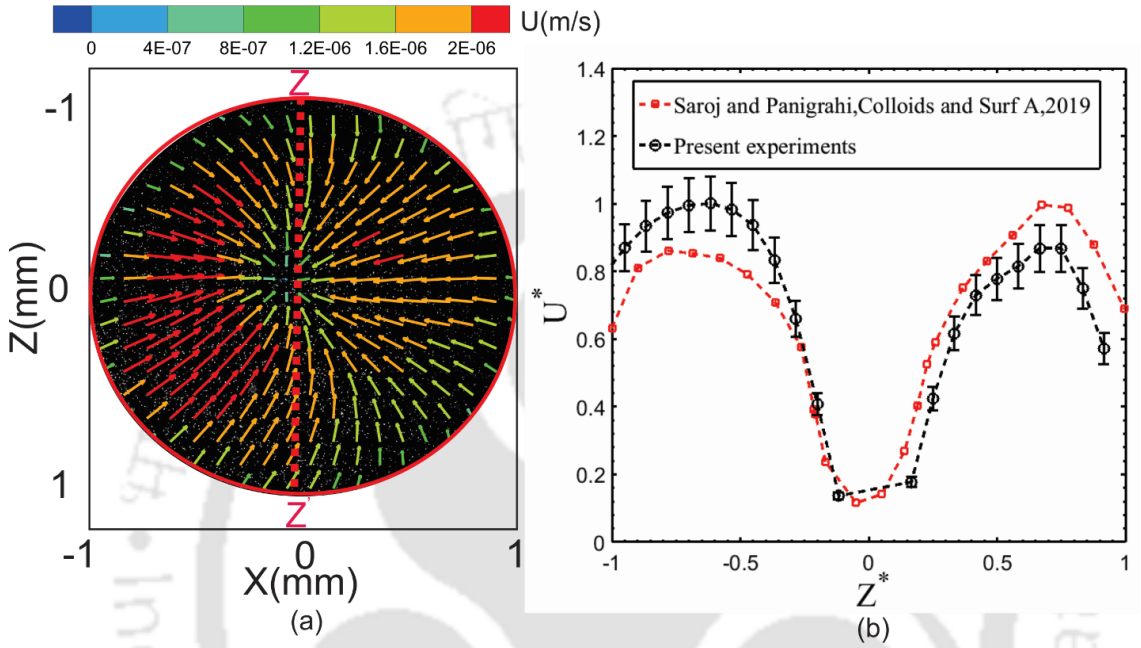

Fig. 4.4 (a) Velocity field inside the ferrofluid droplet in the absence of a magnetic field, and (b) comparison of U^* velocity profile along the diameter $(Z - Z')$ of the droplet with the literature.

Before conducting experiments in the presence of a magnetic field, the internal convection or bulk flow present inside the ferrofluid droplet was measured in the absence of a magnetic field using μ-PIV measurements. Ferrofluid, in the absence of a magnetic field, behaves like any other nanofluid with nanoparticles freely dispersed in the carrier fluid. Several studies have been carried out on internal hydrodynamics of a sessile liquid droplet over a hydrophobic surface, where buoyancy-driven Rayleigh convection results in the downward motion of fluid along the interface and an upward plume-like flow at the center region of the droplet (Fischer 2002; Pradhan and Panigrahi 2015, 2018; Saroj and Panigrahi 2019). Figure 4.4(a) shows the velocity field inside the ferrofluid droplet in the absence of a magnetic field, which shows a radial inward motion towards the center region of the droplet, similar to the studies discussed above. The inward motion of the fluid resulted in a plume-like flow in the central region, which was subsequently traveled towards the contact line region near the air-liquid interface of the droplet. In order to validate our study, a comparison

of U^*-velocity profile along the diameter of the ferrofluid droplet is carried out with the literature, as shown in Fig. 4.4(b). A good match between the two validates the present study and confirms the feasibility of using the μ-PIV technique for velocity measurements of nanofluids like ferrofluids.

4.3.4 Internal hydrodynamics of droplet in the presence of magnetic field

The rate of evaporation of the ferrofluid droplet was observed to be negligible for $t < 30$ s, as discussed in section 4.2.1. This indicates that bright field visualizations and μ-PIV measurements of internal hydrodynamics of ferrofluid in the presence of a magnetic field can be conducted precisely up to time scale $t < 30$ s considering negligible evaporation from the ferrofluid droplet. The maximum time scale corresponding to actuation frequency $f = 0.1$ Hz of the applied magnetic field was calculated to be $t = 10$ s, which was found to be less than the time scale for negligible evaporation, i.e., $t < 30$ s.

A. Bright field visualizations

The ferrofluid droplet was subjected to a time-varying magnetic field of strength $\bar{B}$ = 340 G and actuation frequencies $f = 0.1, 0.5, 1$, and $3\ Hz$. Bright field visualizations were carried out for each case and are shown in Fig. 4.5, respectively. For each case, bright field images are shown at time intervals $\zeta = 0^+$, 0.25, 0.5, 0.75, and 1, respectively, as shown in Fig. 4.5(a). The timestamp $\zeta = 0^+$ represents the instant when the magnetic field was just ON, resulting in the actuation of the ferrofluid droplet in the direction of the applied magnetic field. During the ON cycle of the electromagnet ($\zeta = 0^+ - 0.25$), the magnetic nanoparticles (MNPs) in ferrofluid were observed to migrate through the droplet towards the magnetic zone near the vicinity of the electromagnet. The migration of nanoparticles resulted in a bulk motion of the carrier liquid towards the contact line near the vicinity of the electromagnet. In the presence of a magnetic field, the interparticle dipole-dipole interaction resulted in a chain-like cluster of nanoparticles within the aggregate near the contact line, as shown in the zoomed view in Fig. 4.5(b) (Mendelev and Ivanov 2004). In the absence of a magnetic field, the random orientation of magnetic moments of nanoparticles resulting in the negligible dipolar attraction between the nanoparticles. However, in the presence of a magnetic field, magnetic moments of nanoparticles are orientated in the direction of the applied magnetic field, resulting in a chain-like cluster of nanoparticles, as shown in Fig. 4.5(b). During the OFF cycle of the electromagnet ($\zeta = 0.5,\ 0.75, 1$), nanoparticles were observed to disintegrate

from the chain like clusters and were dispersed freely within the droplet, as shown in Fig. 4.5(b). This was because of the random orientation of magnetic moments of nanoparticles in the absence of a magnetic field, as discussed above. Similar to the migration of nanoparticles, the dispersion of nanoparticles during the OFF cycle resulted in a bulk motion of ferrofluid in the direction opposite to the ON cycle.

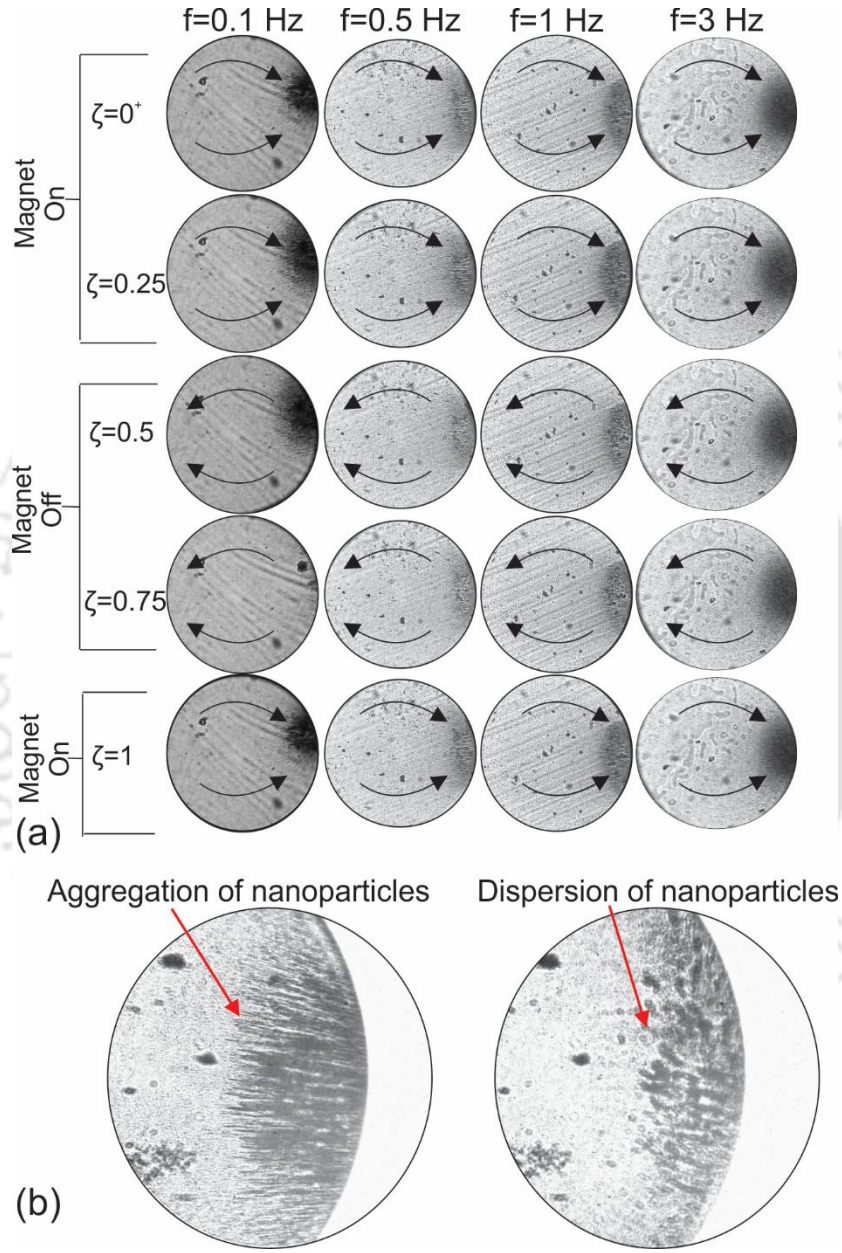

Fig. 4.5 (a) Bright field visualizations of the aggregation and dispersion of nanoparticles inside the ferrofluid droplet in the presence of magnetic field and (b) zoomed view of aggregation and dispersion of nanoparticles at the contact line of the droplet. $\zeta = t/T_M$, where T_M is the time of operation of the electromagnet.

In order to study the effect of actuation frequencies on the migration and dispersion of MNPs in the droplet, various time scales involved with the present study were evaluated, such as; advective time scale (t_u), diffusion/viscous time scale (t_v), and magnetic

perturbation time scale (t_m). All the above timescales were calculated for each case of actuation frequency and are mentioned in Table 4.3. As the advective time scale t_u was found to be very high and constant for all the cases; the effect of the advective time scale is not discussed further. Therefore, the migration, aggregation at the contact line, and then dispersion of nanoparticles during one complete cycle of operation of the electromagnet were found to depend on the balance between the viscous time scale t_v and magnetic perturbation time scale t_m. During the ON cycle of magnetic field, aggregation of nanoparticles was observed in the droplet for a time interval $\zeta = 0$ to 0.25 as shown in Fig. 4.5(a)-(b). This is because, during the time interval $\zeta = 0$ to 0.5, nanoparticles experienced higher magnetic force compared to viscous force resulting in aggregation of nanoparticles in the droplet. The time interval $\zeta = 0.5$ corresponds to case when the magnetic field was just OFF. During the OFF cycle, i.e., from $\zeta = 0.5$ to 0.75, strong dominance of the viscous force compared to the magnetic force acting on nanoparticles resulted in the release/disperse of nanoparticles from the cluster of nanoparticles, as shown in Fig. 4.5(a)-(b). Both migration and dispersion of nanoparticles during the ON and OFF cycle of the magnetic field resulted in a bulk motion of ferrofluid in the droplet.

Table 4.3 Calculation of various time scales in seconds

Time scale (s)	Actuation frequencies (f)			
	$0.1\ Hz$	$0.5\ Hz$	$1\ Hz$	$5\ Hz$
Advective timescale $(2R/U_{B=0})$	300	300	300	300
Diffusion timescale $(4R^2/v)$	2.413	2.413	2.413	2.413
Magnetic perturbation timescale $(1/2f)$	5	1	0.5	0.166

It can be clearly observed that as the magnetic perturbation time scale increases (with the decrease in actuation frequency), the amount of aggregation of nanoparticles in the droplet increases, as shown in Fig. 4.5. This is because, at lower actuation frequencies, the magnetic perturbation time scale was found to be higher as compared to viscous time scale resulting in the migration of more nanoparticles towards the contact line during the ON cycle. Similarly, during the OFF cycle in case of lower actuation frequencies, aggregated nanoparticles from the ON cycle experienced a higher viscous time scale resulting in either complete or partial dispersion of nanoparticles from clusters of aggregated nanoparticles, as shown in Fig. 4.5. A critical actuation frequency was observed ($f_{cr} = 0.5$ Hz), above which no dispersion of nanoparticles from the aggregated nanoparticles at the contact line was observed during the OFF cycle of the magnetic field. This is because the magnetic perturbation time scale t_m corresponding to frequencies above the critical frequency f_{cr} results in less relaxation time

available for dispersion of nanoparticles from the aggregated nanoparticles during the OFF cycle of the magnetic field.

B. μ-PIV measurements

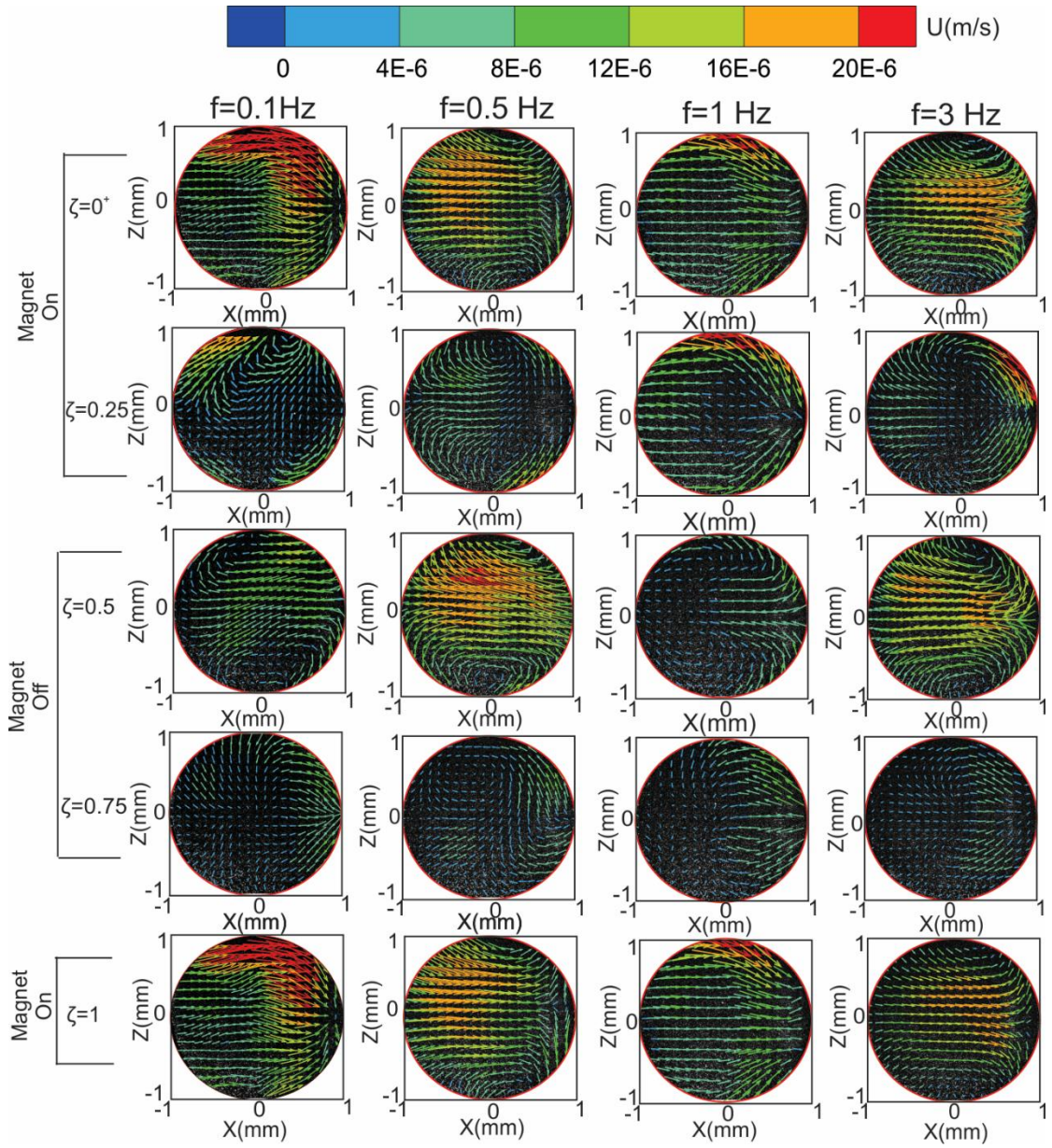

Fig. 4.6 Instantaneous velocity field inside the ferrofluid droplet in the presence of a magnetic field for different actuation frequencies. $\zeta = t/T_M$, where T_M is the time of operation of the electromagnet.

Figure 4.6 represents the temporal variation of the flow field inside the ferrofluid droplet in the presence of a time-dependent magnetic field with actuation frequencies f = 0.1, 0.5, 1, and 3 Hz, respectively. It can be clearly observed that on the activation of the magnetic field, a bulk motion towards the direction of the electromagnet was observed inside the droplet, as evident from the velocity vectors (Left → Right) as shown in Fig. 4.6. This is

because of the migration of nanoparticles towards the contact line near the vicinity of the electromagnet during the ON cycle, as discussed in the previous section.

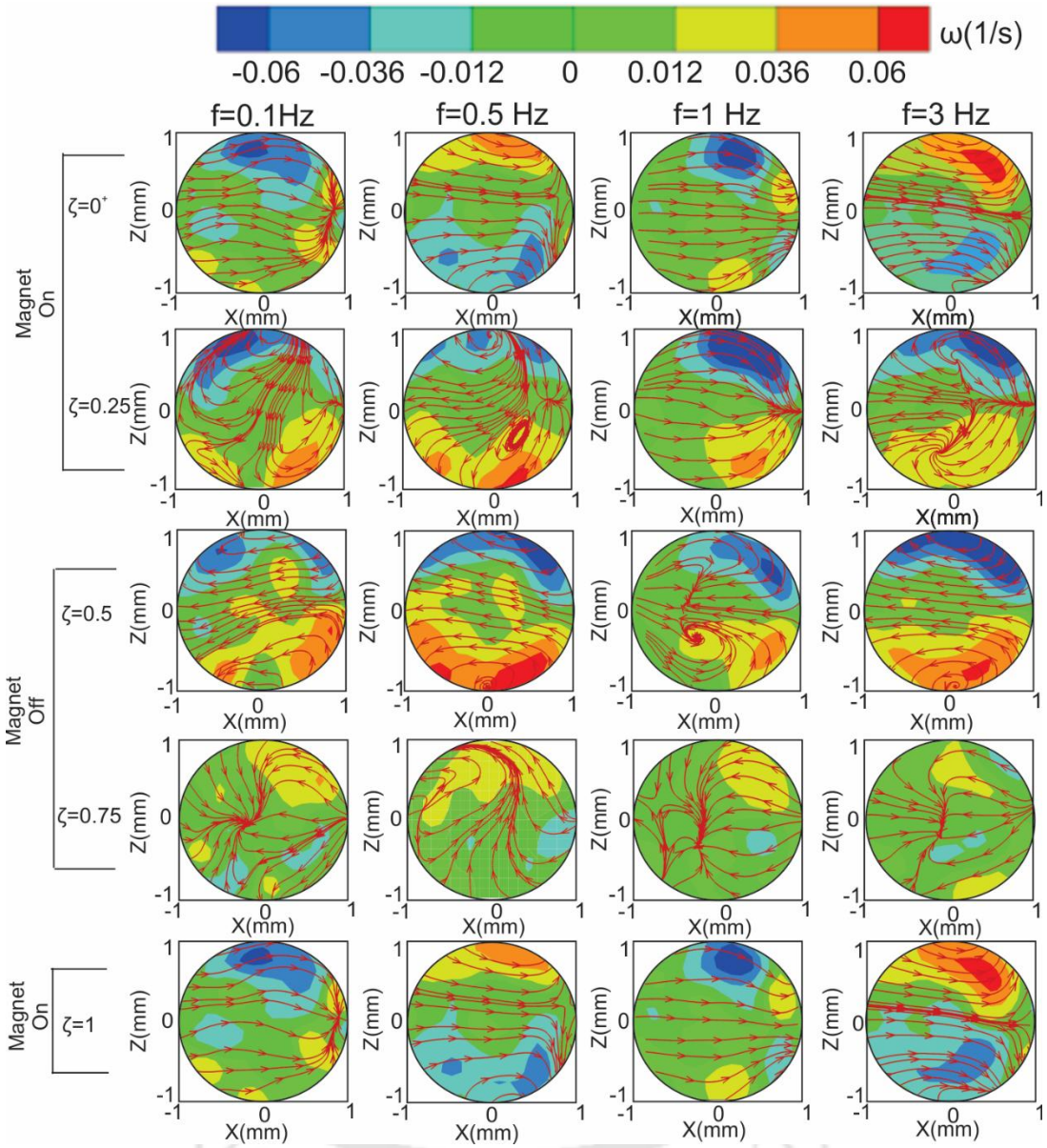

Fig. 4.7 Instantaneous vorticity and corresponding streamlines inside the ferrofluid droplet in the presence of a magnetic field of different actuation frequencies. $\zeta = t/T_M$, where T_M is the time of operation of the electromagnet.

Similarly, during the OFF cycle, a bulk motion was observed inside the droplet in the direction opposite to the ON cycle, as shown by the velocity vectors (Right → Left) in Fig. 4.6. This bulk motion inside the droplet was resulted from dispersion of nanoparticles from the aggregated nanoparticles during the OFF cycle, as discussed in the previous section. For all the cases of actuation frequencies, the magnitude of the velocity of bulk flow inside the droplet was observed to decrease from time instant $\zeta = 0^+$ to $\zeta = 0.25$ during the ON cycle, as shown in Fig. 4.6. This is because of continuous aggregation of nanoparticles at the contact

line from $\zeta = 0^{+} - \zeta = 0.25$, which reduces the strength of the magnetic field inside the droplet resulting in the lower magnetic force acting on nanoparticles at $\zeta = 0.25$. During the OFF cycle, the magnitude of bulk motion inside the droplet was observed to be less as compared to the ON cycle, as shown in Fig. 4.6. This is because of the weak dominance of the magnetic force over the viscous force acting on nanoparticles during the OFF cycle.

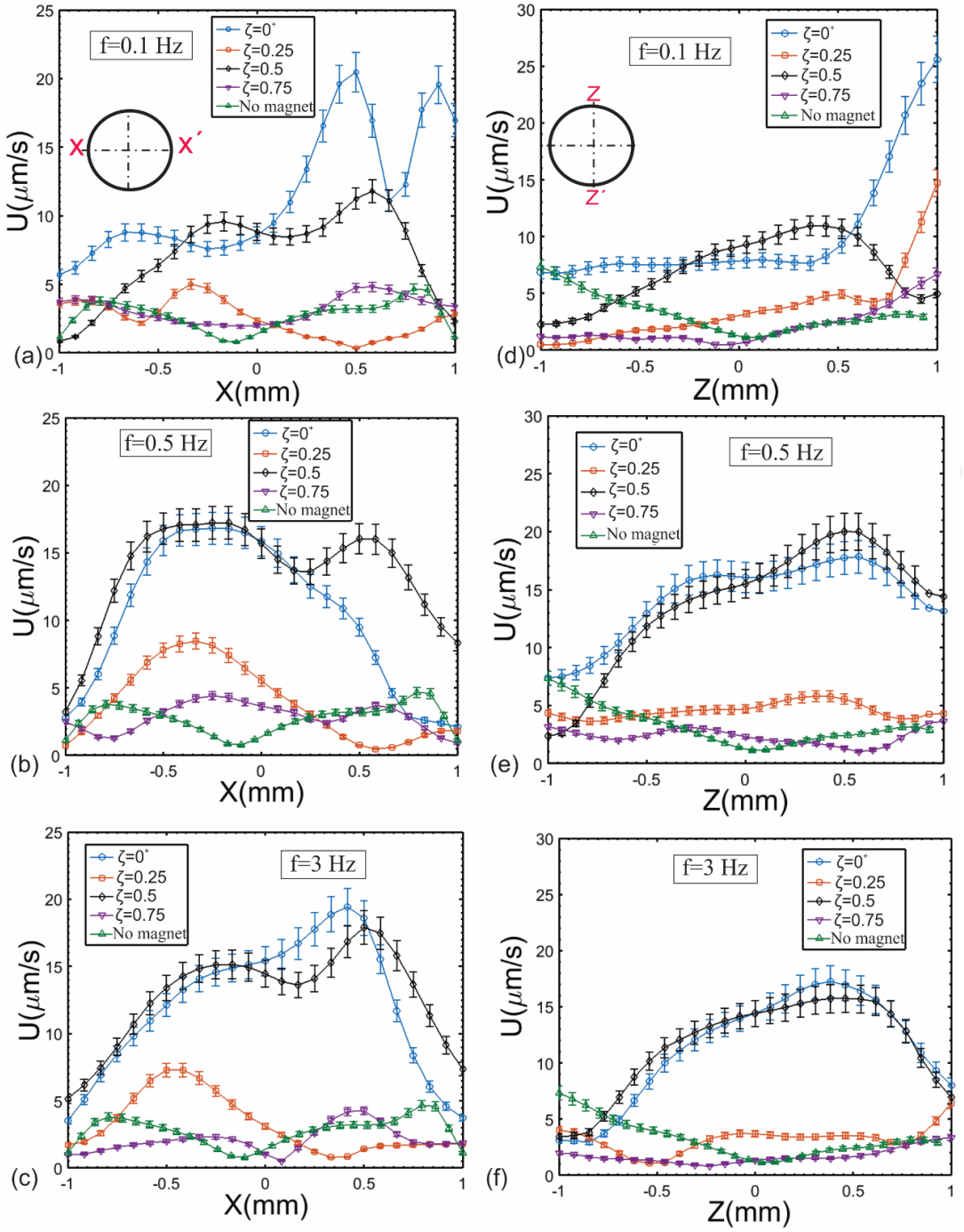

Fig. 4.8 Variation of the total velocity (U) along the diameters $X - X'$ and $Z - Z'$ of the ferrofluid droplet at different time instants in the presence of a magnetic field. $\zeta = t/T_M$, where T_M is the time of operation of the electromagnet.

The black arrow in each velocity plot clearly indicates that two opposite bulk motion exist across the line of symmetry of the droplet during the ON and OFF cycle, as shown in Fig. 4.6. In order to quantify the strength of the circulation of the flow inside the droplet, we calculated the vorticity of the velocity field (ω_y) and is shown in Fig. 4.7. The corresponding streamlines are also superimposed on the vorticity plot, as shown in Fig. 4.7. It can be clearly observed that for all the cases of actuation frequencies, at $\zeta = 0^+$, two opposite directed vorticity were generated inside the droplet due to the motion of bulk flow towards the electromagnet during the ON cycle. From $\zeta = 0^+ - \zeta = 0.25$, vorticity was observed to be affected by the continuous aggregation of nanoparticles at the contact line, as evident from the streamlines, as shown in Fig. 4.7. Similarly, during the OFF cycle, the dispersion of nanoparticles resulted in two opposite directed vorticity inside the droplet as compared to the ON cycle, as shown in Fig. 4.7.

Figure 4.8 shows the variation of the total velocity (U) along the diameter $X - X'$ and $Z - Z'$ of the droplet at different time instants for each case of actuation frequency, respectively. In order to compare the effect of magnetic field, the total velocity in the absence of magnetic field $(\bar{B} = 0)$ is also superimposed in each plot, as shown in Fig. 4.8. It can be clearly observed that the magnitude of total velocity U along the diameters $X - X'$ and $Z - Z'$ increased in the presence of magnetic field for a complete cycle $(\zeta = 0^+, 0.25, 0.5, 0.75)$ as compared to the case of no magnetic field. This is because of the migration and dispersion of nanoparticles in the presence of a magnetic field, which resulted in a strong bulk motion inside the droplet as compared to negligible bulk motion in case of no magnetic field. For each case of actuation frequency, the velocity magnitude was found to decrease from time instant $\zeta = 0^+$ to $\zeta = 0.25$ because of the continuous aggregation of nanoparticles at the contact line, as discussed in the previous section. During the OFF cycle $(\zeta = 0.5 - 0.75)$, the velocity magnitude was found to decrease for all the cases of actuation frequencies, as shown in Fig. 4.8. This is because of the dispersion of nanoparticles from the aggregated nanoparticles at the contact line resulting from the strong viscous force acting on nanoparticles during the OFF cycle. An increase in velocity magnitude was observed with an increase in actuation frequency, as shown in Fig. 4.8. This is because, with an increase in actuation frequency, the magnetic perturbation time scale was found to be lower as compared to viscous time scale. Lower magnetic perturbation time scale with increasing actuation frequency resulted in partial retention of bulk flow from the previous ON cycle of the magnetic field with no dispersion of nanoparticles at the contact line.

4.4 SUMMARY

The internal hydrodynamics of ferrofluid droplets plays an important role in the magnetic field-assisted evaporation/spreading/mixing of ferrofluid droplets. Though the opaqueness of ferrofluid limits the use of various velocity measurement techniques, the present study reports the possibility of using the μ-PIV technique to measure the velocity field of ferrofluid flow in the presence of a magnetic field. The present study reports the internal hydrodynamics of a sessile ferrofluid droplet in the presence of a time-dependent magnetic field of different actuation frequencies. The application of a magnetic field leads to the migration of nanoparticles in the direction of the magnetic field, which in turn results in internal convection or bulk flow inside the ferrofluid droplet. The magnitude of internal convection is found to be a function of strength and frequency of the applied magnetic field. A critical frequency of the applied magnetic field is observed above which negligible dispersion of nanoparticles is observed at the contact line of the droplet during the OFF cycle of the magnetic field. Negligible dispersion of nanoparticles at critical frequency results in stagnant layers of nanoparticles near the contact line, which can be explored in the future for the study of separation of cells or proteins using various markers/antibodies attached magnetic nanoparticles. As the strength of the circulation of internal convection of the droplet is observed to be higher in the presence of a magnetic field, such flow circulation can be effective for magnetically assisted mixing of reagents or fluids.

Chapter 5

EFFECT OF TIME-VARYING MAGNETIC FIELD ON THE MIXING CHARACTERISTICS OF A SESSILE FERROFLUID DROPLET WITH A NON-MAGNETIC DROPLET

As seen in the previous chapters that substantial agitations can be developed in the ferrofluid droplet flow field on perturbation by a time-dependent magnetic field. In this chapter, the implication of the enhanced convection on the ferrofluid droplet's mixing characteristics with another non-magnetic droplet is explored. Bright field visualization and μ-PIV measurement technique are employed for qualitative and quantitative understanding of the internal hydrodynamics of the droplet. The μ-LIF measurement technique is used for the quantification of the mixing index. The role of the various timescale on the overall mixing time between the droplets is highlighted. An important phenomenon of flow instability arising due to the susceptibility mismatch between the two fluids are outlined as well.

5.1 INTRODUCTION

In the previous chapter, we have explored the several facets of the internal hydrodynamics of a sessile ferrofluid droplet under the modulation of a magnetic field. In this study, we investigate the role of internal convections on the mixing characteristic of the droplet. Augmentation of the mixing phenomena under the influence of a magnetic field has been explored in the past (Roy et al. 2009; Zhu and Nguyen 2012; Hejazian et al. 2016). In this chapter, a new method of generating strong convection inside the ferrofluid droplet under the influence of a time-periodic magnetic field is investigated. The ferrofluid droplet (base droplet) is placed between two alternatively acting electromagnets. We show that the transiences in nanoparticles induce a magneto convective flow, which, in turn, promotes the mixing of the base droplet with the non-magnetic sister droplet being injected from the top. The intermittent motion of the magnetic nanoparticles under the influence of the time-dependent magnetic actuation triggers the interfacial instabilities to a significant extent. This phenomenon eventually brings about sufficient agitation in the droplet's bulk liquid, leading to enhanced mixing. The concentration field in the droplet domain under the magnetic field's influence was numerically simulated for the qualitative understanding of the mixing

characteristics. In what follows, this chapter is divided into three sections. In the first section, we explore the ferrofluid droplet's internal convective characteristics in the presence of a magnetic field with the help of bright field visualization. In the intermediate section, following the μPIV measurement technique, we explore the internal hydrodynamics of the bulk liquid inside the droplet in the presence of a magnetic field. In the final section of this chapter, we explore the implication of this augmented advective force on the ferrofluid droplet mixing with another non-magnetic droplet.

5.2 MATERIALS AND METHODS

5.2.1 Substrate preparation and fluid characterization

The preparation of the PDMS substrate is appropriately discussed in section 2.6 of chapter 2. The ferrofluid droplet forms a contact angle of $\theta_{ferrofluid}$~65° on the PDMS substrate. The magnetic nanoparticles are coated with surfactant (Lauric acid) essentially to prevent any interparticle agglomeration in the ferrofluid solution. Note that the coated surfactant layer lowers the contact angle of the ferrofluid solution to the aforementioned value. The preparation and characterization of the ferrofluid solution are elaborately discussed in section 2.7 of chapter 2.

5.2.2 Magnetic forcing actuation setup

The fabrication of electromagnet and its time-dependent actuation is discussed appropriately in section 2.5 of chapter 2. We place the electromagnets at a distance of 0.2 mm from the periphery of the droplet. Note that the time-dependent operation ensures alternate actuation of the electromagnets at a predefined specific instant of time. In the present study, we keep the magnetic field flux density constant at $\bar{B} = 400\ G$, while the actuation frequency varies from $f = 0.3\ Hz$ to $5\ Hz$. In the appendix section, we have provided the distribution of this magnetic field generated by the electromagnet inside the droplet domain (refer Appendix B.1).

5.2.3 Experimental setup and the working principle

We show, in Fig. 5.1(a), the complete methodology of the experiments conducted in this study through a series of schematic depictions. We now briefly discuss the experimental procedure for the sake of completeness and ease in understanding. A ferrofluid droplet of volume 1 μl is placed on the treated PDMS substrate using a digital microdroplet dispenser (Make: Tarsons). We perturb the ferrofluid droplet by a time-dependent magnetic actuation, originating from two axially aligned electromagnets (cf. Fig. 5.1(a)). The controlled magnetic

perturbations generate internal convections inside the droplet. The imposed magnetic actuation strength for about 40 s leads to the formation of a chain-like structure of nanoparticles inside the ferrofluid droplet. Following this event of chain formation, a water droplet containing fluorescent dye (0.05g of Rhodamine 6G in 20 ml of De-Ionized water) of the equal volume is injected on to the ferrofluid droplet with the help of a microdroplet dispenser. We use a hall probe digital gaussmeter (Make SES instruments) to measure the strength of the applied magnetic field. Note that we perform all experiments for base magnetic field strength, $\bar{B} = 400\ G$. Also, care has been taken during experiments to isolate the droplet from the convection currents of the surrounding air such that no shear-induced mixing takes place.

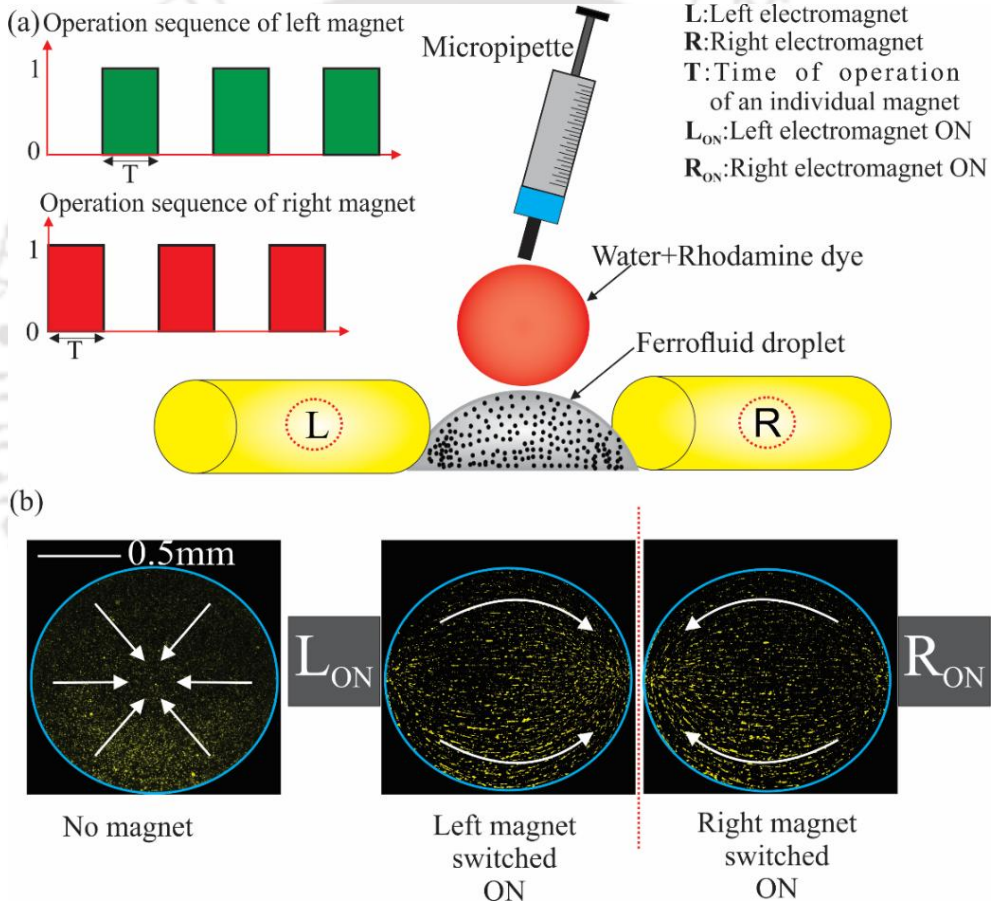

Fig. 5.1 (a) Schematic representation of the working mechanism of the proposed microfluidic platform for rapid and efficient droplet mixing. A fluorescent water droplet is injected from top to a sessile ferrofluid droplet under the actuation of a time-dependent magnetic field. The sequence of operation of the electromagnet is shown in the top left corner of the figure. When the left magnet is in ON-state, the right magnet remains in OFF-state and vice versa. All the involved symbols were defined aptly on the top right-hand side of the figure. (b) Plots show the motion of the fluorescent seeded particles in the presence and absence of the magnetic field. The white-colored arrow shows the direction of the bulk fluid flow inside the droplet.

Figure 5.2(a) shows the schematic of the experimental setup. As already discussed, the present experimental study is divided into three primary parts: the bright field

visualization, the μPIV (micro-particle image velocimetry) analysis, and the μLIF (micro laser-induced fluorescence) investigation. Also, we numerically simulate the mixing process in the present problem, primarily to compare the insights gained from the experimental observations. It is worth mentioning here that the intricate details captured from the simulations co-operate in explaining the experimental results for a better understanding of the flow physics of our interest. In the bright-field visualization, white light from the mercury lamp illuminates the droplet flow field. We observe the transmitted white light from the bottom of the substrate with the help of a 10X (magnification) objective lens having a numerical aperture (NA) of 0.24. In the bright-field visualization, we perceive the motion of the magnetic nanoparticles (MNPs) in the presence of a time-dependent magnetic field. We use an objective lens of higher magnification of 20X to capture the chain-like cluster[1] of the magnetic nanoparticles.

We perform μPIV investigation for the quantification of the internal flow hydrodynamics of the droplet. The details of the μPIV analysis are elaborately explained in chapter 2 (section 2.4) and are not mentioned here for brevity. We appeal to the μLIF investigation for the quantification of the underlying mixing phenomena between the base (ferrofluid) and sister (water) droplets. The experimental setup is similar to the μPIV configuration. For the present task (μLIF investigation), the ferrofluid droplet domain is illuminated by the fluorescent light, and the water droplet (containing fluorescent dye) is subsequently injected from the top with the help of a microdroplet dispenser (Make: Tarsons). Since the beginning of the water droplet injection, we start recording the distribution of the water droplet inside the ferrofluid droplet domain. The recorded images are subsequently converted to the grayscale format. For the elimination of noise from the captured images, we subtract the intensity histogram of the base reference image from all the subsequent recorded images for a particular experiment. Following this, we calculate the standard deviation of the pixel intensity in the droplet region, as given by,

$$C' = 1 - \sqrt{(1/N)\sum_{1}^{N}[(P-\bar{P})^2/\bar{P}^2]} \tag{5.1}$$

[1] The formation of chain-like cluster is an important event associated with the internal hydrodynamics of the ferrofluid drop. This feature has been elaborated in the results and discussion part of this article in greater detail.

Where P, is the intensity which varies from 0 to 256, while the mean pixel value ($\bar{P}$) is given by:

$$\bar{P} = (1/N)\sum_{1}^{N} P \tag{5.2}$$

N represents the number of pixels. Initially, when the droplet is in the unmixed state, $C' = C_0$ and at the final stage of mixing, $C' = C_\infty$. Thus, the mixing index is normalized as

$$\bar{C} = \frac{C' - C_0}{C_\infty - C_0}; 1(= \text{Mixed state}) < \bar{C} > 0(= \text{Unmixed state}) \tag{5.3}$$

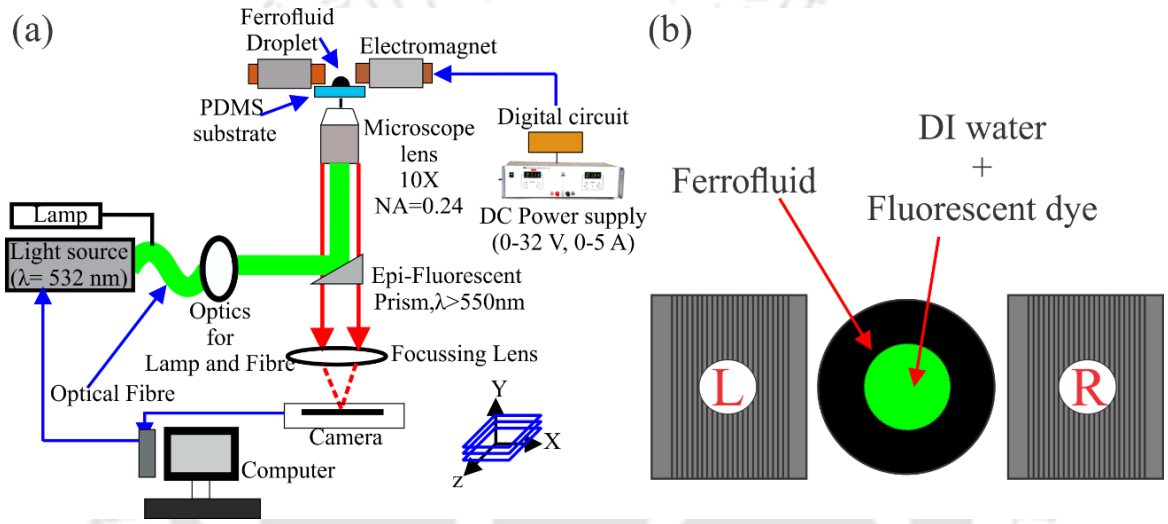

Fig. 5.2 (a) Schematic of the experimental set up along with its components. The experimental setup is used to conduct the bright field visualization, micro-particle image velocimetry (μPIV) analysis, and micro-laser induced fluorescence (μLIF) investigation in the droplet domain. All the components are aptly described in the text. (b) Schematic of the simulated two-dimensional computational domain. L and R indicate the left and right magnet, respectively. (Schematic is drawn not to scale)

During experiments, we ensure to maintain the temperature and the humidity inside the laboratory at $25 \pm 0.5°C$ and $67 \pm 1\%$, respectively. The calculated value of the Bond number ($Bo = \rho g D_h^2/\gamma$) is found to be less than one. However, the magnetic bond number is calculated as $Bo_m = \mu_0 H^2 R/\gamma$ where $\mu_0, H, R,$ and γ represents the magnetic permeability of vacuum, magnetic field intensity, radius of the droplet, and the interfacial tension, respectively. For the present case $Bo_m > 1$, which signifies the dominance of the magnetic force on the droplet domain. For ensuring repeatability, we perform each experiment four times using the same sample. It is worth mentioning here that the maximum uncertainties involved in each run do not exceed 8%.

5.2.4 Numerical method

We also make an effort to simulate the droplet flow field numerically, essentially to understand the intricate dynamics of the convective-diffusive mass transfer between the two droplets. We perform in this study two-dimensional (2D) numerical simulations using COMSOL Multiphysics®. We refer to Fig. 5.2(b), showing the schematic of the computational domain consisting of the sessile droplet (the base droplet), the sister droplet, and the two time-dependent magnets. The continuity and the Navier-Stokes equations for the unsteady, viscous and incompressible fluid flows are given by:

$$\frac{\partial \rho}{\partial t} + \nabla.(\rho \bar{u}) = 0 \tag{5.4}$$

$$\frac{\partial (\rho \bar{u})}{\partial t} + (\bar{u}.\nabla)\bar{u} = -\nabla P + \nabla\{\eta(\nabla \bar{u} + \nabla \bar{u}^T)\} + \bar{F} \tag{5.5}$$

where ρ is the density(kg/m^3) of the fluid, $\bar{u}$ is the velocity field(m/s), η is the viscosity of the fluid $(Pa.s)$, and $\bar{F}$ is the volume force in (N/m^3). We calculate the magnetic field acting on the droplet flow domain by solving the Maxwell equations as given by (Griffiths and Inglefield 2005):

$$\nabla \cdot \bar{B} = 0 \tag{5.6}$$

$$\nabla \times \bar{H} = 0 \tag{5.7}$$

where $\bar{B}$ is the magnetic flux density and $\bar{H}$ is the intensity of the magnetic field. The magnetic flux density $(\bar{B})$ is given by (Griffiths and Inglefield 2005):

$$\bar{B} = \mu_0(\bar{H} + \bar{M}) \tag{5.8}$$

μ_0 is the permeability of vacuum, $\bar{M}$ is the magnetization of the flow domain. The magnetization $(\bar{M})$ is described as (Griffiths and Inglefield 2005):

$$\bar{M} = \chi \bar{H} \tag{5.9}$$

where χ is the magnetic susceptibility of the fluid. Note that $\bar{F}$ in (5.5) is the force that comprises of the gravity force $(\bar{F}_g)$, interfacial tension $(\bar{F}_s)$, and the magnetic force $(\bar{F}_m)$. The gravity force is neglected since the Bond number is less than one (< 1). The interfacial tension can also be ignored since the fluids are miscible. The magnetic force $(\bar{F}_m)$ is calculated from (Strek 2008):

$$\bar{F}_m = (\bar{M} \cdot \nabla)\bar{B} \tag{5.10}$$

Using $\bar{B} = \nabla \times \bar{A}$ in (5.10), the component of the magnetic force ($\bar{F}_m$) in X and Y direction respectively, can be written as (Nouri et al. 2017),

$$F_{m,x} = \frac{C\chi}{\mu_0 \mu_r^2}\left[\frac{\partial A_z}{\partial y}\cdot\frac{\partial^2 A_z}{\partial x \partial y} + \frac{\partial A_z}{\partial x}\cdot\frac{\partial^2 A_z}{\partial x^2}\right] \tag{5.11a}$$

$$F_{m,y} = \frac{C\chi}{\mu_0 \mu_r^2}\left[\frac{\partial A_z}{\partial x}\cdot\frac{\partial^2 A_z}{\partial x \partial y} + \frac{\partial A_z}{\partial y}\cdot\frac{\partial^2 A_z}{\partial y^2}\right] \tag{5.11b}$$

where $\bar{A}$ is the magnetic vector potential (Wb/m), μ_r is the relative permeability of the magnet. The advection-diffusion equation governing the mass transfer phenomena in the droplet domain (modelling framework) is given by,

$$\frac{\partial C}{\partial t} + (\bar{u}.\nabla C) = \nabla \cdot \{D \nabla C\} \tag{5.12}$$

where C is the concentration of the fluid, and D is the diffusion coefficient of the fluid (m^2 / s). The ferrofluid is allotted a scaler concentration value of $C = 1$, while the fluorescent DI-water is allotted a scaler concentration of $C = 0$. The advective-diffusion process will alter the density and viscosity of the mixture in a time-dependent magneto convective flow. Therefore, the density and viscosity of the fluid need to be represented as a function of the concentration flow field (Wen et al. 2011),

$$\rho_{mix} = C\rho_f + (1 - C)\rho_w \tag{5.13}$$

$$\eta_{mix} = \eta_f e^{R(1-C)} \tag{5.14}$$

$$\text{Where, } R = ln(\eta_w/\eta_f) \tag{5.15}$$

where the subscripts mix, f, and w stand for mixture, ferrofluid, and water, respectively. Similarly the effective density (ρ_f) and viscosity (η_f) of ferrofluid can be calculated as (Brinkman 1952),

$$\rho_f = \varphi\rho_{MNP} + (1 - \varphi)\rho_w \tag{5.16}$$

$$\eta_f = \eta_w\left(\frac{1}{(1-\varphi)^{2.5}}\right) \tag{5.17}$$

φ is the volume fraction of magnetic nanoparticles (MNPs) in the ferrofluid solution. Note that in the present work ferrofluid is treated as pure fluid, while its density and viscosity as calculated from eq. (5.16)-(5.17) are used in the numerical computation. The numerical mixing index $(\bar{C})$ is calculated using the following equation (Wang *et al.* 2008; Wen *et al.* 2011),

$$\bar{C} = 1 - \frac{\int_0^R \int_0^{2\pi} |C - C_{n\infty}| r dr d\theta}{\int_0^R \int_0^{2\pi} |C_{n0} - C_{n\infty}| r dr d\theta} \tag{5.18}$$

where C_{n0} and $C_{n\infty}$ are the computed concentration of the droplet domain at the initial and final temporal instances. As such, the initial unmixed state has $\bar{C} = 0$, while the final mixed state has $\bar{C} = 1$

In the numerical simulations, the boundary and the initial conditions are as follows: For the momentum equation, no-slip condition is maintained at the outer boundary of the droplet. For the mass transport equation, no flux condition is applied at the outer boundary droplet; continuity in flux at the interface of the two droplets. As already mentioned before, the ferrofluid is allotted a scaler concentration value of $C = 1$, while the fluorescent DI-water is allotted a scaler concentration of $C = 0$. For the magnetic field simulations, the magnetic insulation boundary condition $(n \times \bar{A} = 0)$ is applied to the surrounding air. To solve the complex two-way coupled non-linear governing equations as mentioned by eq. (5.4)-(5.7) and eq. (5.12), we have used the computational framework of COMSOL Multiphyscis®. We employ the in-built laminar flow, transport of diluted species, and the magnetic field interface to solve the coupled advection-diffusion phenomena. Also, Newton iterations are executed, and the MUMPS solver has been implemented for the linear algebraic system deriving from the finite-element formulation. The second-order backward differentiation formula has been used for temporal discretization. The time step strategy is such that each magnetic cycle is divided into 20 steps to capture all the intricate physics. Also, it is ensured that simulations start at a very small initial time step of $10^{-8}s$. A fixed tolerance value of 10^{-6} is ensured for all the simulations.

5.3 RESULTS AND DISCUSSION

The ferrofluid droplet flow domain consists of a magnetic part and a non-magnetic part. The magnetic nanoparticles (MNPs) constitute the magnetic part, while the non-magnetic part comprises of the bulk carrier liquid. As already mentioned, we explore the motion of the MNPs by bright-field investigations, while the μ-PIV measurement technique quantifies the bulk flow motion. The movement of the nanoparticles under the influence of the applied magnetic field alters the flow dynamics inside the ferrofluid droplet domain, which in turn, changes the concentration field and results in better mixing. We also numerically simulate the magneto convective flow and its effect on the concentration field. Next, we will discuss the

underlying issues of the flow dynamics in the presence of a magnetic field and subsequent mixing in the forthcoming sections.

5.3.1 Droplet Internal hydrodynamics

A. Bright field visualization

In Fig. 5.3(a)-(b), we show the movement of the MNPs when a time-dependent magnetic field of frequency $f = 0.3$ Hz perturb the ferrofluid droplet domain. A magnetic field frequency of 0.3 Hz implies that the time period of the particular magnetic forcing cycle is 3.333.. s. Note that out of the total cycle time ($\sim$3.333 s); the right magnet remains in ON state for 1.6666.. s, while the left magnet is in ON state for another 1.6666.. s. This process is repeated in the time-periodic forcing environment. Since both the electromagnets are aligned along the diametrical direction of the droplet, we show, in Fig. 5.3(a)-(b), the snapshots for the cases when the right magnet is active. Needless to say, the MNPs motion will exhibit similar qualitative kinetics even when the left magnet is turned on to the active state, albeit the direction of the MNPs motion would change. Figure 5.3(a) demonstrates the bright field visualization of the motion of the MNPs at various temporal instants. Note that zero '0' ms denotes the state when the right magnet is switched ON. The MNPs, on the realization of the applied magnetic force, start migrating towards the active magnet (Right magnet). Precise observation of Fig. 5.3(a) shows that the MNPs moves in the droplet flow field following the formation of the cluster having a head and a long tail. The head of the cluster moves towards the active magnet (right magnet) upon piercing through the carrier liquid. This typical piercing action of the cluster (of MNPs), in turn, creates agitations inside the bulk liquid of the ferrofluid droplet. The course of this agitation endorses a motion in the droplet domain. Note that the induced motion due to this agitation is in the opposite direction of the moving MNPs motion (as shown by green arrows in Fig. 5.3(a)). The cluster (of MNPs) on reaching the vicinity of the active magnets strikes the triple contact line. Following this, it undergoes deformation, and in-process rearranges itself according to the prevailing magnetic force environment. Subsequently, the MNPs agglomerates and realigns in a chain-like formation. It is worth mentioning here that this chain-like cluster formation is primarily due to the interparticle dipole-dipole interaction existing between the MNPs in the presence of the magnetic field, as given by $I_m(ij) = -\left[3\frac{(m_i \cdot r_{ij})(m_j \cdot r_{ij})}{r_{ij}^5} - \frac{m_i m_j}{r_{ij}^3}\right]$, where $r_{ij} = r_i - r_j$ is the distance between the i_{th} and j_{th} nanoparticles having magnetic moments m_i and m_j respectively (Mendelev and Ivanov 2004). This chain-like cluster of the MNPs breaks down

as the inactive magnet (the left magnet for the present configuration) returns to its active phase, and the motion of the deagglomerated MNPs continues in a similar manner towards the active magnet (Left at the prevailing situation). This typical fashion of movement of the MNPs inside the droplet domain, i.e., with head and tail, is encountered only at low frequency. At higher frequencies, such kind of motion of the MNPs is not observed. We will discuss this non-intuitive behavior in the latter part of this section in greater detail.

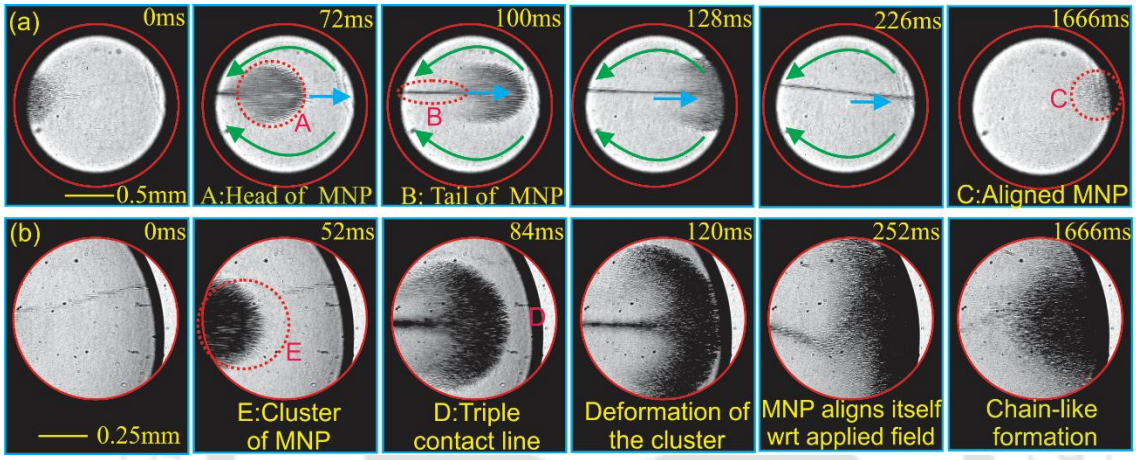

Fig. 5.3 (a) Snapshots depict the motion of the magnetic nanoparticles (MNPs) inside the ferrofluid droplet domain at various temporal instances when perturbed by the time-dependent magnetic field frequency (f) of 0.3 Hz. The blue-colored arrows indicate the direction of the MNPs. The green-colored arrows show the direction of the motion of the bulk carrier fluid. The images are recorded at a microscope magnification of 10X. (b) Snapshots illustrate the spatio-temporal motion of the migrating MNPs near the magnetically active triple contact line. The images are recorded at a higher microscope magnification of 20X.

To further understand the arrangement of the magnetic nanoparticles near the triple contact line area of the active magnet, we make an effort in Fig. 5.3(b) to demonstrate the flow field captured with a higher magnification of 20X. A closer observation of Fig. 5.3(b) shows that the head of the clustered MNPs undergoes deformation on striking the active triple contact line (at around 120ms). As a result of this deformation, we observe the re-alignment of the MNPs in tune with the applied magnetic force field, leading to the development of a chain-like cluster. Note that the individual MNP acts as a dipole in the presence of the applied magnetic field, which, in effect, leads to the development of the chain-like cluster formation.

In Fig. 5.4, we show the spatio-temporal variation of the MNPs inside the droplet domain when perturbed by a time-dependent magnetic field of four different frequencies $f = 0.3\ Hz,\ 1\ Hz,\ 3\ Hz,\ and\ 5\ Hz$ respectively. On actuation of the electromagnet, the MNPs migrate towards the active electromagnet following the typical cluster-like formation, as already explained in the preceding discussions, i.e., a head moves in the forward direction

followed by a long tail. However, this distinctive motion (of MNPs) in a clustered fashion is limited to the lower frequencies, i.e., for $f = 0.3\ Hz$ and $1\ Hz$. At a higher frequency of the magnetic field $f = 3\ Hz$ and $5\ Hz$, the presence of neither the head nor the tail (of the MNP's) could be traced in the domain, as can be seen from Fig. 5.4. In addition to that, a distinct chain-like cluster formation is also not observed at a relatively higher frequency (precisely $f = 5\ Hz$ case). We would like to discuss another interesting observation on the non-dimensional time (ζ) taken by the MNPs cluster to reach the triple contact line nearer the active electromagnet as follows. The non-dimensional time (ζ) is defined as the ratio of instantaneous time to the time period for which an individual magnet remains at ON state (T_M), specifically, $\zeta = t/T_M$. At low frequency, the MNPs could reciprocate between the two magnetically active zones, as can be seen from Fig. 5.4. However, at higher frequencies, the MNPs are unable to reach the magnetically active zones, as observed in Fig. 5.4. In order to figure out the underlying physical reasoning behind this observation, we look at the effects of the advective time scale of the MNPs and the magnetic perturbation time scale of the electromagnet. The advective time scale ($t_u = D_h\ /\ U_{MNP}$) refers to the time taken by the MNPs to travel the characteristics length, i.e., the droplet diameter, at a particular strength of the actuation force. While the perturbation time scale ($t_m = 1/2f$) implies the time over which an individual magnet remains in the ON stage. For the calculation of the advective time scale, we tracked the motion of the cluster of MNPs in presence of the magnetic field. The images were recorded at 300 frames per second, and the nanoparticle cluster was tracked with the help of ImageJ plugin Trackmate® (Schneider et al. 2012). Average of multiple readings ranging over numerous cycles of the applied time-dependent magnetic field was taken for calculation of velocity of the cluster (of MNPs). Following which the average velocity (U_{MNP}) of the magnetic nanoparticles was found to be around 11mm/s. Based on this average velocity, the advective time scale ($t_u = D_h\ /\ U_{MNP}$) of the MNPs is found to be around $0.13\ s$. On the other hand the magnetic perturbation time scale, $t_m = 1/2f$ becomes $1.667\ s$, $0.5\ s$, $0.1667\ s$, and $0.1\ s$ for $0.3\ Hz$, $1\ Hz$, $3\ Hz$, and $5\ Hz$ cases, respectively. It is because of this imbalance between the advective and magnetic perturbation time scale ($t_u < t_m$), at lower frequencies of the magnetic field, particularly for $0.3\ Hz$ and $1\ Hz$, the MNPs could reciprocate between the two magnetically active zones, as can be seen from Fig. 5.4, whereas for a relatively higher frequency, i.e., for $f = 5\ Hz$ case, the advective time scale of the MNPs is higher as compared to the magnetic perturbation time scale. As a consequence, the MNPs could not reciprocate between the two magnetically active zones.

However, at the magnetic field frequency of 3 Hz, the advective time scale is almost balanced by the perturbation time scale ($t_u \sim t_m$). Quite notably, at this frequency, the MNPs travel in the most optimal way. This particular optimal motion of the MNPs at the magnetic field frequency of 3 Hz has a huge implication in the internal convections of the bulk carrier fluid flow, as well as its significance on subsequent mixing. We will discuss this part in the forthcoming sections.

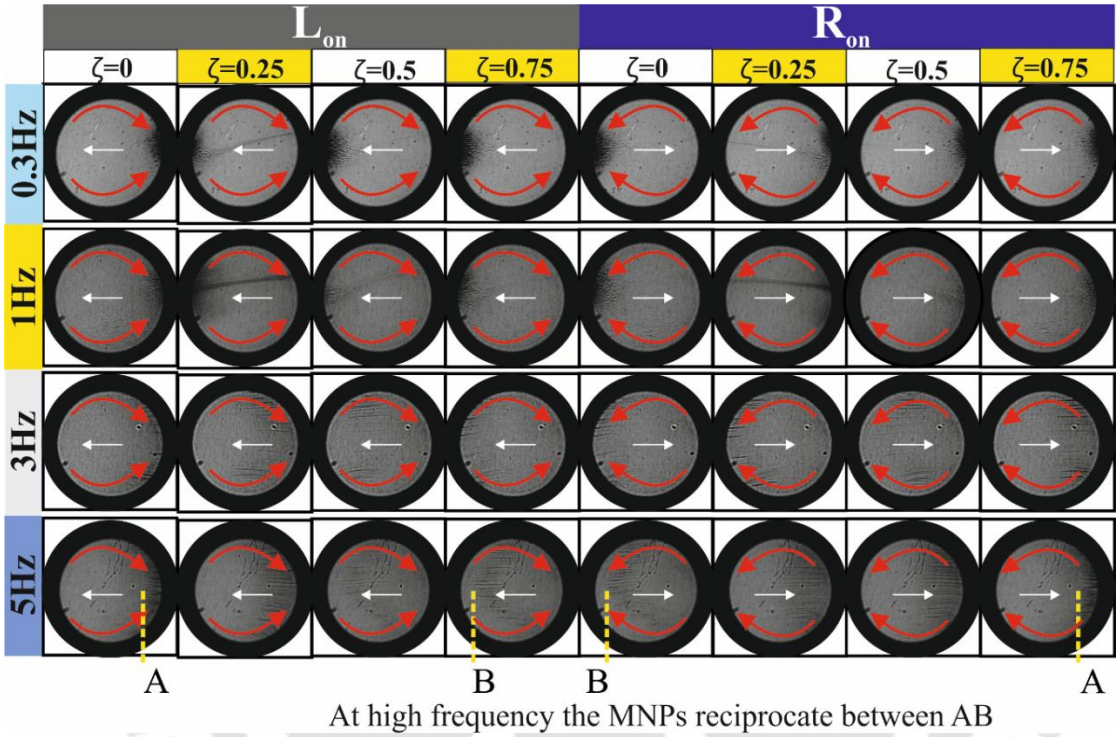

Fig. 5.4 Plot depicts the motion of the magnetic nanoparticles (MNPs) under the influence of magnetic field frequency of 0.3 Hz, 1 Hz, 3 Hz, and 5 Hz, respectively, for the various time instances of functioning of the electromagnet. The white colored arrows indicate the direction of the MNPs motion, and the red colored arrows show the direction of the bulk flow. "AB" denotes the position between which the MNPs reciprocate at $f = 5\ Hz$. $\zeta = t/T_M$, where t is the instantaneous time and T_M is the time of operation of an individual magnet.

B. µ-PIV investigation

We have seen in the previous section that the advective time scale (t_u) of the MNPs gets almost balanced by the perturbation time scale (t_m) of the electromagnet when the magnetic field frequency is maintained at $f = 3\ Hz$. This balance between the two active time scales (precisely t_u and t_m) signifies that the MNPs move between the two magnetically active regions in an optimum possible manner. It is worth mentioning here that the optimal movement of MNPs ensures substantial disturbances in the bulk fluid domain, as discussed next.

In Fig. 5.5, we show the variation of the velocity vectors of the bulk fluid flow inside the ferrofluid droplet domain obtained at different temporal instants of the magnetic actuation cycle with a frequency maintained at $f = 3\ Hz$. As we have already observed from the bright field visualization, on the actuation of the electromagnets, the motion of the MNPs leads to the development of oppositely directed motion of the bulk carrier fluid. This typical agitation of the bulk flow is the consequential effect of the piercing action of the MNPs on the carrier fluid, as discussed before. Due to this piercing action of the MNPs, a high-pressure zone is created ahead of the MNPs cluster, leading to the development of low pressure behind it.

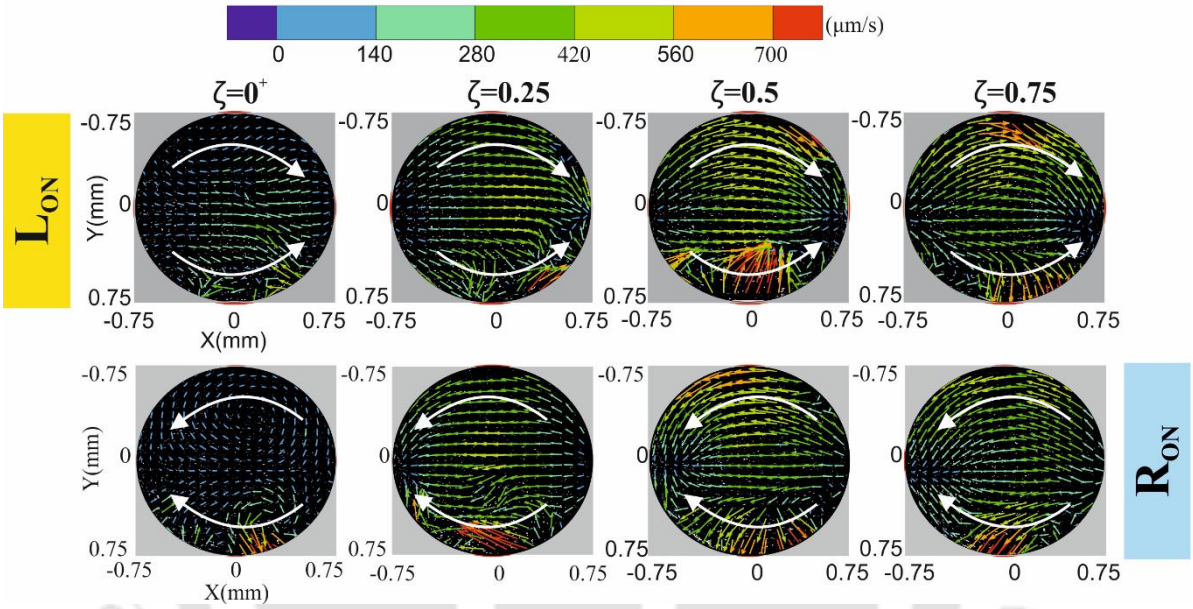

Fig. 5.5 Plot depicts the bulk flow motion inside the droplet at various time of operation of the magnetic field, when the frequency of the magnetic field is maintained at 3Hz. The total time of operation of an individual magnet is divided into four parts, with each individual time-steps denoting an increment of $T_M/4$, where 'T_M' represents the time of operation of an individual magnet, i.e., $T_M = 1/2f$. L_{ON} and R_{ON} signifies the state when the left electromagnet and the right electromagnet is active, respectively. The white colored arrows indicate the direction of the bulk liquid flow motion.

As a consequence of the spatial pressure gradient in the droplet domain, the bulk liquid moves from the high-pressure zone to the low-pressure zone. Following this phenomenon, we observe in Fig. 5.5 the bulk flow motion in the opposite direction of the MNPs motion. It is to be mentioned here that $\zeta = 0^+$ denotes the state when the magnet is just switched ON, while $\zeta = 0.25: 0.5: 0.75$ represents the subsequent intermediate stages. Note that at $\zeta = 0^+$, the MNPs realize the magnetic force and start rearranging themselves along the direction of the applied forcing environment. Primarily due to this rearrangement of the magnetic nanoparticles (MNPs), the low intensity of agitation is produced in the droplet flow domain at $\zeta = 0^+$. Consequently, we observe low magnitude velocity at this stage, as witnessed in Fig. 5.5. At $\zeta = 0.5$, a relatively higher velocity is observed in the droplet

domain. This is because the head of the moving MNPs on striking the triple contact line of the magnetically active zone generates a tremendous amount of agitation in the droplet fluid domain. Following this impact (of the MNPs with the triple contact line at the magnetically active region), the MNPs rearrange themselves according to the applied magnetic force field. As the MNPs start rearranging themselves, the viscous force of the bulk liquid subsequently dissipates the generated disturbances in the carrier fluid. Primarily due to this reason, we observe a spontaneous drop in the ferrofluid droplet flow velocity at $\zeta = 0.75$, as can be seen in Fig. 5.5. Similar characteristics can be observed even when the right magnet is turned into an 'On' state, barring the fact that the fluid motion is in the opposite direction to the scenarios pertinent to the left magnet case.

To obtain a clearer insight on this distinctive variation in the bulk flow velocity magnitude in the ferrofluid droplet domain, we depict Fig. 5.6(a). Note that Fig. 5.6(a) shows the variation of ϕ, which is given as:

$$\phi = \frac{U}{U_{0^+}} \tag{5.18}$$

While U refers to the strength of the velocity inside the droplet domain. U_{0^+} implies the strength of the flow-field at $t^* = 0^+$. The strength of the velocity (U) was calculated by the root mean square of all the velocity vectors along the X-Y plane, and given as:

$$U = \frac{1}{N \times M} \sum_{i=1,j=1}^{N,M} \sqrt{u(i,j)^2 + v(i,j)^2} \tag{5.19}$$

While N and M refer to the number of grid points in the X and Y directions, respectively. Note that $u(i,j)$ and $v(i,j)$ refers to the instantaneous X and Y directional velocities. From the observation made in the context of bright field investigation, we can recall that the movement of MNPs towards the magnet induces fluid motion inside the droplet. However, the MNPs on reaching further downstream impacts the triple contact line nearer the active magnet, which in turn creates a bulk disturbance in the carrier liquid. This disturbance, however, decays with time because of the effective viscosity of the carrier fluid. Keeping these inferences in mind, we would like to discuss the temporal variation of ϕ for the magnetic field frequencies of 0.3 Hz, 1 Hz, 3 Hz, and 5 Hz, respectively, as plotted in Fig. 5.6(a). For all the frequencies except for $f = 5\,Hz$, ϕ exhibits a positive (+ve) slope initially, and on reaching its peak value, it

encounters a negative (-ve) slope. When the magnetic field frequency is maintained at $f = 5\ Hz$, an almost constant slope is encountered. It is worth mentioning here that, although within the uncertainty region, a steady increase in ϕ for $f = 5\ Hz$ is distinctly visible from figure 7(a). Also, we report another important observation from Fig. 5.6(a) is that, for the $f = 3\ Hz$ case, the ϕ curve demonstrated maximum value.

The positive (+ve) slope signifies the rise in the bulk flow velocity, while a negative (–ve) slope of ϕ signifies a decrease in bulk flow velocity in the droplet domain. As discussed before, when the electromagnet is actuated, the MNPs moves towards the magnetically active zone. As a consequence of these disturbances, we observe a positive (+ve) slope of ϕ during initial temporal instants of the actuation cycle in Fig. 5.6(a). Next, when the moving MNPs impacts the triple contact line near the active magnet region, tremendous agitation is produced in the droplet flow field. At this point, we observe a peak velocity in the droplet domain, as witnessed in Fig. 5.6(a). Once the velocity reaches a peak value, the viscous effect of the fluid dissipates the agitated flow velocity to the surrounding fluid. Notably, as a consequence of this dissipating effect, following this peak value, we observe a negative (–ve) slope of ϕ in Fig. 5.6(a).

From the above discussion, it is clear that the viscous force acts as the suppressing agent for the agitation being developed in the flow field. Notably, we observed the presence of critical frequency $(f = 3\ Hz)$ at which the magnetic perturbation time scale almost balances the advective time scale of the MNPs. Following this balance between the dominant time scales, the suppression rate of the agitation intensity is largely reduced. As a result, we observe augmented flow velocity throughout the magnetic cycle for $f = 3\ Hz$ case, which is supported by $\phi > 1$ in Fig. 5.6(a). Conversely, for the cases of $f = 0.3\ Hz$ and $f = 1\ Hz$, the magnetic perturbation time scale becomes more significant than the advective time scale. Because of the dominating effect of the perturbation time scale, the disturbances initiated in the domain almost diminishes at the end of the magnetic field cycle. Consequently, we observe in Fig. 5.6(a) the value of ϕ lower than one $(\phi < 1)$ towards the end of the magnetic field cycle. When the magnetic field frequency (f) is maintained at 5Hz, the advective time scale (t_u) becomes higher than the perturbation time scale. Important to mention here that, because of this difference in involved time scales, the MNPs cannot fully impact both the triple contact line of the droplet at the magnetically active region. This temporal effect leads to a reduction in spatial dispersion of the MNPs in the flow domain. Thus, at this frequency,

the motion of the MNPs is highly localized, as seen in Fig. 5.4. Notably, as a consequence of this phenomenon, we encounter a constant slope for the 5 Hz case in Fig. 5.6(a).

In Fig. 5.6(b), we show the variation of ϕ_m in the droplet domain for a particular cycle of operation of the magnetic field. For the sake of completeness, we here define ϕ_m as given by,

$$\phi_m = \frac{\int_t^{t+T} \phi(t)dt}{T} \tag{5.20}$$

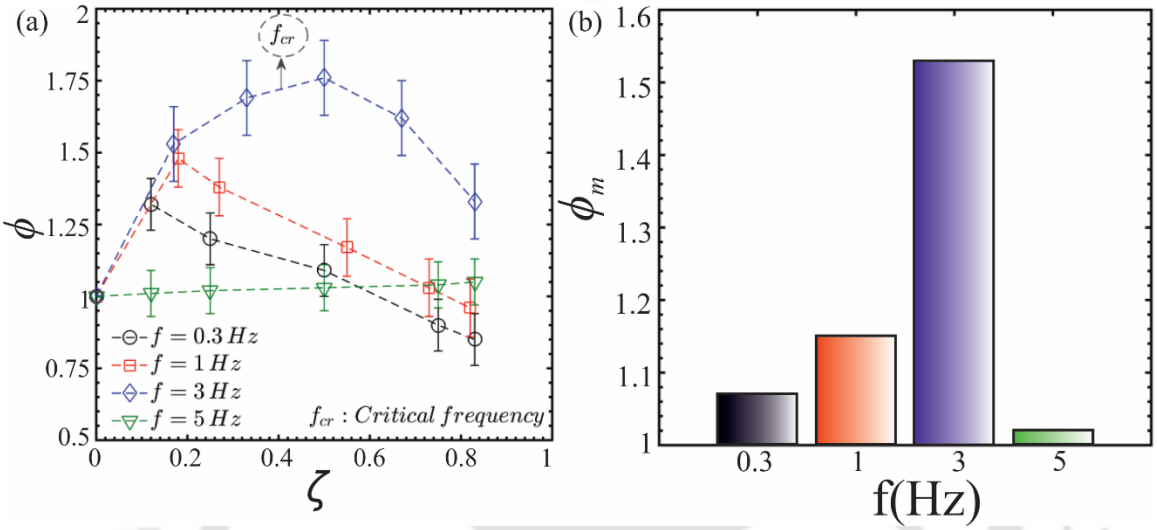

Fig. 5.6 (a) Plot illustrates the temporal variation of ϕ for various magnetic field frequencies. The black-colored arrow identifies the critical frequency of the applied magnetic field at which maximum disturbances are produced in the droplet domain. (b) The bar graph depicts the variation of ϕ_m for the various magnetic field frequencies.

As discussed before, when the magnetic field frequency is maintained at 3 Hz, the advective time scale almost balances the magnetic perturbation time scale. Thus, this frequency ($f = 3Hz$) serves as the critical frequency (f_{cr}) at which maximum agitation and minimum dissipation of the fluid velocity takes place in the droplet flow field. Primarily because of this reason, we encounter a high value of ϕ_m, as can be seen from Fig. 5.6(b). Whereas for lower frequencies (particularly, for $f = 0.3\,Hz$ and $f = 1\,Hz$), since the perturbation time scale is very large as compared to the advective time scale ($t_u < t_m$), the disturbances created in the flow domain by the moving MNPs get dissipated well in the field. As a result of this, we observe lower values of ϕ_m in Fig. 5.6(b). From the ongoing discussion, it may be inferred that, for frequencies higher than critical frequencies, i.e., $t_u > t_m$, the motion of MNPs are highly localized, thereby creating localized agitations in the bulk liquid domain. Due to this limited disturbance, a lower value of ϕ_m is encountered at this frequency (cf. Fig. 5.6(b)).

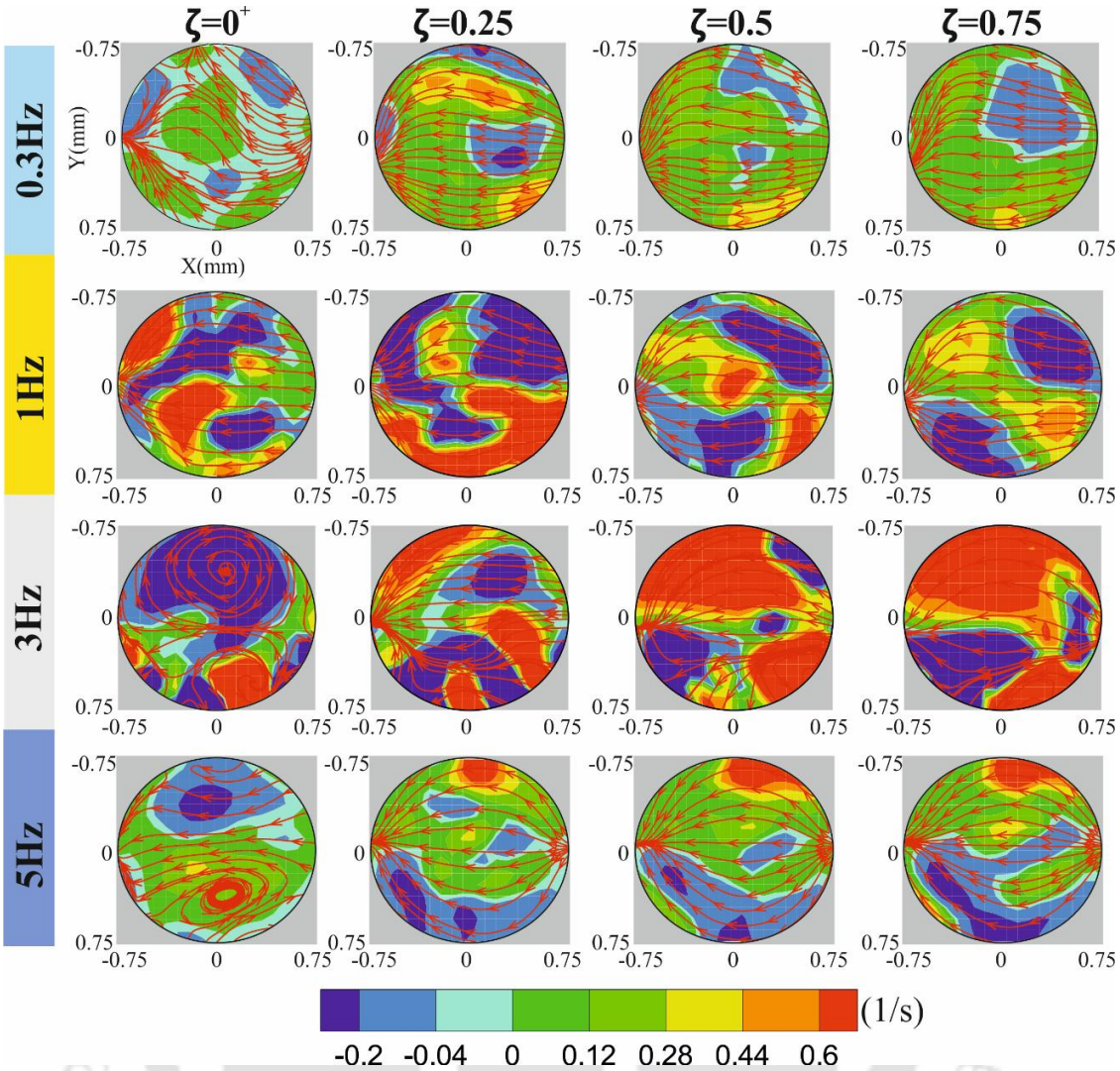

Fig. 5.7 Plot depicts the temporal variation of the vorticity contours for the various magnetic field frequency of 0.3 Hz, 1 Hz, 3 Hz, and 5 Hz, respectively. The red-colored arrows indicate the streamlines of the flow. The plot shows the vorticity flow field when the right magnet is in ON state.

In order to gain further insights into the underlying flow dynamics, we undertake an effort to predict the circulation produced inside the droplet flow field. In doing so, we calculate the vorticity (ω_z) of the velocity field as,

$$\omega_z = \nabla \times \bar{u} \tag{5.21}$$

In Fig. 5.7, we show the variation vorticity contours in the ferrofluid droplet flow field under the influence of various magnetic field frequencies. Two oppositely directed vortices are clearly observed for all the investigating cases. Quite intuitively, the magnitude of vorticity is maximum for the 3 Hz case in comparison to all other cases under consideration. This behavior is in agreement with our previously made observation on the development of maximum augmentation in velocity (cf. Fig. 5.6) in the droplet flow field at $f = 3\ Hz$.

5.3.2 Droplet mixing characteristics

A. Experimental insights

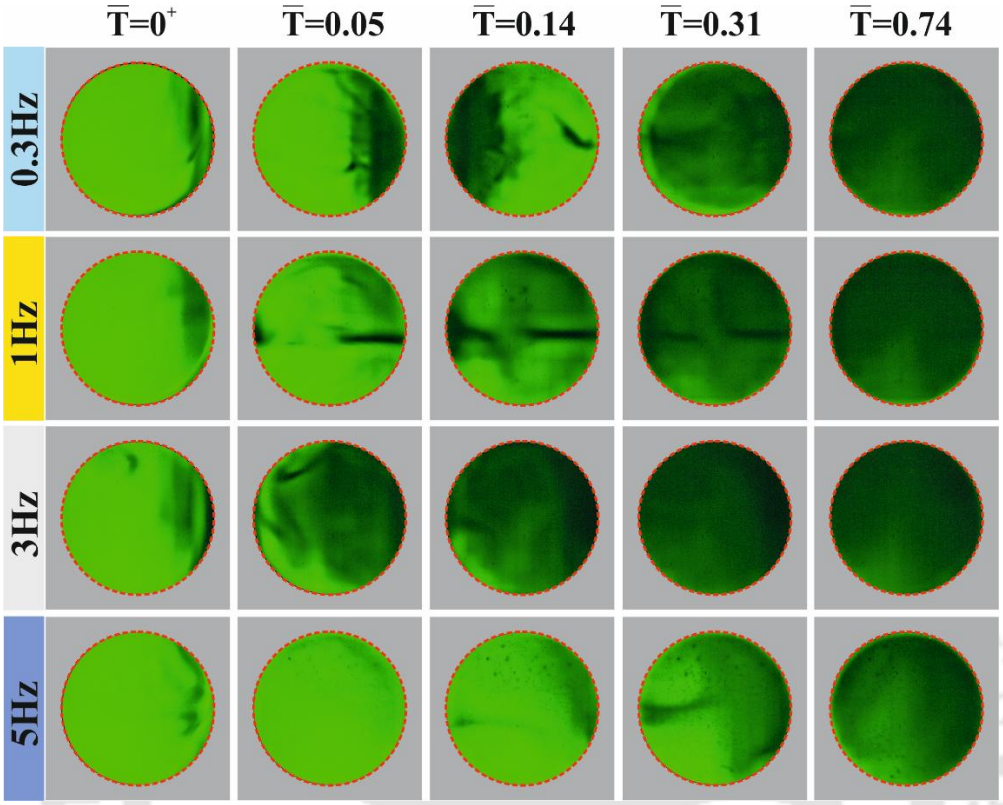

Fig. 5.8 Fluorescein distribution inside the droplet flow field at various time instances of the mixing processes for the magnetic field applied frequency of 0.3 Hz, 1 Hz, 3 Hz, and 5 Hz, respectively. $\bar{T}$ represents the non-dimensionalized mixing time and is given as $\bar{T} = t/T_0$ where, t is the instantaneous time and T_0 is the total time of mixing between the two droplets in the absence of a magnetic field.

From the discussion made in the preceding section, it is apparent that the manipulation of internal convections inside the ferrofluid droplet is possible by careful maneuvering of the MNPs movement. In this section, we explore the role of these convections on the underlying mass transfer between two droplets. The procedure adopted for the mixing process is already described in the materials and methods section.

In the absence of any external force, mixing between two droplets occurs solely due to molecular diffusion. However, the influence of a magnetic field in the paradigm of mixing dynamics at the microfluidic scale leads to a completely different scenario (Zhu and Nguyen 2012; Hejazian et al. 2016). Quite notably, the mixing dynamics gets further amplified in the presence of a time-dependent magnetic field. The amplification is primarily due to the substantial agitation produced in the droplet flow domain under the influence of a time-dependent magnetic field. The time-periodic magnetic actuation leads to interfacial instability, which, in turn, enhances subsequent mixing following an augmented agitation in

the droplet flow field. Note that the intensity of this agitation is directly related to the frequency of the applied magnetic field, attributed primarily to its considerable effect on the interfacial instability. Because of this frequency modulated agitation, the underlying mixing between two droplets enhances.

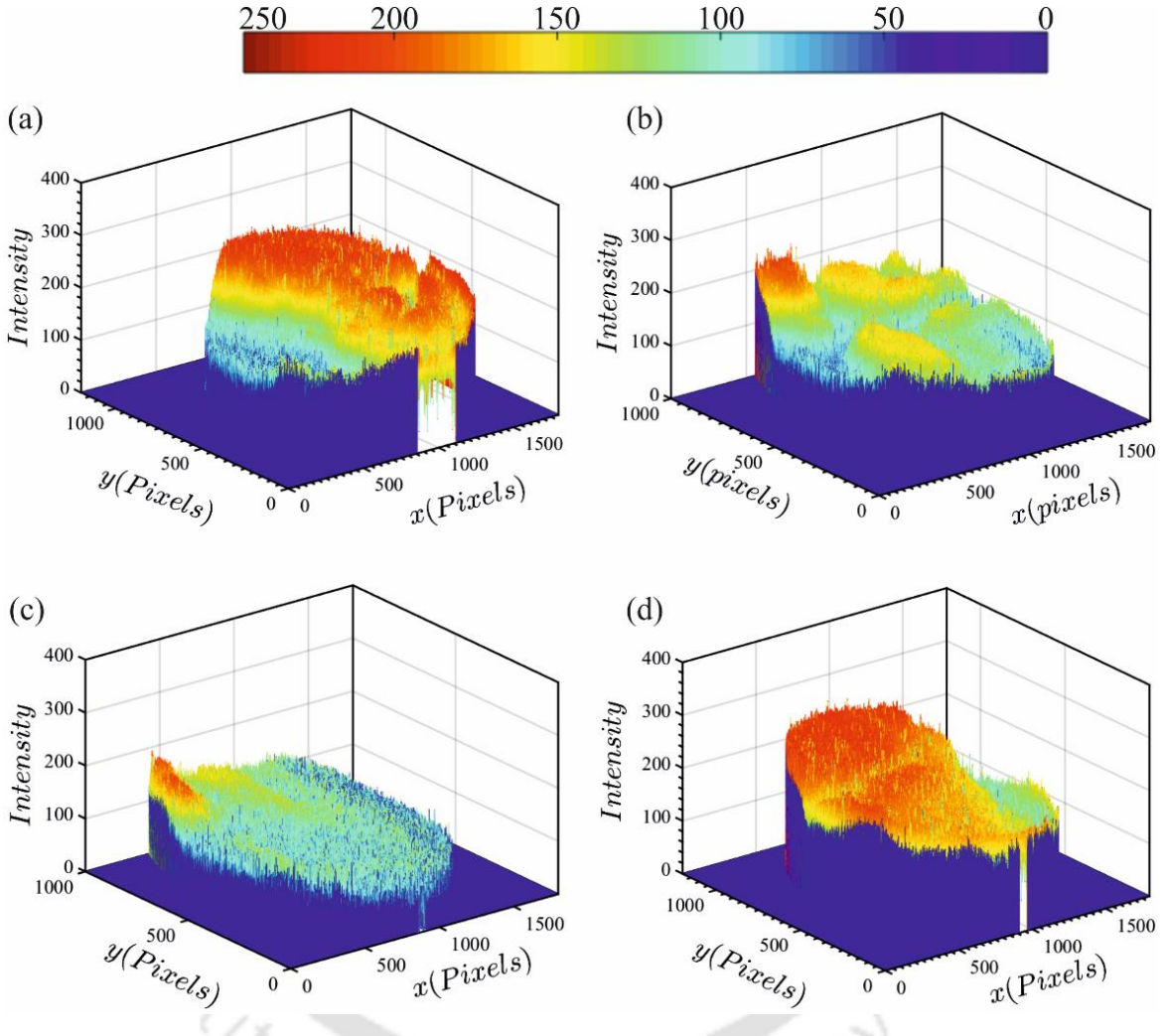

Fig. 5.9 Representative distribution of the fluorescence intensity at $\bar{T} = 0.14$ for the magnetic field frequency of (a) $f = 0.3\ Hz$ (b) $f = 1\ Hz$ (c) $f = 3\ Hz$ (d) $f = 5\ Hz$. The color bar shows the pixel intensity ranging from 0 to 255.

In Fig. 5.8, we show the distribution of the fluorescein intensity in the flow domain of the mixed droplet at different temporal instants. Important to mention here that a fully mixed state will have a uniform intensity distribution throughout the droplet flow field. Note that $\bar{T}$ represents the non-dimensional mixing time and is defined as $\bar{T} = t/T_0$, where t is the instantaneous time and T_0 is the total time of mixing between the two droplets in the absence of the magnetic field. In the presence of a magnetic field, the susceptibility mismatch between the two fluid leads to the development of flow instability. As a result of this instability and its

subsequent effect on bulk flow agitation, the overall mixing time between the two droplets is reduced substantially. From Fig. 5.8, we can see that the inhomogeneity in the fluorescence distribution gradually reduces over time. A closer observation of Fig. 5.8 is suggestive of a better mixing for $f = 3Hz$ case, as realized by a uniform fluorescein field in the domain even at earlier temporal instants $\bar{T} = 0.05$ and 0.14. Since the severe agitation in the flow field leads to an enhancement in mixing, this observation (fluorescein field for $f = 3\ Hz$) is in support with our argument of augmented flow velocity (which is the effect of severe agitation) for $f = 3Hz$ as discussed before. Thus, it can be argued that the mixing phenomena taking place inside the droplet flow field are a strong function of the frequency of the applied magnetic field. To further ascertain the mixing phenomena occurring between two droplets (precisely, between two fluids) in Fig. 5.8, we plot the distribution of the fluorescence intensity at $\bar{T} = 0.14$ in Fig. 5.9. We can clearly visualize from Fig. 5.9(c) an almost uniform fluorescein distribution inside the droplet flow field when the magnetic field frequency is maintained at $f = 3Hz$. Whereas substantial inhomogeneity exists in the droplet domain for the cases of $f = 0.3\ Hz,\ 1\ Hz,\ and\ 5\ Hz$.

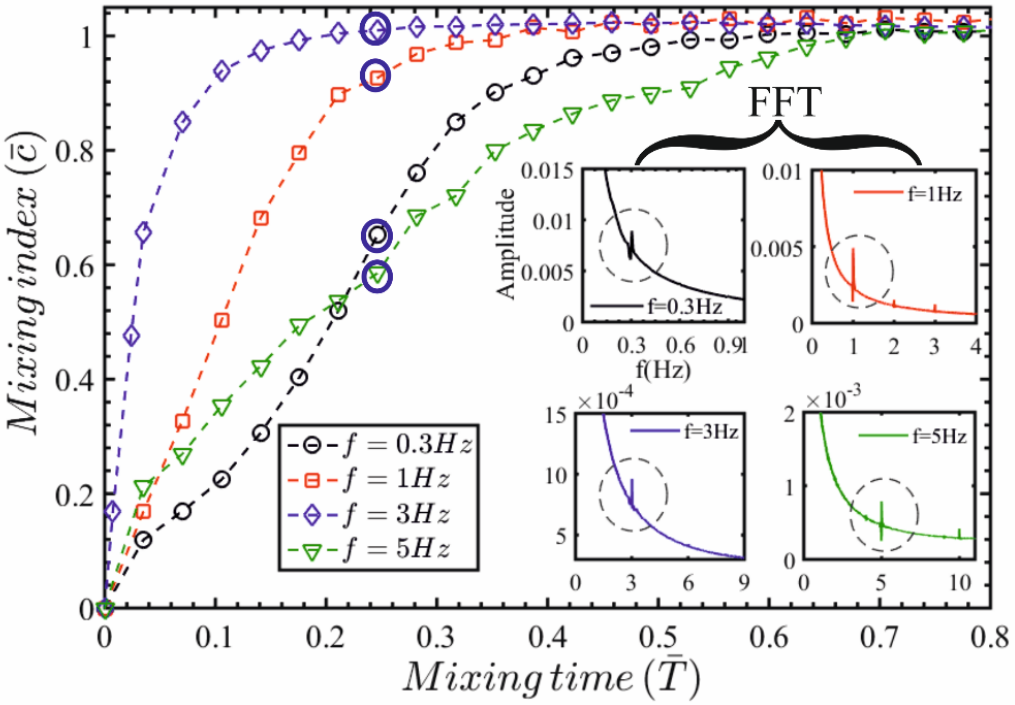

Fig. 5.10 Plot depicts the temporal variation of the mixing index ($\bar{C}$) of the droplet flow field for the magnetic field applied frequency of 0.3Hz, 1Hz, 3Hz, and 5Hz, respectively. The insets depict the Fast Fourier Transform of the mixing index for all the cases under consideration. The black color dotted circle highlights the peak of the Fast Fourier Transform curve. The blue color circle identifies the mixing index ($\bar{C}$) at $\bar{T} = 0.25$.

It is established by now that the perturbation frequency (f) of the magnetic field plays a dominant role in the magnetofluidic mixing of the microdroplet. In Fig. 5.10, we show the variation of the mixing index ($\bar{C}$) versus the non-dimensionalized mixing time, $\bar{T}(= t/T_0)$ for all the cases under consideration. The plot in Fig. 5.10 shows that for $\bar{T} = 0.25$, the mixing index ($\bar{C}$) varies as 0.62, 0.94, 0.99, and 0.58 (highlighted by encircled points) for the magnetic field actuation frequencies of 0.3 Hz, 1 Hz, 3 Hz, and 5 Hz, respectively. This particular insight signifies that rapid mixing is possible when the magnetic field frequency (f) is maintained at 3 Hz. The inset of Fig. 5.10 shows the Fast Fourier Transform (FFT) of the mixing index data. These FFT values justify that the applied magnetic field frequency is the dominant perturbing force acting on the droplet domain.

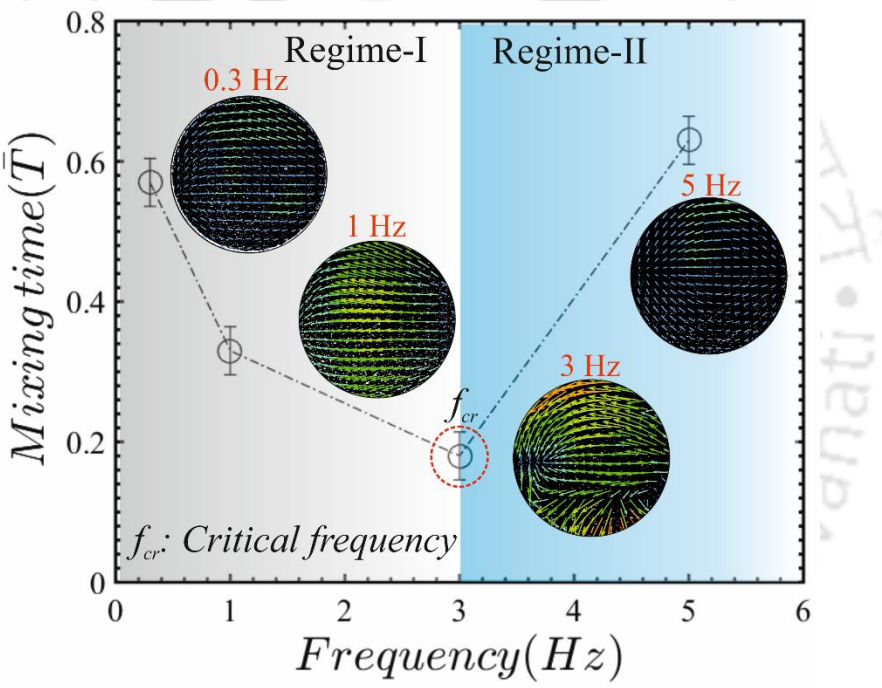

Fig. 5.11 Plots depict the experimental variation of the overall mixing time between the two droplets for the various perturbing magnetic field frequency(f). The black color hollow circle (O) indicates the experimental droplet mixing time at a particular frequency. The critical frequency is identified by the dotted red color circle. Regime-I indicates the zone in which mixing time is inversely related to magnetic field frequency. Regime-II indicates the zone in which the droplet mixing time is directly related to frequency of the magnetic field. The inset shows the velocity distribution inside the ferrofluid droplet domain for all the magnetic field perturbing frequencies.

In the preceding discussion, we have identified the presence of a critical frequency at which the time of the complete mixing process of the two droplets is minimum. Thus, the interactive role of the involved time scales viz., the advective, perturbation, and diffusive time scales on the mixing process is non-trivial as apparent from the ongoing discussion. We have previously seen that the advective and perturbation time scales are almost equal for $f = 3\ Hz$

case. Intuitively, the minimum time for complete mixing in the present scenario should be for $f = 3\ Hz$ case. In Fig. 5.11, we show the variation of the overall non-dimensionalized mixing time ($\bar{T}$) between the two droplets for the various frequencies of the perturbing magnetic field. The curve in Fig. 5.11 exhibits an initial negative (-ve) slope, and after reaching a critical value, it encounters a positive slope (+ve). As such, the curve in Fig. 5.11 can be divided into regime I and regime II, respectively. In regime-I, with an increase in the frequency of the perturbing magnetic field, the overall mixing time between the two droplets reduces. While in regime-II, an increase in frequency of the magnetic field from the critical one, increases the mixing time between the droplets. The critical frequency is encountered at the transition point from regime 1 to regime 2. At the critical frequency (f_{cr}), the flow encounters minimum mixing time. This minimum mixing time is primarily due to the aggravated agitations the droplet domain experiences at the critical frequency (cf. inset of Fig. 5.11).

B. Numerical perspectives

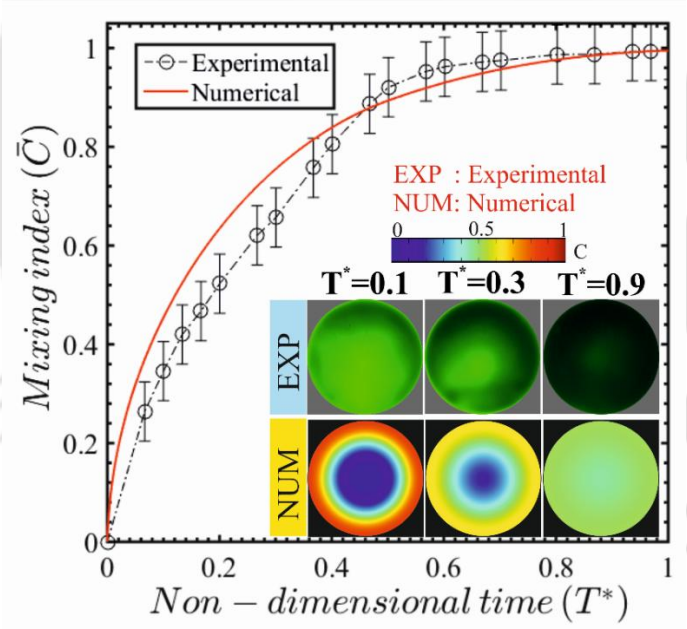

Fig. 5.12 Plot benchmarks the experimentally calculated mixing index with that of the numerically calculated mixing index, in the absence of an external magnetic field. $T^* = t/T_0$, where T_0 is the total time of mixing of the droplet. The inset shows the snapshots of the temporal evolution of the concentration flow field of the droplet.

In the present work, we have used bright field visualization, μPIV, and μLIF to comprehensively explore the droplet mixing characteristics. However, the adopted experimental methodologies have limitations in observing the instabilities in the concentration flow field of the droplet. In addition to that, the designed circuit of the electromagnet has its restrictions at very high magnetic field frequencies. Primarily because

of these reasons, numerical simulations are conducted in COMSOL Multiphysics® to explore the concentration field of the mixed droplet at higher frequencies. Also, we took advantage of simulations to have a qualitative understanding of the instabilities occurring in the droplet domain. In Fig. 5.12, we compare the simulated results of the mixing index ($\bar{C}$) with our experimental data in absence of any external magnetic forcing. A good match between the experimentally observed and numerically calculated mixing index justifies the reliability of our experiments. The inset of Fig. 5.12 shows the instantaneous numerical and experimental evolution of the droplet concentration field. The present numerical modelling framework, albeit 2D, is benchmarked with the experimental data and can be used as a tool to extract detailed insight in the droplet mixing physics.

We have discussed about the flow instability of two fluids (miscible) and argued its effect on the underlying mixing in the preceding section. It is worth mentioning here that the instability is induced in the droplet flow domain due to the magnetic susceptibility mismatch between the two fluids. These disparities in the effective magnetization ensure an increase in the overall interfacial area leading to the development of "***finger-like***" fronts, as can be observed from Fig. 5.13(a). Note that the "***finger-like***" fronts appearing at the interface are an indicative measure of the flow instability. We show in Fig. 5.13(a) the temporal evolution of the concentration field for various perturbing frequencies. Although the prime aim of the present endeavor is not to critically analyze the instability picture, yet we have discussed the "***finger-like***" fronts being developed at the interface during magnetic perturbation for a broader understanding of the mixing dynamics in the present scenario.

It is worth mentioning here that the instability picture, as discussed above, is not the numerical artifact; instead, the appearance of the ***"finger-like"*** structures is the consequence of the mismatch of the magnetic susceptibility of two fluids. With the alteration in the frequency of the magnetic field, the distinctive spatial variation of the concentration flow domain is apparent. A closer inspection of Fig. 5.13(a) reveals that the numerical results showing the uniform distribution of the concentration field for $f = 3Hz$ are in coherence with the experimental observations, as demonstrated in Fig. 5.8. Moreover, at higher magnetic field frequencies, the droplet domain attains an almost constant behavior. This constant behavior is primarily due to the fact that at a higher perturbing frequency, the magnetic perturbation time scale is very low as compared to the advective time scale of the flow, i.e., $t_m \ll t_U$. Consequently, under the application of very high magnetic field frequencies, any perturbation could not be fully propagated, and the droplet domain behaves as if it is acted

upon by two magnets under steady operations. Figure 5.13(b) shows the numerical and experimental evolution of the concentration flow field at the critical frequency of 3Hz. Consistency in the concentration flow field between the experimental and numerical results, as observed in Fig. 5.13(b), justifying the reliability of the modeling framework developed in this analysis.

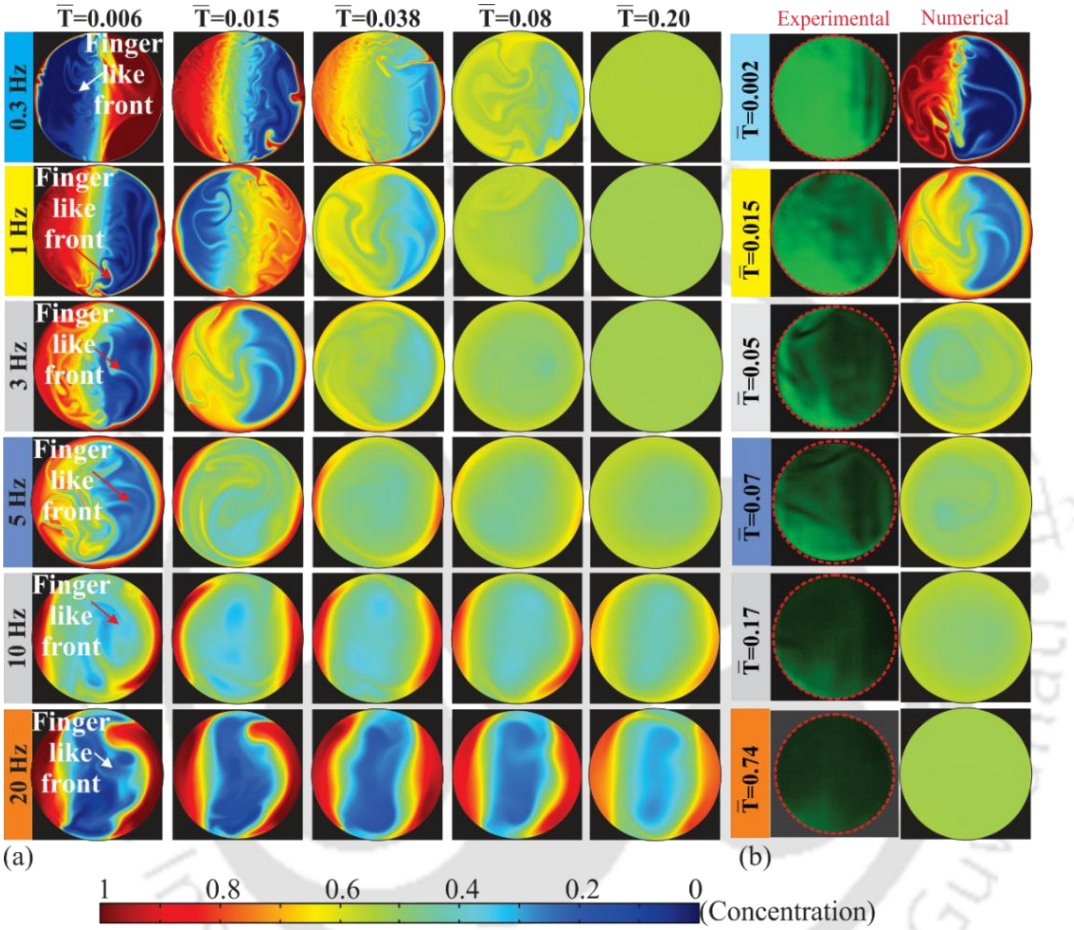

Fig. 5.13 (a) Concentration distribution inside the droplet flow field at various temporal instances of the droplet mixing process for the magnetic field applied frequency of 0.3 Hz, 1 Hz, 3 Hz, 5 Hz, 10 Hz and 20 Hz respectively. The black and white-colored arrow identify the finger-like front developed in the droplet domain due to the magnetization differences between the two fluids. (b) Plots depict the temporal evolution of the experimental and numerical variation of the concentration flow field when the magnetic field frequency is maintained at 3Hz.

5.4 SUMMARY

In the present study, the mixing dynamics of a ferrofluid droplet with a non-magnetic droplet under the influence of a time-dependent magnetic field have been investigated. The intermittent motion of magnetic nanoparticles (MNPs) under the external forcing induces a magneto convective flow inside the ferrofluid droplet. By performing the bright field visualizations, we obtain the qualitative understanding of the MNP's motion inside the

ferrofluid droplet, while μPIV investigation is carried out for quantification of the bulk flow dynamics inside the domain. As observed, the flow convection inside the ferrofluid droplet gets augmented in the presence of a time-dependent magnetic field. The flow dynamics inside the ferrofluid droplet is numerically simulated, specifically to explore the existence of interfacial instability, which initiates the mixing in the present problem. A mismatch of the magnetic susceptibility of two fluids, together with the viscosity contrast, triggers the mixing in the convective mixing regime. A critical frequency is observed at which the internal convection inside the droplet is amplified in the presence of a magnetic field. At this critical frequency, the advective time scale of the flow is balanced by the magnetic perturbation time scale. This balance ensures optimal reciprocation of the MNPs in between the two magnetically active zones. At a lower frequency, the residence time of the MNPs at a particular magnetically active zone increases, ensuring that the agitated energy of the bulk flow is dissipated by the viscous energy of the flow. While at a higher frequency, the MNPs are unable to reach the magnetically active zone, thereby restricting the agitation developed in the bulk flow to a particular limit. Since the agitation developed in the droplet domain is maximum at the critical frequency, the time of complete mixing between the two droplets becomes minimum at this frequency. The critical frequency obtained from the experimental observations is in good agreement with the numerical result. At the critical frequency, the overall mixing time between the two droplets is reduced by almost 80% when compared with the base case, i.e., no applied magnetic field. The proposed technique may enable numerous biomicrofluidic and Lab-on-a-CD based applications towards achieving efficient mixing in a less invasive way.

Chapter 6

EFFECT OF TIME-DEPENDENT MAGNETIC FIELD ON THE EVAPORATION DYNAMICS OF A SESSILE FERROFLUID DROPLET

The previous investigations have shown that tailoring the magnetic nanoparticles motion is possible with a time-dependent magnetic field. In this chapter, we investigate the role of the magnetic nanoparticles' transient motion on the evaporation kinetics of the ferrofluid droplet. Bright field visualization and μ-PIV measurement technique are employed for qualitative and quantitative understanding of the droplet's internal hydrodynamics. The evolution of the droplet morphology in the presence of a magnetic field is captured using a CMOS camera. The role of the various timescale on the overall lifetime of the sessile ferrofluid droplet is highlighted. The characteristics stages that the ferrofluid droplet encounters while evaporating in the presence of a time-dependent magnetic field are outlined as well.

6.1 INTRODUCTION

Although the role of a steady magnetic field on the evaporation kinetics of a ferrofluid droplet is known (Jadav et al. 2017; Saroj and Panigrahi 2019). In this chapter, we experimentally investigate the evolution of the ferrofluid droplet in a controlled atmosphere when perturbed by a time-dependent magnetic field with various frequencies. Modulation of the evaporation dynamics by careful maneuvering of the magnetic particle migration is highlighted. At first, the droplet's external characteristics under the influence of a time-dependent magnetic field, as manifested by the change in its height, contact angle, and diameter, are explored. A significant deviation of the evaporation characteristics of the magnetically perturbed ferrofluid droplet from the no magnet case (when no magnetic field perturbs the droplet domain) is highlighted as well. The time-dependent nature of the magnetic field stretches the contact line region, thereby increasing the overall evaporative surface area of the droplet (Fig. 6.1(a)). To explore the underlying physical issues of these characteristics, the internal hydrodynamics of the droplet is investigated both qualitatively and quantitatively, using bright-field visualization and μPIV measurement, respectively.

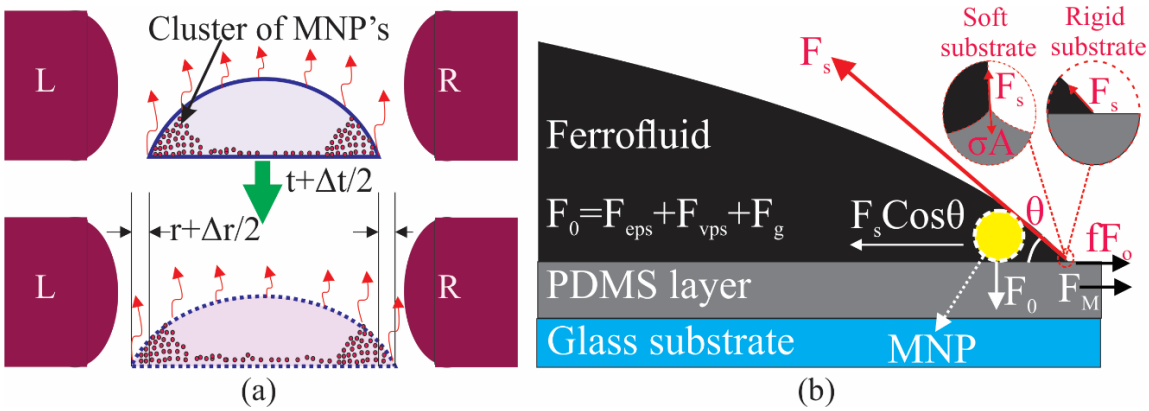

Fig. 6.1 (a) Schematic showing the particle migration in the ferrofluid droplet and the subsequent motion of the contact line after a time instance of $t + \Delta t$, in the presence of two alternatively perturbing electromagnets. 'L' and 'R' denote the left and right electromagnet, respectively. (b) Schematic illustrates the forces acting on a magnetic nanoparticle (MNP) at the contact line. $F_{eps}, F_{vps}, F_g, F_s, and\ F_M$ denotes the electrostatic, Vandaar-waals, gravity, surface tension, and magnetic force, respectively. f denotes the friction factor. The left zoomed-in figure shows the deformation near the three-phase contact line on the soft substrate due to the balance between the liquid surface tension force (F_s) and the substrate yield force. σ denotes the substrate yield stress, A denotes the area of the three-phase contact line. The right zoomed-in figure shows the deformation near the three-phase contact line on the rigid substrate.

6.2 MATERIALS AND METHODS

6.2.1 Surface preparation and fluid characterization

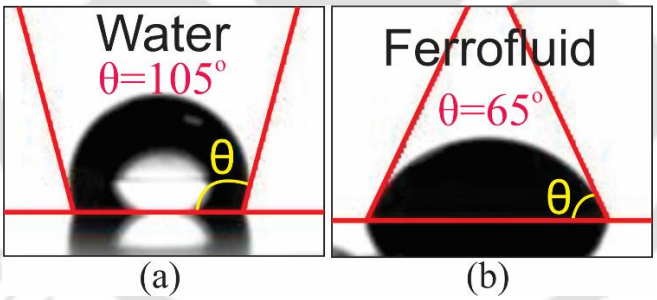

Fig. 6.2 Plot shows the static contact angle of (a) water and (b) ferrofluid droplets on the treated PDMS substrate. The volume of the sessile droplet is around 1.5µl.

The preparation of the substrate is discussed in detail in section 2.6 of chapter 2. In Fig. 6.2, the hydrophobic behavior of the treated substrate is demonstrated, where deionized water forms a static equilibrium contact angle of $\theta_{water} = 105°$. However, the prepared ferrofluid solution forms a contact angle of $\theta_{ferrofluid} = 65°$. This reduction in contact angle is primarily since the magnetic nanoparticles in the ferrofluid solution are coated with surfactant (lauric acid) to avoid agglomeration (Rosensweig 1984; Odenbach 2002). The treated substrate, in which, the ratio of the oligomer and the curing agent was 10:1, has the modulus of elasticity (E) of around 1.5MPa (Lopes and Bonaccurso 2012, 2013; Dey et al. 2015). The stiffness of the prepared substrate can be quantified by a softness parameter γ/ER, where R

is the macroscopic length scale and γ is the surface tension of the liquid with air (Marchand et al. 2012; Lubbers et al. 2014). For $E = 1.5\ MPa$, the softness parameter for the prepared PDMS substrate was found to be $O[\gamma/ER] \sim 10^{-6}$. This low value of softness parameter ensures the substrate behaves as an "apparently rigid substrate", as such no wetting ridge formation is observed in the present work (Marchand et al. 2012; Lubbers et al. 2014). The preparation and characterization of the ferrofluid solution are elaborately discussed in section 2.7 of chapter 2.

6.2.2 Electromagnet assembly

We fabricate two electromagnets (L and R) for intermittent perturbation of the droplet domain. The fabrication and operation of the electromagnet are clearly explained in section 2.5 of chapter 2. Note that the electromagnets are kept at a distance of around 2.5 mm from the droplet's center. The electromagnet is activated by supplying current from a DC power source (Make: Aplab). For generating time-dependent magnetic fields, we have developed an in-house digital circuit to supply pulsed current to the electromagnet. The arrangement is made such that when 'L' is in "ON" state, 'R' remains in the "OFF" state, thereby ensuring that only one electromagnet remains in the "ON" state at a particular instant of time. Note that, in the present study, a magnetic field of strength $\bar{B}$ = 640 G and actuation frequencies f = 0.5, 1.0, and 3Hz is applied to the ferrofluid droplet. The magnetic field is measured at the surface of the electromagnet facing the droplet by a Gaussmeter (Make: SES Instruments). The droplet-electromagnet assembly is covered with a glass lid to minimize the effects of convection of surrounding air on the evaporation kinetics and internal convection. While performing experiments, the electromagnets are actuated once the droplet reaches its static contact angle.

6.2.3 Experimental procedure and droplet visualization.

In this study, we explore the implications of the magnetic field induced convections on the internal as well as external hydrodynamics of the ferrofluid droplet. The internal hydrodynamics is investigated with the help of a µPIV set-up, while the external hydrodynamic features of the ferrofluid droplet are quantified by the changes in the contact angle, diameter, and height of the droplet. The Goniometer (Make: ACAM-NSC) is used to measure the contact angle. The details of the goniometer are mentioned appropriately in section 2.2 of chapter 2. Note that the set-up consists of a droplet-dispensing module, a white LED light, a diffuser, and a CMOS camera. A sessile droplet of volume 1.5µl is dispensed into the treated substrate with the help of the droplet-dispensing module (speed range: 0.038-

16µl/s). The white LED, together with the diffuser, is used to illuminate the droplet volume. The images are captured with a CMOS camera, having an image resolution of 744 x 480 pixels^2. The acquired images are post-processed in ImageJ (Schneider et al. 2012), and an in-house code is developed to decipher the information from the processed images. To mention, from these processed images, we calculate the following parameters, such as the change in diameter, height, and contact line velocity of the droplet (see section 2.2 of chapter 2 for more detail).

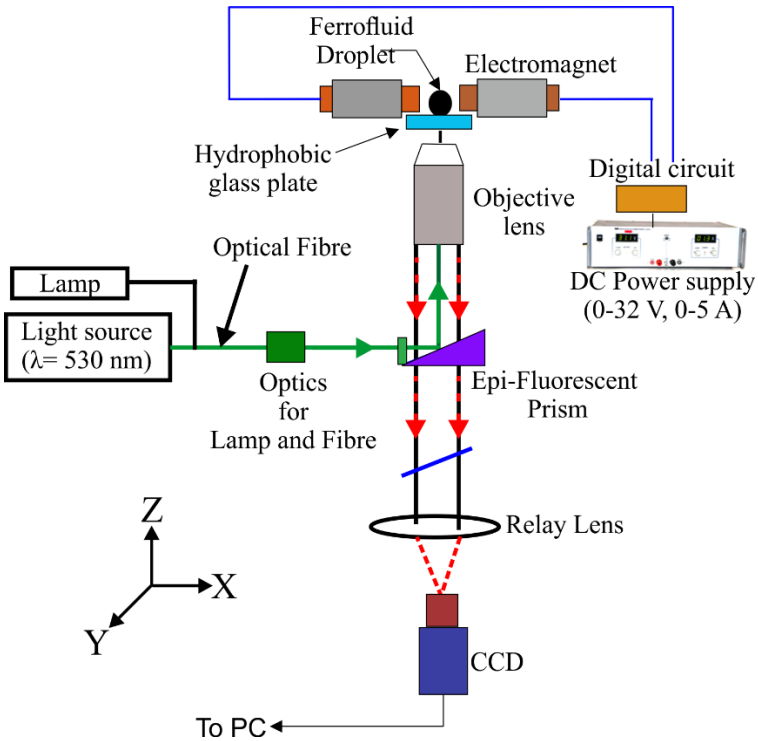

Fig. 6.3 Schematic representation of the µPIV experimental set-up, used for quantifying the internal flow hydrodynamics of the ferrofluid droplet. The components used in the experiments have been shown in several schematics, and their functions have been well defined in the text.

We measure the velocity field inside the droplet by µPIV techniques. The µ-PIV system, as schematically shown in Fig. 6.3, consists of three main components, viz, (i) an inverted microscope (Make: Leica, DM IL LED), (ii) a fluorescent light source (Make: Leica), and (iii) a CCD camera (Make: Leica). The ferrofluid droplet is seeded with 1µm diameter fluorescent microspheres (Make: Molecular Probes Inc.). The fluorescent particles ensure acceptable low noise levels under the present illumination conditions. The details of the µ-PIV investigations are explained elaborately in section 2.4 of chapter 2.

The mass loss of the droplet due to evaporation is measured with the help of a weighing balance (Make: AND-GR202) having a minimum resolution of 0.01mg. The temperature and the humidity inside the laboratory are maintained at $25 \pm 0.5°C$ and $67 \pm 1\%$, respectively. The Bond number ($Bo = \Delta\rho g D_h^2/\gamma$) is less than one, where ρ, g, D, γ

represents the density, acceleration due to gravity, diameter, and surface tension, respectively. The magnetic bond number is calculated as $Bo_m = \mu_0 H^2 D_h/\gamma$, where μ_0, H_0 represent the permeability of free space and magnetic field strength(A/m), respectively. For the present case $Bo_m \gg 1$, signifying the dominance of magnetic force over the surface tension force. Each experiment is repeated four times for the repeatability. The maximum uncertainties involved in each run does not exceed 8%.

6.3 RESULTS AND DISCUSSION

In this section, we first elucidate the evaporation characteristics of the ferrofluid droplet, when perturbed by the time-dependent magnetic field. We investigate the changes in the droplet diameter, height, contact angle for the various frequencies of the perturbing magnetic field, as considered in this study. Further, we explore the internal hydrodynamics of the droplet, and in doing so, we focus on the motion of the magnetic nanoparticles (MNPs) and the bulk flow behaviour.

6.3.1 Evaporation characteristics of the ferrofluid droplet

To study the evaporation behaviour of the droplet, we have quantified the temporal change in the contact angle, diameter, and height of the droplet. Also, the variation of the droplet volume with time is calculated as one of the essential characteristics of the droplet evaporation kinetics. The contact angle (θ^*), height (H^*), and diameter (D^*) of the droplet are non-dimensionalized with their initial droplet contact angle, diameter, and height, respectively as $\theta^* = \theta/\theta_0$, $H^* = H/H_0$, $D^* = D/D_0$ where the subscript '0' indicates the initial value. In Fig. 6.4(a), we show the dynamical changes in the contact angle (both left and right contact angle) when two electromagnets perturb the droplet domain alternatively. As seen in Fig. 6.4(a), whenever the left electromagnet is in the ON stage, the left contact angle (θ_L) attains a higher value as compared to the right contact angle and vice-versa. This observation can be attributed to the magnetic forcing driven movement of the MNPs inside the droplet. The migration of the MNPs towards the active magnet increases the surface energy of the liquid-air interface (near the active magnet). The increased surface energy results in a higher contact angle of the liquid-air interface nearer the active magnet zone. Important to mention, this increase in the contact angle of the liquid-air interface at the active magnet zone further leads to a decrease in the contact angle of the liquid-air interface that is maintained at the nearby end of the inactive magnet zone. The snapshots in the inset of Fig. 6.4(a) shows the droplet morphology at particular time instants. The presented snapshots support our argument of increased contact angle at the contact line of the active magnet and

vice versa. Note that a spontaneous reduction in the magnitude of the contact angle can also be observed as time proceeds. This reduction in the contact angle is primarily due to the prevailing mode of evaporation (precisely DCVR mode of evaporation) wherein the mass of the droplet is getting lost. In the forthcoming discussion, we investigate the existing modes of evaporation exhibited by the droplet in the presence of a time-dependent magnetic field in greater detail.

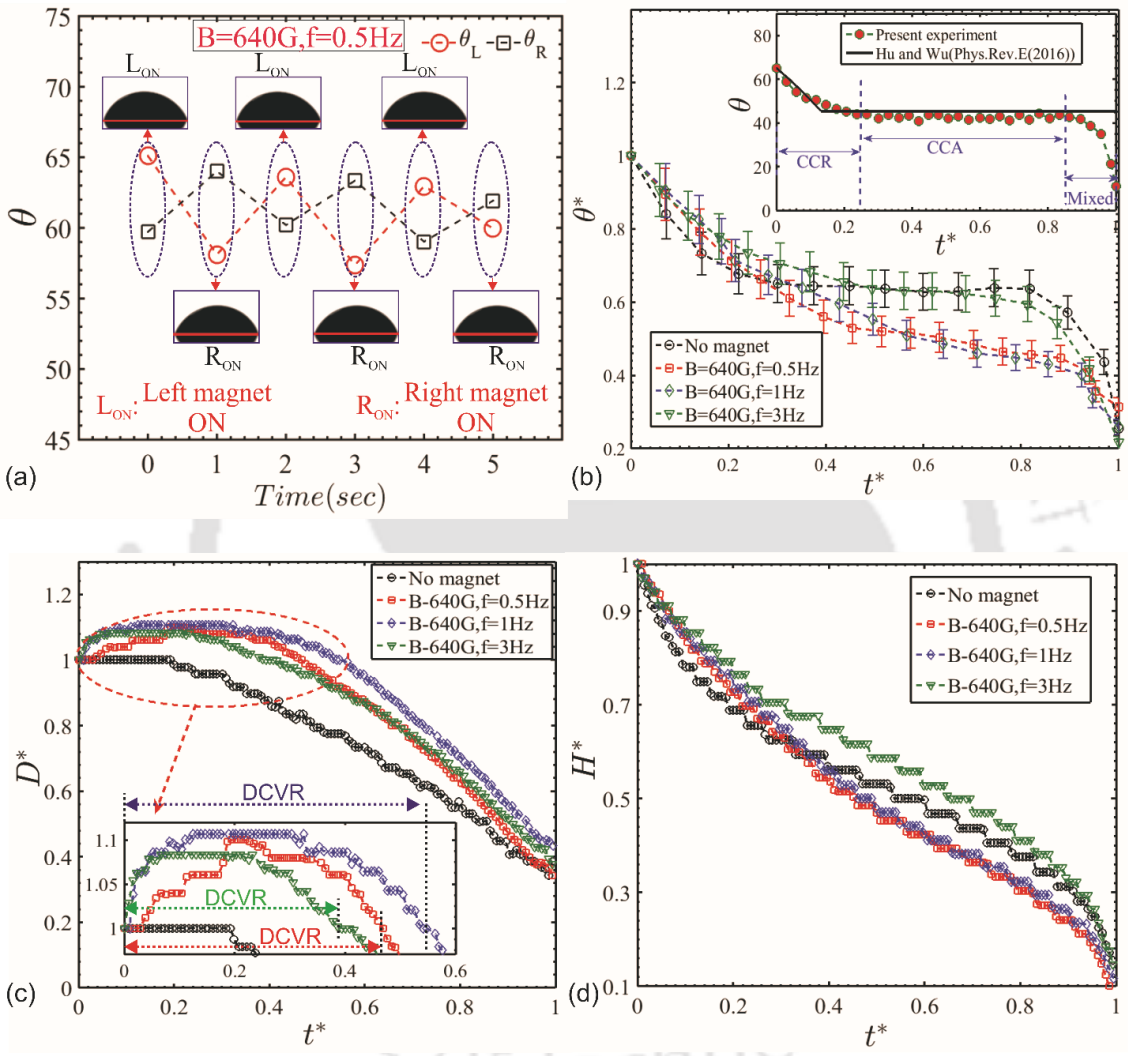

Fig. 6.4 (a) Plot shows the variation of the contact angle (θ_L, θ_R) when the left magnet and right magnet is switched On alternatively, for f=0.5Hz, B=640G (b) Plot depicts the variation of non-dimensional contact angle (θ^*) for the various investigating cases. The inset figure illustrates the stages of evaporation of a ferrofluid droplet in the absence of a magnetic field. (c) The plot shows the temporal variation of the droplet diameter(D^*) as it evaporates. (d) The plot illustrates the change in height (H^*) of the droplet throughout its evaporation life-time. The t^* is the non-dimensionalized time and is given by $t^* = t/t_E$, where t_E is the total life-time of the droplet.

Figure 6.4(b) shows the changes in the contact angle when the frequency of the perturbing magnetic field is varied. In the absence of a magnetic field, the ferrofluid droplet evaporates following three distinct modes (cf. Fig. 6.4(b)-inset), viz, the constant contact radius mode (CCR), the constant contact angle mode (CCA), and the late-stage mixed mode.

At the initial stage, it evaporates in constant contact radius mode (CCR). In the CCR mode, a sharp drop in contact angle takes place while the triple contact line of the droplet remains pinned. With this spontaneous decrease in the contact angle of the droplet, a stage arrives where the de-pinning force ($F_{depinning}$, the force responsible for depinning the triple contact line) becomes higher than the intrinsic energy barrier $\left(\frac{\partial U}{\partial r}\right)$. Note that this energy barrier tends to pin the interface of the triple contact line (Orejon et al. 2011). Primarily due to this depinning force $F_{depinning} > \frac{\partial U}{\partial r}$, the triple contact line recedes, and the evaporation process continues following constant contact angle mode (CCA). In the CCA mode of evaporation, the contact angle remains almost constant while the contact radius decreases. In the final stage of evaporation (Mixed-mode), the contact line recedes as well as the contact angle decreases. Also, to check the correctness of experimental methods, the change in contact angle (θ) for the base case (No magnet case) is validated with the theoretical results of Hu and Wu (Hu and Wu 2016). A reasonable agreement can be observed between the two results, except for the late stage of evaporation. This discrepancy is mainly because the theoretical modeling framework of Hu and Wu (Hu and Wu 2016) didn't account for the late mixed stage of evaporation in the underlying analysis. The modes of evaporation get altered when the time-dependent magnetic field perturbs the droplet domain, as can be seen from Fig. 6.4(b). The contact angle of the droplet in the presence of a time-dependent magnetic field decreases in three typical stages. In the initial stage of evaporation, the slope of the contact angle is high, followed by the mid-stage, where the slope decreases. In the late stage of evaporation, a sharp decrease in contact angle can be observed. In the subsequent discussion, we will see that these characteristic variations of the contact angle of the ferrofluid droplet in the presence of a time-dependent magnetic field are due to the presence of new modes of evaporation altogether.

We show in Fig. 6.4(c), the temporal variation of the droplet diameter (D^*) as it evaporates. Having a closer look at Fig. 6.4(c), the observations made are as follows: in the absence of a magnetic field, the contact line remains pinned (CCR mode) for about 20% of the total evaporation time, and then a spontaneous decrease in diameter (CCA mode) takes place. However, in the presence of a magnetic field, the diameter of the droplet increases at the initial temporal instants attains a peak value, and finally decreases with time. To mention, this observation holds true for all the perturbing frequencies considered in this study. This observation agrees with our proposition that the droplet evaporation kinetics in the presence of a time-dependent magnetic field does not follow any CCR or CCA modes, since at no stage

of evaporation, as shown in Fig. 6.4(a)-(d), neither the diameter nor the contact angle of the droplet remains constant. Quite remarkably, we have recognized these new modes of evaporation kinetics through the present experimental investigations and termed them as DCVR (Decreasing contact angle and variable radius), DCDR (Decreasing contact angle and decreasing radius), and late mixed modes. Notably, the new modes of droplet evaporation in the presence of a time-dependent magnetic field are in sharp contrast to the established modes, as observed in the absence of a magnetic field. In the DCVR mode of evaporation, the contact angle decreases, while the diameter of the droplet encounters a rise and fall pattern. The duration of evaporation in this particular zone is calculated until the diameter of the droplet reduces to $D^* = 1$. As seen in Fig. 6.4(c), the diameter of the droplet increases at the initial temporal instants of this mode. This is primarily because of the interplay of the forcing factors under the modulation of magnetic field. To be precise, the applied force barrier (i.e., the magnetic force, F_M) is greater than the combined strength of de-pinning $(F_{depinning})$ and pinning $(F_{pinning})$ forces. The pinning force $(F_{pinning})$ is the algebraic sum of electrostatic force (F_{eps}), Van der Waals force (F_{vap}) and the gravity force (F_g) (cf. Fig. 6.1b, for the involved forces near the contact line). The de-pinning force $(F_{depinning})$ is given by $\gamma \sin\theta_0 \delta\theta$, where γ is the surface tension of the fluid (Orejon et al. 2011). Note that $\delta\theta = (\theta_0 - \theta(t))$ and $\theta(t)$ is the instantaneous contact angle. As the droplet evaporates, $\theta(t)$ decreases continuously, leading to an enhancement of the de-pinning force $(F_{depinning})$.

Fig. 6.5 Snapshots depicts the temporal evolution of the evaporating ferrofluid droplet for the various cases under investigation. All the respective modes of evaporation at that particular temporal instant are highlighted. The t^* is the non-dimensionalized time and is given by $t^* = t/t_E$, where t_E is the total lifetime of the droplet.

Therefore, in the subsequent stages of evaporation, the de-pinning force $(F_{depinning})$ becomes greater than the combined strength of the pinning $(F_{pinning})$ and applied magnetic (F_M) forces. At this stage, the triple contact line will start receding following this enhanced

de-pinning force $\left(F_{depinning}\right)$ and results in the decrease of the droplet diameter. As the droplet diameter becomes $D^* = 1$, we observe a spontaneous decrease in height, diameter, and contact angle of the droplet with an almost constant slope, as witnessed in Fig. 6.4. In this zone, the droplet evaporates following the DCDR mode. The late mixed mode of evaporation follows this mode.

In Fig. 6.4(d), we show the temporal variation of the height of the droplet. A spontaneous decrease in the height of the droplet can be easily observed for all the cases under consideration as time grows. Thus, we can conclude that the DCVR mode of evaporation kinetics ensures the stretching of the diameter of the droplet during initial temporal instants. Important to mention, this stretching further implies an increase in the triple contact line area. This fact, in particular, has tremendous implications on the overall life-time of the droplet, as discussed in greater detail in one of the succeeding sections. Note that the duration of the DCVR mode of evaporation is dependent on the frequency of the perturbing electromagnet and is seen to follow the order $t_{1\ Hz} > t_{0.5\ Hz} > t_{3\ Hz}$, as witnessed in Fig. 6.4(c). Snapshots showing the image of the evaporating droplet obtained at different temporal instants are shown in Fig. 6.5. The instantaneous evolution of the droplet wetting characteristics is directly related to the frequency of the perturbing magnetic field, as can be seen in Fig. 6.5. As already observed, the duration of the DCVR mode of evaporation is maximum for the 1Hz case as compared to all the other involved cases.

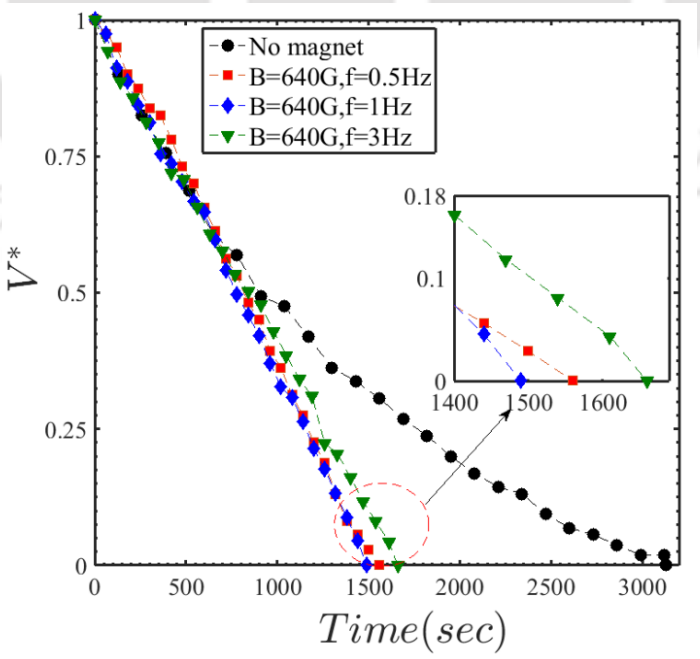

Fig. 6.6 Plot illustrates the change of the non-dimensionalized volume (V^*) of the ferrofluid droplet for all the investigating cases under consideration. The inset figure is an enlarged view of the dotted red circled area. (V^*) is the non-dimensionalized volume and is given by V/V_0.

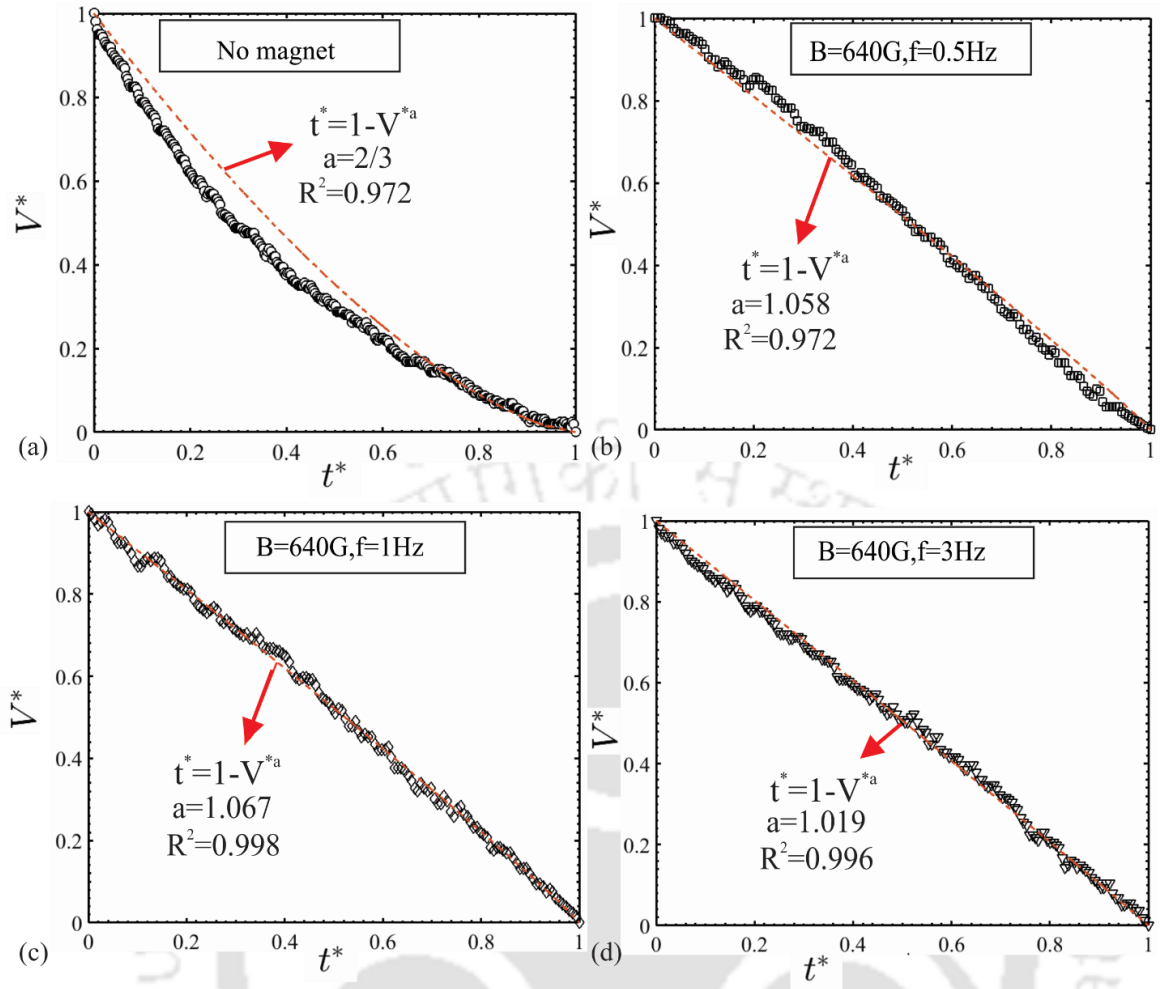

Fig. 6.7 Plots depicts the variation of the non-dimensional volume (V^*) for the non-dimensional time (t^*) along with the respective fitted curve for (a) No magnetic field applied, (b) $\bar{B}$=640 G, f=0.5 Hz, (c) $\bar{B}$=640 G, f=1 Hz, (d) $\bar{B}$=640 G, f=3 Hz. The droplet evaporates following the equation: $t^* = 1 - V^{*a}$, where 'a' is the constant.

In Fig. 6.6, we show the evolution characteristics of the droplet being perturbed by the time-dependent magnetic field. It can be observed from Fig. 6.6 that, under the influence of the magnetic field, the droplet is evaporating at almost half the time it evaporates in the absence of a magnetic field. Note that when the magnetic field frequency is maintained at f = 1 Hz, the droplet takes minimum time to evaporate, while the droplet takes maximum time to evaporate at f = 3 Hz, as shown in the inset of Fig. 6.6. Important to mention, there is a change in the curve characteristics between the "No magnet" case and in the presence of time-dependent magnet cases. It is important to mention in this context here that a droplet in the absence of magnetic forcing evaporates following stick-slip mode ensuing the 2/3rd power law ($t^* = 1 - V^{*a}, a \sim 2/3$) (Nguyen and Nguyen 2012, 2014; Xu et al. 2013; Stauber et al. 2014). In Fig. 6.7, we show the temporal variation of droplet volume along with the fitted curve for all the cases under consideration. It can be seen from Fig. 6.7 that, in the absence of

magnet, the droplet evaporates following the 2/3rd power law. However, when a time-dependent magnetic field perturbs the droplet domain, the value of a~1 and this particular value of 'a' is suggestive of the fact that the droplet evolution characteristics get linearized in the presence of the magnetic field. Also, the value of constant 'a' varies in the order $a_{1\ Hz} > a_{0.5\ Hz} > a_{3\ Hz}$, as can be seen from Fig. 6.7(a)-(d). Notably, this inference is in clear support with the previous observation on droplet life-time, i.e., the droplet life-time is minimum for the 1 Hz case. From the observations made in the above figures (Fig. (6.4)-(6.6)), an interesting unaddressed question emerges as to *What is the role of the frequency of the perturbing magnetic field on the droplet evaporation kinetics?* In the succeeding sections, we observe the internal hydrodynamics of the ferrofluid droplet in the presence of a time-dependent magnetic field to gain insights into the mechanism of the evaporation kinetics. Precisely the internal hydrodynamical features of the droplet will address the above issue as discussed next.

6.3.2 Internal hydrodynamics in the presence of the magnetic field

In this section, we explore the effect of time-dependent magnetic field on the internal hydrodynamics of the ferrofluid droplet. We perform out this particular analysis to understand the behaviour of the MNPs and the bulk flow of the droplet on its evaporation kinetics. In Fig. 6.8, we show the motion of the MNPs, when disturbed by various frequencies of the magnetic field (precisely 0.5 Hz, 1Hz, and 3Hz). The whole cycle of operation of an individual electromagnet is divided into four equal parts, where 'T_M' represents the time period of operation of the magnetic field. The snapshots showing the image at different temporal instants are given accordingly. We can see that, on switching the magnet to the ON state, the MNPs migrate towards the active magnet. Note that the MNPs, on reaching the magnetically active zone, arrange themselves in chain like-cluster formation. This formation is the resultant effect of the interparticle dipole-dipole interaction between the MNPs in the presence of the active electromagnet, as given by $I_m(ij) = -\left[3\frac{(m_i \cdot r_{ij})(m_j \cdot r_{ij})}{r_{ij}^5} - \frac{m_i m_j}{r_{ij}^3}\right]$, where $r_{ij} = r_i - r_j$ is the distance between the i_{th} and j_{th} nanoparticles having magnetic moments m_i and m_j respectively (Mendelev and Ivanov 2004). The formed cluster breaks down once the magnetic force is applied from the other end (In this study, two magnets, placed diametrically opposite to each other, are used to energize the droplet). Note that at high frequency (Precisely 3 Hz), due to the low time-duration of the perturbation, the MNPs do not possess sufficient time to move from one side of the magnetically active zone to the other side. As a result of this low perturbation time, the motion of MNPs is localized in the region AA' (cf. Fig. 6.8(a)).

Furthermore, in Fig. 6.8(b), we show the zoomed-in view of the MNPs motion at the vicinity of the contact line of the active magnet (Left magnet). It can be clearly observed that the MNPs agglomerates in a chained-cluster formation for the f=0.5Hz case. While for the f=3 Hz case, no cluster formation takes place due to the inability of the MNPs to reach the contact line. The motion of the MNPs is tracked manually with the help of an ImageJ plugin "Manual tracking" (Schneider et al. 2012), following which the average velocity of the MNP (U_p) was found to be of the order of 4300 $\mu m/s$.

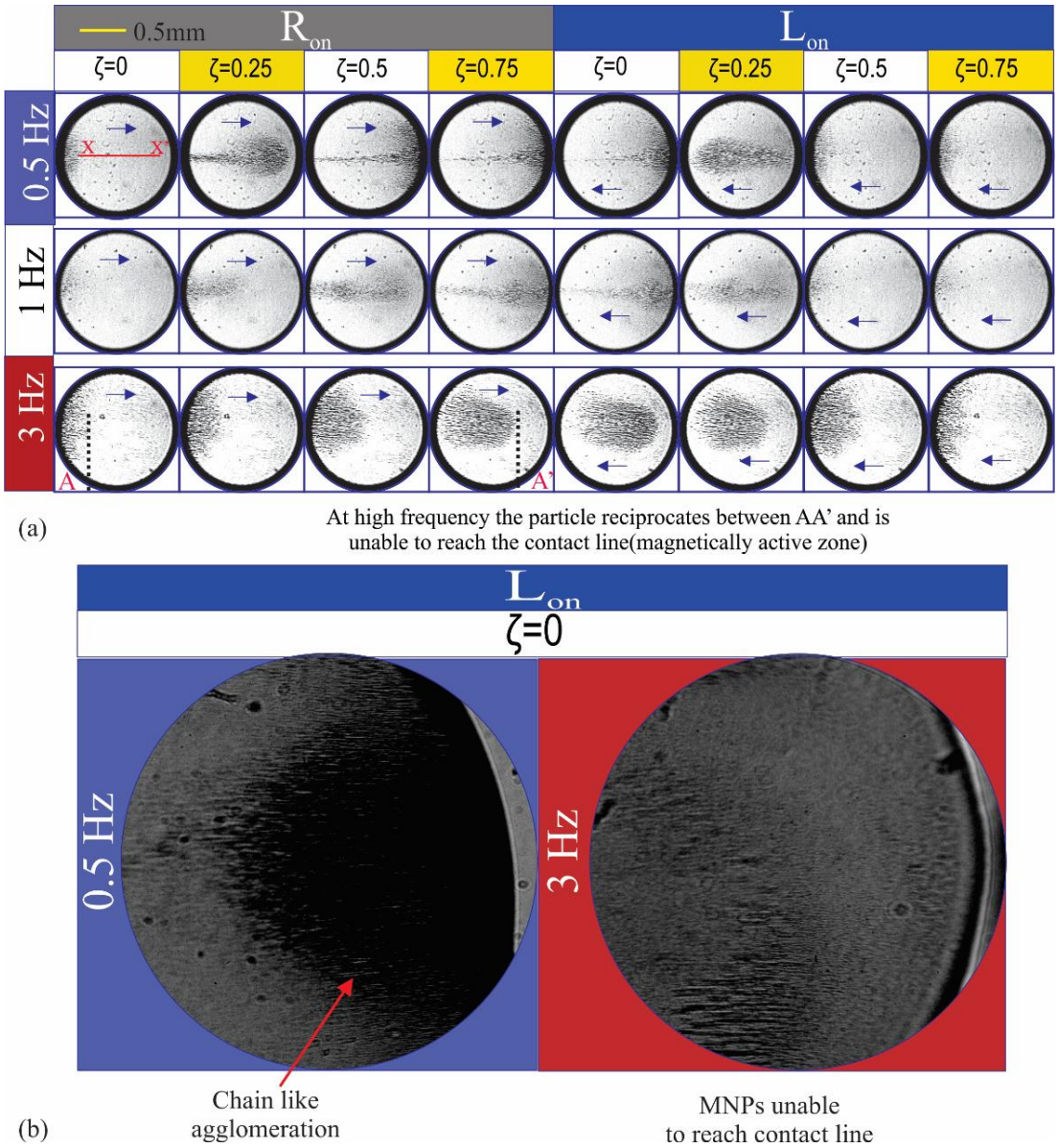

Fig. 6.8 (a) Bright field visualization of the droplet at various times of operation of the magnetic field, when the frequencies of the electromagnets are varied from f=0.5Hz, 1Hz, and 3Hz, respectively. The blue colored arrows show the direction of motion of the MNPs. 'T_M' denotes the time period of operation of an individual electromagnet. AA' denotes the zone in which the MNPs reciprocates at higher frequencies (precisely 3Hz). ζ denotes the intermediate timestamps of the operation of the magnetic field. (b) Zoomed-in view at the contact line region, when the left magnet is active at $\zeta = 0$. Images are acquired at 20X magnification.

As explained in the previous section, when the magnet is switched ON, the MNPs being magnetic in nature, pierces the bulk fluid of the droplet and rushes towards the active magnet following the XX' line of symmetry (cf. Fig. 6.8(a)). During the motion, the cluster of the MNPs pierces the carrier fluid. This piercing action generates a high-pressure zone ahead of the magnetic nanoparticles, whereas a low-pressure zone is maintained behind the moving MNPs. As a result of this pressure difference in the droplet domain, the bulk fluid motion is generated in the opposite direction to the motion of the moving MNPs. As such, the ferrofluid droplet domain on being perturbed by the magnetic field experiences two typical motions- one shown by the MNPs, while the other is that of the bulk flow. In the previous paragraph, we have observed the movement of the MNPs via bright field visualization technique. The bulk flow motion is quantified by μPIV measurement. Figure 6.9 shows the variation of the velocity vectors of the bulk flow in the droplet domain obtained at different temporal instants of the functioning of the time-dependent electromagnet for (precisely, when f=0.5Hz and 3Hz) at ζ =0, 0.25, 0.5, and 0.75. As already mentioned, $\zeta = t/T_M$, where T_M refers to the time for which a particular electromagnet remains active. It is clearly observed from Fig. 6.9 that as the left magnet is switched ON, the bulk flow rushes towards the right magnet and vice-versa. The direction of the bulk flow motion changes only when the inactive magnet returns to its active phase (equivalently, the direction of the bulk flow motion remains constant throughout the operation of a particular magnet). To mention $\zeta = 0$ denotes the state when the magnet is just switched ON, while, $\zeta = 0.5$, and $\zeta = 0.75$ signifies the subsequent intermediate stages. Note that $\zeta = 0$ is the stage when the nanoparticles realize the magnetic force and start to rearrange themselves along the direction of the applied force. Primarily due to this rearrangement, the low magnitude of velocity is initiated in the droplet flow field. At $\zeta = 0.25$ the MNPs move towards the magnetically active zone with its peak velocity. While at $\zeta = 0.5$ and $\zeta = 0.75$ a spontaneous drop in the flow velocities can be seen for all the case barring $f = 3Hz$ case. In Fig. 6.10, we show the strength of the flow velocity being developed inside the droplet for all the investigating cases. The strength of the velocity is calculated by the root mean square (U) of all the velocity vectors along the X-Y plane

$$U = \frac{1}{N \times M} \sum_{i=1,j=1}^{N,M} \sqrt{u(i,j)^2 + v(i,j)^2} \tag{6.1}$$

Where N and M represent the number of grid points in X and Y direction, respectively. The depicted figure (Fig. 6.10) reiterates the already stated fact that, when the magnet is switched ON, the bulk flow velocity increases, and on reaching its peak value, a decrease in the velocity

of the bulk flow takes place. Note that the decline in velocity takes place for f=0.5 Hz and f=1 Hz case only. However, for the f=3 Hz case, no considerable decrease in velocity is observed. This typical behavior of the droplet flow field can be perceived once we delve deep into the role of the involved timescales in the droplet flow domain, namely the advective timescale $t_u = D_h/U_p$, the perturbation time scale $t_m = 1/2f$ and the diffusion time scale $t_v = D_h^2/\vartheta$. The advective timescale refers to the timescale of motion of the MNPs towards the magnet. The perturbation time scale refers to the time period for which an individual magnet perturbs the droplet flow domain. While the diffusion time scale exists due to the effective viscosity of the bulk flow. The diffusion time scale is the same for all the investigating cases and is around 4s, while the advective timescale (t_u) is of the order of ~ 0.4 s. The perturbation time scale is 1s, 0.5 s, and 0.16 s for 0.5 Hz, 1 Hz, and 3 Hz cases, respectively. Since the diffusion time scale is larger than the other two time scales, the overall dynamics of the droplet flow field are governed by the balance between the perturbation and advective time scales.

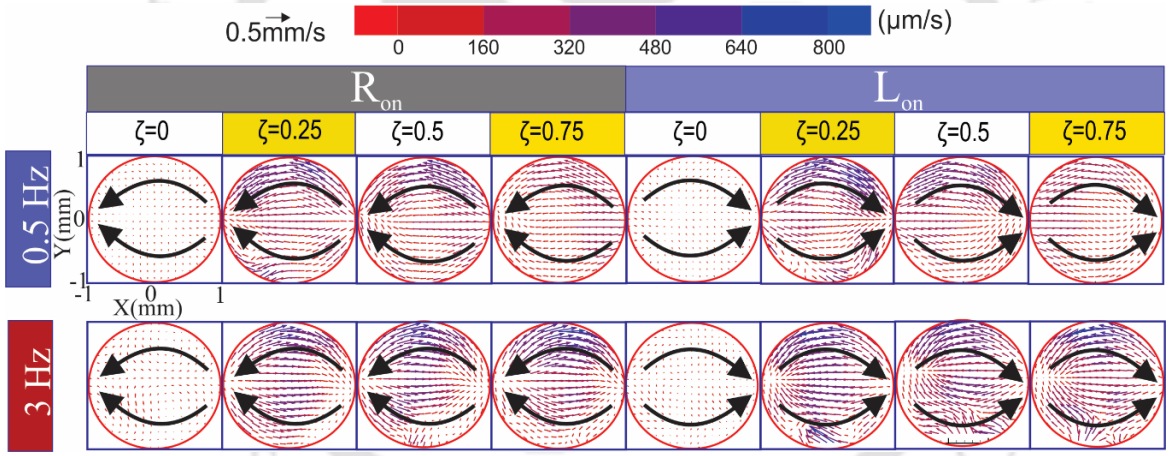

Fig. 6.9 Temporal evolution of the instantaneous velocity vectors inside the droplet flow field obtained at various times of operation of the electromagnet. The frequencies of the magnetic field are maintained between f=0.5 Hz and 3 Hz, respectively. The total time of operation of an individual magnet is divided into four parts, with each individual time-steps denoting an increment of $T_M/4$, where 'T_M' represents the time of operation of an individual magnet, i.e. $T_M = 1/2f$. The flow field is observed at $50\ \mu m$ from the substrate. Black colored arrows indicate the motion of the bulk flow.

As already observed from the preceding paragraphs that whenever the magnet is switched ON, the MNPs migrates towards the active magnet and, in turn, creates disturbances in the bulk flow. Furthermore, when the moving MNPs impact the contact line nearby the active magnet, a large disturbance is created in the bulk flow, resulting in its peak velocity. However, after impacting the contact line, the MNPs starts arranging itself in a chain-like cluster formation under the influence of the applied magnetic field. As a consequence, the viscous forces of the liquid dampens out the created disturbances. Primarily, for this reason,

we find a reduction in the overall velocity for 0.5 Hz and 1 Hz case once the peak velocities are reached. To mention, specific for these frequencies, advective timescale (t_u) is comparable with perturbation timescale (t_m). Needleless to mention here that the decrease in velocity is more for 0.5 Hz case as compared to the 1 Hz case since the advective time scale almost balances the perturbation time scale for the 1 Hz case. However, for the 3 Hz case, the perturbation time scale (t_m) is very small when compared to the advective time scale. Primarily due to this fact, the MNPs for this particular case (f=3 Hz) always stay in a mobile state. As such, the viscous force of the liquid is always less in comparison to the advective force of the MNPs. Thus, no decay in velocity is encountered for this case as witnessed in Fig. 6.10.

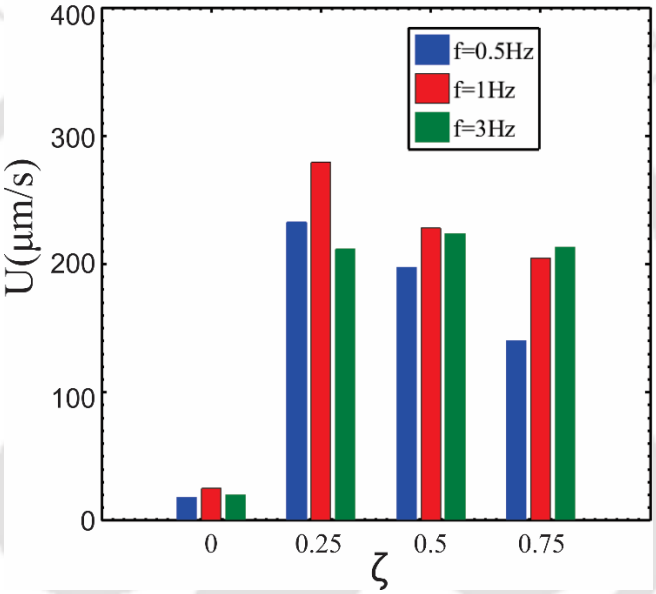

Fig. 6.10 Plot illustrates the variation of the strength of the velocity (U) inside the droplet domain at various time instant of operation of the magnetic field. 'T_M' represents the time of operation of each individual magnet. Note that ζ represents the temporal instant of the functioning magnetic field.

6.3.3 Internal dynamics of the evaporating droplet

In this section, we explore the internal dynamics of the droplet domain throughout its evaporation process. Here the flow field of the droplet is represented at various temporal instants of its life-time (precisely $t^* = 0, t^* = 0.25, t^* = 0.5, t^* = 0.75$). In Fig. 6.11(a), we show the velocity vectors inside the droplet domain for all the investigating cases. In the absence of a magnetic field, the fluid flow inside the droplet domain is directed inward. While, in the presence of the magnetic field, the fluid is directed away from the active magnet as already mentioned in the preceding section (cf. Fig. 6.11(b), for the direction of the bulk flow, where a schematic representation of the bulk flow motion is shown). The inward flow motion signifies an upwards plume type flow, which is in stark contrast to the capillary flow, as was

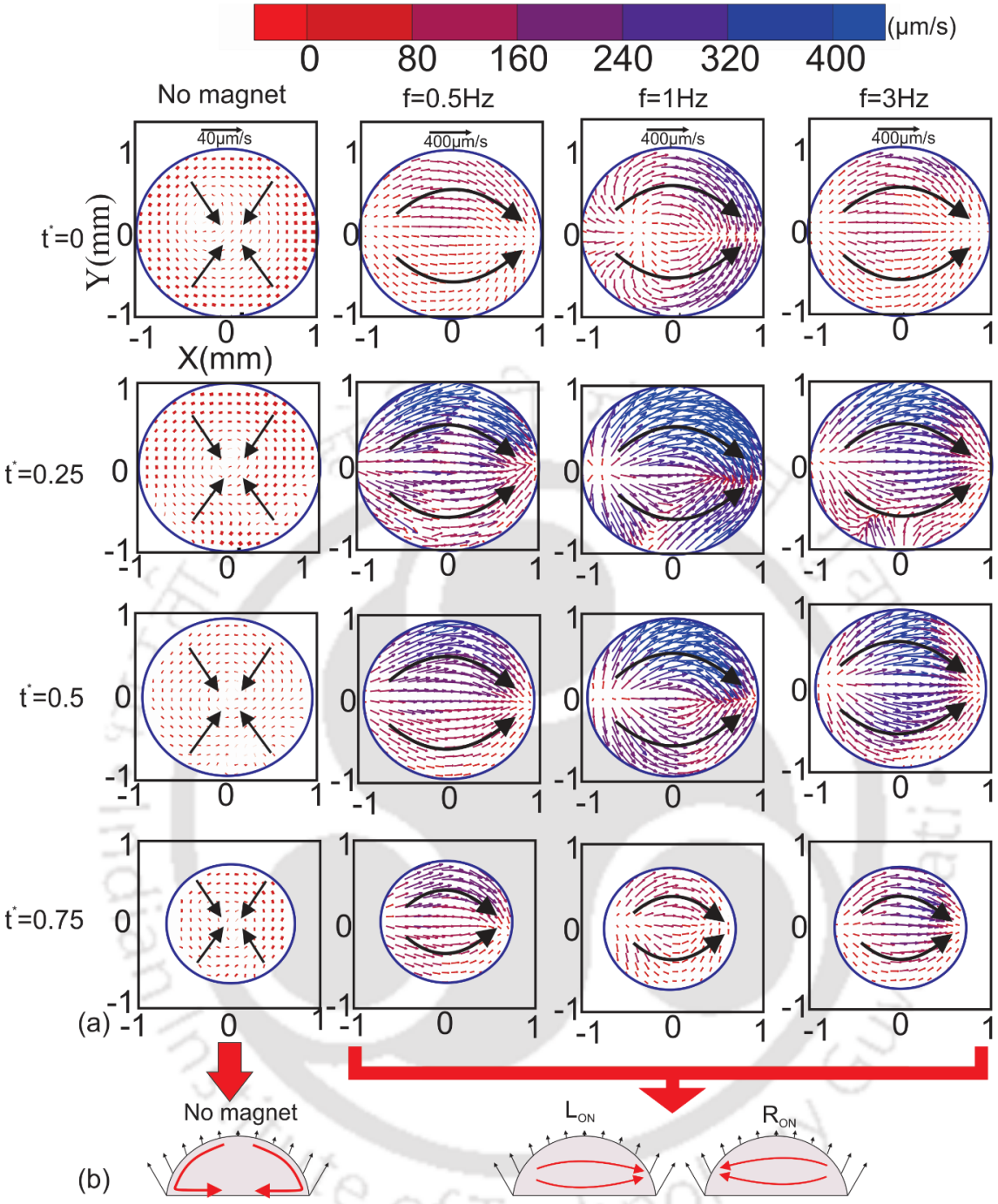

Fig. 6.11 (a) Velocity vectors inside the droplet at various times of the evaporation process, when the frequencies of the magnetic field are maintained between f=0.5 Hz, 1 Hz, and 3 Hz. The plot depicts the droplet domain only when the left magnet is in ON state. Black colored arrows show the overall direction of the bulk flow. The total time of evaporation of the individual droplet is divided into 4-time steps with each time steps representing an increment of $T_E/4$, where T_E is the total time of evaporation of an individual droplet. (b) Schematic illustrates the bulk flow motion inside the droplet during its evaporation process, both in the absence and presence of the magnetic field.

suggested by Deegan et al (2000). It may be mentioned here that the non-uniform evaporation induces a temperature gradient in the droplet flow field, and resulting in a Marangoni convection in the bulk flow (Ristenpart et al. 2007). The motion of the bulk flow depends on the ratio of the thermal conductivities of the substrate (k_s) and the fluid (k_f). It is worth

adding here that, for $k_s/k_f < 1.45$, the Marangoni convection dominates the evaporation process. In the present investigation $k_s/k_f = 0.5$, and primarily due to this value of k_s/k_f, an inward-directed flow is encountered in the droplet domain. However, a different perspective can be obtained when the magnetic field perturbs the droplet, as can be observed from Fig. 6.11(a). Note that $t^* = 0$ denotes the state when the magnet is just switched ON, and a very low velocity is encountered here. For $t^* = 0.25$, the peak velocities are encountered while at $t^* = 0.5$, and $t^* = 0.75$ a decreases in velocities can be seen for all the frequencies.

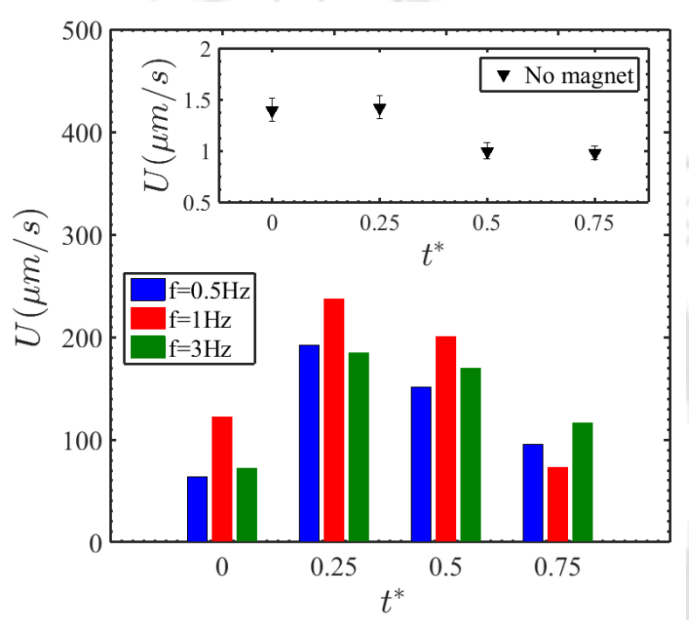

Fig. 6.12 Plot illustrates the variation of the strength of the velocity of the droplet domain at various time instant of the evaporation process. The total time of evaporation of the individual droplet is divided into four time-steps with each individual time-steps representing an increment of $T_E/4$, where T_E is the total time of evaporation of an individual droplet. The velocity shown is the area-averaged mean velocity of the bulk flow inside the droplet domain. The inset shows the mean velocity variation in the droplet domain in the absence of a magnetic field.

Figure 6.12 depicts the variation of the strength of the bulk flow velocity (U) inside the droplet domain for cases under consideration. The inset shows the velocity variation when no magnetic field perturbs the domain. As can be seen from Fig. 6.12 the bulk flow velocity in the droplet domain under the influence of the magnetic field becomes two orders higher than that of the no magnet case (precisely the "base" case). Also, in accordance with the previous discussion, we can see that the mean bulk flow velocity reaches its peak value at $t^* = 0.25$, after which a clear decrease is observed for $t^* = 0.5$, and $t^* = 0.75$. We attribute the initial increase in bulk flow velocity to an increase in the volume fraction of the MNPs. With the evaporation of the liquid carrier phase, the volume fraction of the MNPs in the fluid increases. This increased volume fraction of the MNPs ensures substantial disturbances in the

bulk fluid domain (when placed under the magnetic field). However, with further evaporation, as the receding contact angle of the droplet is reached, the contact line gets depinned, and it recedes. This receding of the contact line ensures that the distance between the triple contact line and the magnet increases. Notably, this increase in the distance reduces the amount of disturbances created on the bulk flow, thereby reducing its velocity. In addition to that, at a higher volume fraction of nanoparticles, the resistance offered by the substrate wall to the flow becomes significant. It is mainly because of these two reasons; we see a decrease in the mean velocity for $t^* = 0.5$ and $t^* = 0.75$ in Fig. (6.11)-(6.12).

6.3.4 Contact line dynamics of the evaporating droplet

In one of the preceding sections, we have shown that the ferrofluid droplet under the influence of two time-dependent electromagnets evaporates in three stages mainly: the DCVR mode, the DCDR mode, and the late mixed mode. These stages ensure dissimilarity in the motion of the contact line. Accordingly, we here attempt to calculate the triple contact line velocity as given by:

$$U_{cl} = \frac{D(t) - D(0)}{\Delta t} \tag{6.2}$$

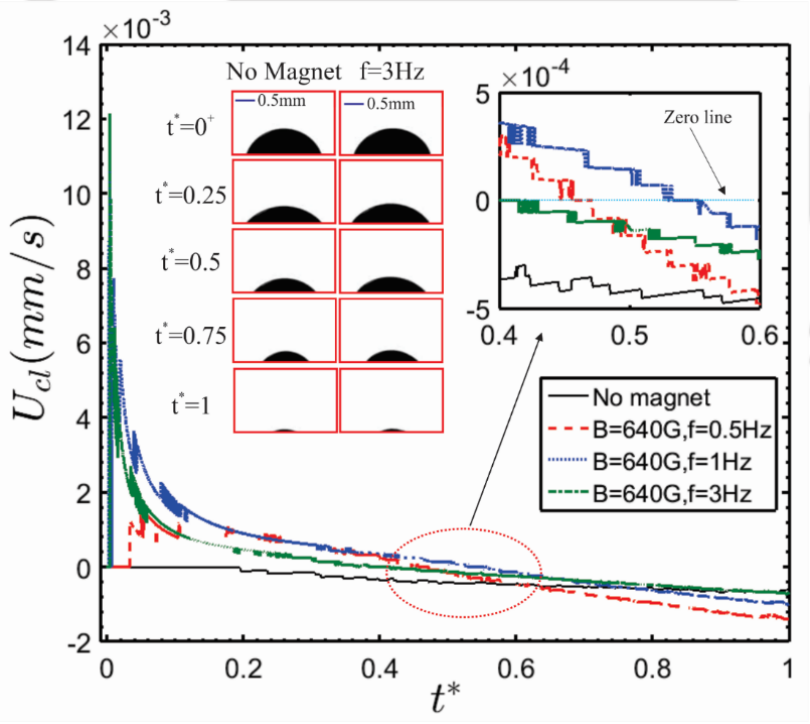

Fig. 6.13 Plot depicts the temporal evolution of the velocity of the contact line under the influence of the magnetic field, when the frequency varies from f=0.5 Hz, f=1 Hz, and f=3 Hz, respectively. The magnetic field flux density is kept constant at $\bar{B} = 640\ G$. The inset on the left-hand side shows the snapshots of the evaporating droplet for "no magnet" and f=3 Hz case. The inset on the right-hand side shows the zoomed view of the area under the red colour dotted ellipse. The dotted light blue straight line indicates the zero line.

Figure 6.13 shows the temporal variation of the velocity of the triple contact line (U_{cl}). Note that in the absence of a magnetic field, the triple contact line remains pinned until 20% of the total evaporation time. Due to this extended pinning, the mean velocity of the triple contact line remains almost zero. However, under the influence of the time-periodic magnetic field, the diameter of the droplet increases at the earlier temporal instant, leading to the positive velocity of the triple contact line. To mention, the initial rise in the triple contact line velocity is directly dependent on the frequency of the magnetic field. The maximum initial velocity is encountered when the frequency of the magnetic field is maintained at f=3 Hz, while the rise in velocity is minimum when f=0.5 Hz. Therefore, it can be concluded that the spontaneity of the perturbation process dominates the initial increase in the triple contact line velocity. The zero line in the inset of Fig. 6.13 indicates the point where the instantaneous diameter of the droplet is equal to the initial diameter of the droplet. Therefore, the temporal instant at which the U_{cl} intersect the zero line can be taken as the time till which the droplet undergoes evaporation in the DCVR mode. In the present investigation, the DCVR zone duration is about 47%, 53 %, and around 45% for f=0.5 Hz, f=1 Hz, and f=3 Hz cases, respectively. The increased period of the DCVR zone ensures a high triple contact line area, thereby making sure of the fast evaporation of the droplet.

6.3.5 Mechanism of evaporation

Although it is established by now that the decrease in the droplet life-time is due to the increase in the effective evaporative surface area, specifically the triple contact line area, we here make an effort to figure out the underlying issues in greater detail. As such, we would like to address an important question in this context, i.e., *why the duration of DCVR zone is more for the f=1 Hz compared to the other two cases, i.e., f=0.5 Hz and f=3 Hz*? To mention, the problem at hand is a time-dependent problem. Thus, the intricate physics can only be understood once we exploit the role of the individual times scales involved with the underlying phenomena. We have seen in the bright field visualization section that on the actuation of the magnetic field, the MNPs migrate towards the magnet and arrange themselves in a chain-like cluster formation. The impact of this chain-like cluster formation is responsible for the movement of the triple contact line towards the magnet. This phenomenon eventually increases the triple contact line area. Pertaining to the 1 Hz case, where the advective time scale is balanced by the perturbation time scale, the receding of the triple contact line is delayed to the maximum possible extent. For this particular case, it may be the situation that even if the receding contact angle of a liquid-air interface is reached, the MNPs arrive there

(the liquid-air interface) beforehand (Since, $t_U \sim t_M$) and derails the receding of the triple contact line. This prevention of the receding motion of the contact line, in turn, extends the duration of the DCVR zone for this particular case (When f=1 Hz). However, for the 0.5 Hz case (Where, $t_U < t_M$), the MNPs move towards the magnet and reside there for 1 s, and during this time interval (1 s), the other contact line starts receding when the receding contact angle of the droplet is reached (since the surface tension force will always try to recede the contact line). For the 3 Hz case, however, the MNPs do not possess sufficient time to reach at both the contact line effectively, since the perturbation time scale is very small as compared to the pertinent advective time scale. It is because of this reason we encounter the least duration for the DCVR for the 3 Hz case.

6.4 SUMMARY

In the present study, we have demonstrated that the evaporation time of the ferrofluid droplet can be effectively reduced in a controlled manner using the time-dependent magnetic field. To understand the internal hydrodynamic features qualitatively, we have conducted a bright field visualization of the droplet domain, while the μPIV analysis has been carried out for the quantitative description of the underlying hydrodynamics. To summarize, we have observed distinct evaporation characteristics of the ferrofluid droplet under the perturbation of the magnetic field. We have unveiled that the magnetic field induced forcing alters the droplet evaporation mechanism non-trivially as realized by the presence of the new modes of evaporation *viz*., the DCVR, DCDR, and late mixed stage. We have graphically shown these new modes of evaporation and aptly demonstrated the flow physics involved with the underlying kinetics. In the DCVR zone, which is the first as well as the crucial mode of evaporation in the present scenario, although the temporal variation of the droplet height and the contact angle decreases (shows similarity with the CCR mode of the unperturbed case), the diameter of the droplet shows a rise and fall pattern. Under the influence of the magnetic field, the contact line gets stretched (de-pinning), thereby increasing the triple contact line area. This increased contact line area enhances the evaporation rate and results in a reduction in the overall life-time of the droplet. Also, we have identified a critical frequency of the applied magnetic field strength for which the droplet encounters a minimum life-time. At the critical frequency, the advective time scale of the magnetic nanoparticles gets balanced by the perturbation time scale of the magnetic field. This balance of time scale is suggestive of the optimum motion of the MNPs between the two magnetically active zones (precisely the contact line regions). As such, this optimal motion of MNPs prevents the receding of the

contact line to the maximum extent (beyond a point, the de-pinning forces dominate the perturbation force, and the contact line recedes), leading to an escalation of the DCVR mode of evaporation. We believe that the inferences of the present analysis, which provide an effective way for the controllability in the droplet evaporation kinetics by tuning the motion of the MNPs, may be crucial to a host of applications requiring a greater degree of control in the life-time of a droplet.

Chapter 7

CONCLUSION AND SCOPE FOR FURTHER WORK

In this final chapter, the important conclusions drawn from the studies executed as a part of this Thesis are summarized. This is followed by discussions on the application potential of the study and the possible further extensions of the present work.

7.1 SUMMARY AND OUTLOOK

In order to support the rapid growth of ferrofluid-based applications, fundamental insights are required to discern the physics governing the ferrofluid transport phenomena in the presence of a magnetic field. The present thesis addresses some fundamental issues related to the transport process of ferrofluid flow under the modulation of a magnetic field. In the purview of this general theme, the major topics that are addressed in the present dissertation as follows:

- Thermohydrodynamics of the ferrofluid flow in a heated channel in the presence of a steady and time-varying magnetic field.
- Effect of frequency of the time-dependent magnetic field on the internal hydrodynamics of a sessile ferrofluid droplet.
- Mixing of a sessile ferrofluid droplet with another non-magnetic droplet in a time-dependent magnetic forcing environment.
- Evaporation characteristics of a sessile ferrofluid droplet in a magnetic field driven environment.

The concluding remarks are categorized into the four above mentioned major topics, and the key findings of the present investigation are summarized in the subsequent subsections.

7.1.1 Thermohydrodynamics of ferrofluid in the presence of magnetic field

The convective heat transfer characteristics of ferrofluid flow in a heated stainless steel tube in the presence of both steady and time-dependent magnetic fields are explored via experimental and numerical investigations. Infrared thermography is carried out for quantification of the thermal characteristics of the flow field, while the bright field visualization technique is employed for a qualitative understanding of the hydrodynamic

features of the ferrofluid flow. Numerical simulations are conducted to gain insights into the ferrofluid flow's intricate dynamics in the magnetic field's presence. The governing equations for the problem considered in the present study are the continuity, momentum, energy, and Maxwell equations. Augmentation in the thermal characteristics of the ferrofluid flow in the presence of a steady magnet is observed (around 23 % when compared to the base case, i.e., no applied magnetic field). It has been clearly illustrated that a hump-like structure develops in the magnetically active zone on the actuation of the steady electromagnet. Due to the development of hump-like structure, a recirculation zone is primarily created at the immediate downstream location, leading to the development of secondary flow. It has also been shown that when a time-dependent magnetic field perturbs the ferrofluid domain, substantial enhancement in the thermal characteristics of the flow field occurs (around 39 % compared to the base case). On the application of a time-dependent magnetic field, the heat transfer augmentation process is governed by the balance between the dominant time scales, mainly the advective and perturbation time scales. The study finally establishes the mechanism of augmentation in heat transfer as follows: (a) formation of the hump with irregular spikes on the surface because of clustering of MNPs (b) chain-like clustering of the dispersed MNPs in the bulk fluid, (c) imbalance of the resultant forces and couples in the flow field due to the interaction of inertia and magnetic forces.

7.1.2 Internal hydrodynamics of ferrofluid under the modulations of a magnetic field

A systematic experimental investigation is carried out to explore the internal hydrodynamics of a sessile ferrofluid droplet in the presence of a time-dependent magnetic field. The motion of the magnetic nanoparticles is observed by the bright field visualization, whereas the μ-PIV measurement technique is used for quantification of the bulk liquid flow. The primary focus of the study has been to assess the role of frequency of the magnetic field on the hydrodynamics (such as velocity, vorticity) inside the ferrofluid droplet. It has been clearly illustrated that on the actuation of an electromagnet, the magnetic nanoparticles migrate towards the direction of the applied magnetic field, which in turn, generates internal convection inside the ferrofluid droplet. Alterations of the flow field velocity, in effect, is achieved by careful maneuvering of the applied frequency of the magnetic field. The presence of a critical frequency ($f = 0.5\,Hz$) is observed beyond which negligible dispersion of the magnetic nanoparticles at the magnetically active zone takes place. The negligible dispersion of nanoparticles at critical frequency leads to the development of stagnant layers of nanoparticles near the contact line. This phenomena may have an impact on the study of

separation of cells or proteins using various markers/antibodies, tagged with magnetic nanoparticles.

7.1.3 Mixing characteristics of the ferrofluid droplet in a magnetic field-driven environment

The mixing characteristics of a sessile ferrofluid droplet with a non-magnetic droplet under the modulation of a time-dependent magnetic field are thoroughly explored. Bright field visualization and μPIV measurement technique are used for qualitative and quantitative understanding of the flow parameters. The μLIF measurement technique is employed for quantification of the underlying mixing phenomena between the two fluids. Enhancement in the flow convections inside the ferrofluid droplet is observed in the presence of a time-dependent magnetic field. In addition, flow instabilities also get triggered due to the susceptibility mismatch between the two fluids. Numerical simulations are conducted for the understanding of the initiation of instability inside the droplet. The results revealed that the enhanced flow convections on getting coupled with the flow instabilities substantially reduce the mixing time between the two fluid droplets. A critical frequency of the applied magnetic field is observed at which the droplets exhibit minimum mixing time (around 80% less time compared to the base case, i.e., when no magnetic field is applied). The critical frequency is the resultant effect of the advective and perturbation timescales. The results of this study demonstrate an efficient way of mixing between two droplets. The proposed study may find relevance in numerous biomicrofluidic and Lab-on-a-CD based applications where fast mixing between reagents are required.

7.1.4 Evaporation kinetics of the ferrofluid droplet as modulated by the magnetic field

The implications of the transient motion of magnetic nanoparticles in the presence of a time-varying magnetic field on the evaporation dynamics of the sessile ferrofluid droplet is investigated experimentally. The time-dependent motion of the magnetic nanoparticles inside the ferrofluid droplet non-trivially maneuvers the pinning/depinning dynamics of the triple contact line, which in turn enhances the evaporative mass transfer. The overall lifetime of the droplet is significantly reduced under the influence of a time-dependent magnetic field. On perturbation by a time-dependent magnetic field, the lifetime of the ferrofluid droplet reduces drastically and becomes almost halves, compared to the base case, i.e., no applied magnetic field. Results demonstrate the presence of new modes of evaporation *viz.*, the decreasing contact angle and varying radius mode (DCVR), the decreasing contact angle and decreasing

radius mode (DCDR), and the late mixed mode. Under the influence of the magnetic field, the contact line gets stretched (de-pinning), thereby increasing the triple contact line area. This increased contact line area enhances the evaporation rate and reduces the overall lifetime of the droplet. The presence of a threshold frequency is observed at which the ferrofluid droplet exhibits a minimum lifetime. The inferences drawn from the present analysis may provide an effective way for the controllability of the droplet's overall lifetime.

7.2 APPLICATION POTENTIAL OF THE STUDY

The inferences drawn from the present thesis can be extrapolated in many real-time engineering applications such as electronic cooling, mixing of fluids, evaporation of droplets, and many more. While designing an electronic cooling mechanism, ferrofluid may be used under the modulation of the time-varying magnetic field for achieving effective heat transfer. Similarly, mixing between fluids, which predominantly occurs via molecular diffusion, can be substantially augmented under a magnetic field driven environment. This is of particular importance to biological sampling applications where rapid and efficient mixing is of prime significance. Also, the evaporation kinetics of the ferrofluid droplet is substantially enhanced in a magnetic field ambiance. The transient motion of the magnetic nanoparticles under modulation of a time-dependent magnetic field alters the pinning and depinning dynamics of the triple contact line, thereby amending the droplet's evaporation kinetics considerably. This inference may be of critical importance to applications requiring controlled evaporation dynamics and deposition patterns, for example, printing industries.

7.3 SCOPE FOR FURTHER WORK

In the present study, the transport phenomena of ferrofluid in the presence of a magnetic field are explored both experimentally and numerically. More analysis is required to explore the suitability of ferrofluid in a variety of microfluidic related applications. The following are the recommendations for future investigations:

- In this study, during the numerical investigations, ferrofluid is treated as a single-phase fluid. To have a detailed understanding of the orientation and arrangement of the magnetic nanoparticles in the presence of a magnetic field, ferrofluid must be treated as a two-phase fluid, i.e., comprising of solid nanoparticles and liquid carrier phase.

- The deposition pattern of the ferrofluid droplet in the presence of a time-dependent magnetic field can be explored. The transient motion of the magnetic nanoparticles may suppress the formation of a coffee ring pattern.
- In this study, the evaporation of the ferrofluid droplet in the presence of two alternatively working electromagnet is explored. The morphological evolution of the droplet in the presence of a rotating magnetic field may be an interesting problem. In the presence of a rotating magnetic field, the magnetic nanoparticles will form closed linked chains that may non-trivially affect the contact line's pinning/depinning dynamics.

References

Ahmed A, Fleck BA, Waghmare PR (2018a) Maximum spreading of a ferrofluid droplet under the effect of magnetic field. Physics of Fluids 30:077102. https://doi.org/10.1063/1.5032113

Ahmed A, Qureshi AJ, Fleck BA, Waghmare PR (2018b) Effects of magnetic field on the spreading dynamics of an impinging ferrofluid droplet. Journal of Colloid and Interface Science 532:309–320. https://doi.org/10.1016/j.jcis.2018.07.110

Ahuja AS (1975) Augmentation of heat transport in laminar flow of polystyrene suspensions. II. Analysis of the data. Journal of Applied Physics 46:3417–3425. https://doi.org/10.1063/1.322062

Aminfar H, Mohammadpourfard M, Ahangar Zonouzi S (2013) Numerical study of the ferrofluid flow and heat transfer through a rectangular duct in the presence of a non-uniform transverse magnetic field. Journal of Magnetism and Magnetic Materials 327:31–42. https://doi.org/10.1016/j.jmmm.2012.09.011

Andrade A, Ferreira R, Fabris J, Domingues R (2011) Coating Nanomagnetic Particles for Biomedical Applications. In: Biomedical Engineering - Frontiers and Challenges. InTech

Anoop K, Sadr R (2012) nPIV velocity measurement of nanofluids in the near-wall region of a microchannel. Nanoscale Research Letters 7:284. https://doi.org/10.1186/1556-276X-7-284

Asfer M, Mehta B, Kumar A, et al (2016) Effect of magnetic field on laminar convective heat transfer characteristics of ferrofluid flowing through a circular stainless steel tube. International Journal of Heat and Fluid Flow 59:74–86. https://doi.org/10.1016/j.ijheatfluidflow.2016.01.009

Azizian R, Doroodchi E, Mckrell T, et al (2014) Effect of magnetic field on laminar convective heat transfer of magnetite nanofluids. International Journal of Heat and Mass Transfer 68:94–109. https://doi.org/10.1016/j.ijheatmasstransfer.2013.09.011

Bau HH, Zhong J, Yi M (2001) A minute magneto hydro dynamic (MHD) mixer. Sensors and Actuators, B: Chemical 79:207–215. https://doi.org/10.1016/S0925-4005(01)00851-6

Berry SM, Alarid ET, Beebe DJ (2011) One-step purification of nucleic acid for gene expression analysis via Immiscible Filtration Assisted by Surface Tension (IFAST). Lab on a Chip 11:1747. https://doi.org/10.1039/c1lc00004g

Beyzavi A, Nguyen N-T (2009) One-dimensional actuation of a ferrofluid droplet by planar microcoils. Journal of Physics D: Applied Physics 42:015004. https://doi.org/10.1088/0022-3727/42/1/015004

Biswal SL, Gast AP (2004) Micromixing with Linked Chains of Paramagnetic Particles. Analytical Chemistry 76:6448–6455. https://doi.org/10.1021/ac0494580

Bogojevic D, Chamberlain MD, Barbulovic-Nad I, Wheeler AR (2012) A digital microfluidic method for multiplexed cell-based apoptosis assays. Lab on a Chip 12:627–634. https://doi.org/10.1039/C2LC20893H

Brinkman HC (1952) The Viscosity of Concentrated Suspensions and Solutions. The Journal of Chemical Physics 20:571–571. https://doi.org/10.1063/1.1700493

Brutin D, Sobac B, Loquet B, Sampol J (2011) Pattern formation in drying drops of blood. Journal of Fluid Mechanics 667:85–95. https://doi.org/10.1017/S0022112010005070

Černák J, Helgesen G, Skjeltorp AT (2004) Aggregation dynamics of nonmagnetic particles in a ferrofluid. Physical Review E 70:031504. https://doi.org/10.1103/PhysRevE.70.031504

Chauvet F, Cazin S, Duru P, Prat M (2010) Use of infrared thermography for the study of evaporation in a square capillary tube. International Journal of Heat and Mass Transfer 53:1808–1818. https://doi.org/10.1016/j.ijheatmasstransfer.2010.01.008

Cheung YN, Qiu H (2011) Characterization of acoustic droplet formation in a microfluidic flow-focusing device. Physical Review E 84:066310. https://doi.org/10.1103/PhysRevE.84.066310

Chon CH, Paik S, Tipton JB, Kihm KD (2007) Effect of Nanoparticle Sizes and Number Densities on the Evaporation and Dryout Characteristics for Strongly Pinned Nanofluid Droplets. Langmuir 23:2953–2960. https://doi.org/10.1021/la061661y

Churchill SW, Ozoe H (1973) Correlations for Laminar Forced Convection with Uniform Heating in Flow over a Plate and in Developing and Fully Developed Flow in a Tube. Journal of Heat Transfer 95:78–84. https://doi.org/10.1115/1.3450009

Das S, Dey A, Reddy G, Sarma DD (2017) Suppression of the Coffee-Ring Effect and Evaporation-Driven Disorder to Order Transition in Colloidal Droplets. The Journal of Physical Chemistry Letters 8:4704–4709. https://doi.org/10.1021/acs.jpclett.7b01814

de Groot TE, Veserat KS, Berthier E, et al (2016) Surface-tension driven open microfluidic platform for hanging droplet culture. Lab on a Chip 16:334–344. https://doi.org/10.1039/C5LC01353D

Deegan RD (2000) Pattern formation in drying drops. Physical Review E 61:475–485.

https://doi.org/10.1103/PhysRevE.61.475

Deegan RD, Bakajin O, Dupont TF, et al (2000) Contact line deposits in an evaporating drop. Physical Review E 62:756–765. https://doi.org/10.1103/PhysRevE.62.756

Deegan RD, Bakajin O, Dupont TF, et al (1997) Capillary flow as the cause of ring stains from dried liquid drops. Nature 389:827–829. https://doi.org/10.1038/39827

Dey R, Daga A, DasGupta S, Chakraborty S (2015) Electrically modulated dynamic spreading of drops on soft surfaces. Applied Physics Letters 107:034101. https://doi.org/10.1063/1.4927307

Elfimova EA, Ivanov AO, Camp PJ (2013) Thermodynamics of ferrofluids in applied magnetic fields. Physical Review E 88:042310. https://doi.org/10.1103/PhysRevE.88.042310

Eral HB, Augustine DM, Duits MHG, Mugele F (2011) Suppressing the coffee stain effect: how to control colloidal self-assembly in evaporating drops using electrowetting. Soft Matter 7:4954. https://doi.org/10.1039/c1sm05183k

Erbil HY (2012) Evaporation of pure liquid sessile and spherical suspended drops: A review. Advances in Colloid and Interface Science 170:67–86. https://doi.org/10.1016/j.cis.2011.12.006

Etgar L, Nakhmani A, Tannenbaum A, et al (2010) Trajectory control of PbSe–γ-Fe_2O_3 nanoplatforms under viscous flow and an external magnetic field. Nanotechnology 21:175702. https://doi.org/10.1088/0957-4484/21/17/175702

Ferraro D, Lin Y, Teste B, et al (2015) Continuous chemical operations and modifications on magnetic γ-Fe_2O_3 nanoparticles confined in nanoliter droplets for the assembly of fluorescent and magnetic SiO_2 @γ-Fe_2O_3. Chemical Communications 51:16904–16907. https://doi.org/10.1039/C5CC07044A

Fischer BJ (2002) Particle Convection in an Evaporating Colloidal Droplet. Langmuir 18:60–67. https://doi.org/10.1021/la015518a

Franke T, Schmid L, Weitz DA, Wixforth A (2009) Magneto-mechanical mixing and manipulation of picoliter volumes in vesicles. Lab on a Chip 9:2831. https://doi.org/10.1039/b906569p

Fu LM, Tsai CH, Leong KP, Wen CY (2010) Rapid micromixer via ferrofluids. Physics Procedia 9:270–273. https://doi.org/10.1016/j.phpro.2010.11.060

Ganguly R, Sen S, Puri IK (2004) Heat transfer augmentation using a magnetic fluid under the influence of a line dipole. Journal of Magnetism and Magnetic Materials 271:63–73. https://doi.org/10.1016/j.jmmm.2003.09.015

Gao Y, Beerens J, van Reenen A, et al (2015) Strong vortical flows generated by the collective motion of magnetic particle chains rotating in a fluid cell. Lab on a Chip 15:351–360. https://doi.org/10.1039/C4LC01198H

Gavili A, Zabihi F, Isfahani TD, Sabbaghzadeh J (2012) The thermal conductivity of water base ferrofluids under magnetic field. Experimental Thermal and Fluid Science 41:94–98. https://doi.org/10.1016/j.expthermflusci.2012.03.016

Godson L, Raja B, Mohan Lal D, Wongwises S (2010) Enhancement of heat transfer using nanofluids—An overview. Renewable and Sustainable Energy Reviews 14:629–641. https://doi.org/10.1016/j.rser.2009.10.004

Goharkhah M, Ashjaee M (2014) Effect of an alternating nonuniform magnetic field on ferrofluid flow and heat transfer in a channel. Journal of Magnetism and Magnetic Materials 362:80–89. https://doi.org/10.1016/j.jmmm.2014.03.025

Goharkhah M, Ashjaee M, Jamali J (2015a) Experimental investigation on heat transfer and hydrodynamic behavior of magnetite nanofluid flow in a channel with recognition of the best models for transport properties. Experimental Thermal and Fluid Science 68:582–592

Goharkhah M, Ashjaee M, Shahabadi M (2016) Experimental investigation on convective heat transfer and hydrodynamic characteristics of magnetite nanofluid under the influence of an alternating magnetic field. International Journal of Thermal Sciences 99:113–124. https://doi.org/10.1016/j.ijthermalsci.2015.08.008

Goharkhah M, Salarian A, Ashjaee M, Shahabadi M (2015b) Convective heat transfer characteristics of magnetite nano fluid under the influence of constant and alternating magnetic field. Powder Technology 274:258–267

Griffiths DJ, Inglefield C (2005) Introduction to Electrodynamics. American Journal of Physics 73:574–574. https://doi.org/10.1119/1.4766311

Grillone A, Ciofani G (2017) Magnetic Nanotransducers in Biomedicine. Chemistry - A European Journal 23:16109–16114. https://doi.org/10.1002/chem.201703660

Hejazian M, Li W, Nguyen N-T (2015) Lab on a chip for continuous-flow magnetic cell separation. Lab on a Chip 15:959–970. https://doi.org/10.1039/C4LC01422G

Hejazian M, Phan D-T, Nguyen N-T (2016) Mass transport improvement in microscale using diluted ferrofluid and a non-uniform magnetic field. RSC Advances 6:62439–62444. https://doi.org/10.1039/C6RA11703A

Hernández-Contreras M, Ruíz-Estrada H (2003) Transport properties of ferrofluids. Physical Review E 68:031202. https://doi.org/10.1103/PhysRevE.68.031202

Hiergeist R, Andrä W, Buske N, et al (1999) Application of magnetite ferrofluids for hyperthermia. Journal of Magnetism and Magnetic Materials 201:420–422. https://doi.org/10.1016/S0304-8853(99)00145-6

Hu D, Wu H (2016) Volume evolution of small sessile droplets evaporating in stick-slip mode. Physical Review E 93:042805. https://doi.org/10.1103/PhysRevE.93.042805

Huang G, Li M, Yang Q, et al (2017) Magnetically Actuated Droplet Manipulation and Its Potential Biomedical Applications. ACS Applied Materials & Interfaces 9:1155–1166. https://doi.org/10.1021/acsami.6b09017

Jadav M, Patel RJ, Mehta R V. (2017) Influence of magnetic field on evaporation of a ferrofluid droplet. Journal of Applied Physics 122:145302. https://doi.org/10.1063/1.4990665

Jaiswal V, Dwivedi RK, Harikrishnan AR, Dhar P (2018) Magnetohydrodynamics- and magnetosolutal-transport-mediated evaporation dynamics in paramagnetic pendant droplets under field stimulus. Physical Review E 98:013109. https://doi.org/10.1103/PhysRevE.98.013109

Katsikis G, Cybulski JS, Prakash M (2015) Synchronous universal droplet logic and control. Nature Physics 11:588–596. https://doi.org/10.1038/nphys3341

Kitenbergs G, Erglis K, Perzynski R, Cēbers A (2015) Magnetic particle mixing with magnetic micro-convection for microfluidics. Journal of Magnetism and Magnetic Materials 380:227–230. https://doi.org/10.1016/j.jmmm.2014.10.033

Lajvardi M, Moghimi-Rad J, Hadi I, et al (2010) Experimental investigation for enhanced ferrofluid heat transfer under magnetic field effect. Journal of Magnetism and Magnetic Materials 322:3508–3513. https://doi.org/10.1016/j.jmmm.2010.06.054

Lee SH, van Noort D, Lee JY, et al (2009) Effective mixing in a microfluidic chip using magnetic particles. Lab on a Chip 9:479–482. https://doi.org/10.1039/B814371D

Liang L, Zhang C, Xuan X (2013) Enhanced separation of magnetic and diamagnetic particles in a dilute ferrofluid. Applied Physics Letters 102:234101. https://doi.org/10.1063/1.4810874

Lin D, Li P, Lin J, et al (2017) Orthogonal Screening of Anticancer Drugs Using an Open-Access Microfluidic Tissue Array System. Analytical Chemistry 89:11976–11984. https://doi.org/10.1021/acs.analchem.7b02021

Liu H, Li M, Li Y, et al (2018) Magnetic steering of liquid metal mobiles. Soft Matter 14:3236–3245. https://doi.org/10.1039/c8sm00056e

Long Z, Shetty AM, Solomon MJ, Larson RG (2009) Fundamentals of magnet-actuated

droplet manipulation on an open hydrophobic surface. Lab on a Chip 9:1567. https://doi.org/10.1039/b819818g

Lopes MC, Bonaccurso E (2012) Evaporation control of sessile water drops by soft viscoelastic surfaces. Soft Matter 8:7875. https://doi.org/10.1039/c2sm25958c

Lopes MC, Bonaccurso E (2013) Influence of substrate elasticity on particle deposition patterns from evaporating water–silica suspension droplets. Soft Matter 9:7942. https://doi.org/10.1039/c3sm51184g

Lubbers LA, Weijs JH, Botto L, et al (2014) Drops on soft solids: free energy and double transition of contact angles. Journal of Fluid Mechanics 747:R1. https://doi.org/10.1017/jfm.2014.152

Maleki MA, Soltani M, Kashaninejad N, Nguyen N-T (2019) Effects of magnetic nanoparticles on mixing in droplet-based microfluidics. Physics of Fluids 31:032001. https://doi.org/10.1063/1.5086867

Mampallil D, Eral HB, van den Ende D, Mugele F (2012) Control of evaporating complex fluids through electrowetting. Soft Matter 8:10614. https://doi.org/10.1039/c2sm26103k

Manukyan S, Schneider M (2016) Experimental Investigation of Wetting with Magnetic Fluids. Langmuir 32:5135–5140. https://doi.org/10.1021/acs.langmuir.5b04737

Marchand A, Das S, Snoeijer JH, Andreotti B (2012) Contact Angles on a Soft Solid: From Young's Law to Neumann's Law. Physical Review Letters 109:236101. https://doi.org/10.1103/PhysRevLett.109.236101

Martin JE, Shea-Rohwer L, Solis KJ (2009) Strong intrinsic mixing in vortex magnetic fields. Physical Review E 80:016312. https://doi.org/10.1103/PhysRevE.80.016312

Mary P, Studer V, Tabeling P (2008) Microfluidic Droplet-Based Liquid−Liquid Extraction. Analytical Chemistry 80:2680–2687. https://doi.org/10.1021/ac800088s

Mendelev VS, Ivanov AO (2004) Ferrofluid aggregation in chains under the influence of a magnetic field. Physical Review E 70:051502. https://doi.org/10.1103/PhysRevE.70.051502

Moffat JR, Sefiane K, Shanahan MER (2009) Effect of TiO_2 Nanoparticles on Contact Line Stick−Slip Behavior of Volatile Drops. The Journal of Physical Chemistry B 113:8860–8866. https://doi.org/10.1021/jp902062z

Moffat RJ (1988) Describing the uncertainties in experimental results. Experimental Thermal and Fluid Science 1:3–17. https://doi.org/10.1016/0894-1777(88)90043-X

Müller HW, Liu M (2001) Structure of ferrofluid dynamics. Physical Review E 64:061405. https://doi.org/10.1103/PhysRevE.64.061405

Munaz A, Kamble H, Shiddiky MJA, Nguyen N-T (2017) Magnetofluidic micromixer based on a complex rotating magnetic field. RSC Advances 7:52465–52474. https://doi.org/10.1039/C7RA08073E

Murray MM (2008) Demonstration of Heat Transfer Enhancement Using Ferromagnetic Particle Laden Fluid and Switched Magnetic Fields. Journal of Heat Transfer 130:. https://doi.org/10.1115/1.2970064

Nakatsuka K, Jeyadevan B, Neveu S, Koganezawa H (2002) The magnetic fluid for heat transfer applications. Journal of Magnetism and Magnetic Materials 252:360–362. https://doi.org/10.1016/S0304-8853(02)00683-2

Neuringer JL, Rosensweig RE (1964) Ferrohydrodynamics. Physics of Fluids 7:1927. https://doi.org/10.1063/1.1711103

Nguyen N-T (2012) Micro-magnetofluidics: interactions between magnetism and fluid flow on the microscale. Microfluidics and Nanofluidics 12:1–16. https://doi.org/10.1007/s10404-011-0903-5

Nguyen NT, Wu ZG, Huang XY, Wen C-Y (2005) The application of μPIV technique in the study of magnetic flows in a micro-channel. Journal of Magnetism and Magnetic Materials 289:396–398. https://doi.org/10.1016/j.jmmm.2004.11.112

Nguyen TAH, Nguyen A V. (2014) Transient Volume of Evaporating Sessile Droplets: 2/3, 1/1, or Another Power Law? Langmuir 30:6544–6547. https://doi.org/10.1021/la4047287

Nguyen TAH, Nguyen A V. (2012) On the Lifetime of Evaporating Sessile Droplets. Langmuir 28:1924–1930. https://doi.org/10.1021/la2036955

Nkurikiyimfura I, Wang Y, Pan Z (2013) Heat transfer enhancement by magnetic nanofluids—A review. Renewable and Sustainable Energy Reviews 21:548–561. https://doi.org/10.1016/j.rser.2012.12.039

Nouri D, Zabihi-Hesari A, Passandideh-Fard M (2017) Rapid mixing in micromixers using magnetic field. Sensors and Actuators A: Physical 255:79–86. https://doi.org/10.1016/j.sna.2017.01.005

Oddy MH, Santiago JG, Mikkelsen JC (2001) Electrokinetic instability micromixing. Analytical Chemistry 73:5822–5832. https://doi.org/10.1021/ac0155411

Odenbach S (ed) (2002) Ferrofluids. Springer Berlin Heidelberg, Berlin, Heidelberg

Orejon D, Sefiane K, Shanahan MER (2011) Stick–Slip of Evaporating Droplets: Substrate Hydrophobicity and Nanoparticle Concentration. Langmuir 27:12834–12843. https://doi.org/10.1021/la2026736

Pak BC, Cho YI (1998) Hydrodynamic and heat transfer study of dispersed fluids with submicron metallic oxide particles. Experimental Heat Transfer 11:151–170. https://doi.org/10.1080/08916159808946559

Parekh K, Lee HS (2010) Magnetic field induced enhancement in thermal conductivity of magnetite nanofluid. Journal of Applied Physics 107:09A310. https://doi.org/10.1063/1.3348387

Philip J, Shima PD, Raj B (2007) Enhancement of thermal conductivity in magnetite based nanofluid due to chainlike structures. Applied Physics Letters 91:203108. https://doi.org/10.1063/1.2812699

Philip J, Shima PD, Raj B (2008) Nanofluid with tunable thermal properties. Applied Physics Letters 92:043108. https://doi.org/10.1063/1.2838304

Pitzer KS, Peiper JC, Busey RH (1984) Thermodynamic Properties of Aqueous Sodium Chloride Solutions. Journal of Physical and Chemical Reference Data 13:1–102. https://doi.org/10.1063/1.555709

Pollack MG, Shenderov AD, Fair RB (2002) Electrowetting-based actuation of droplets for integrated microfluidics Lab on a Chip 2:96. https://doi.org/10.1039/b110474h

Pradhan TK, Panigrahi PK (2015) Deposition pattern of interacting droplets. Colloids and Surfaces A: Physicochemical and Engineering Aspects 482:562–567. https://doi.org/10.1016/j.colsurfa.2015.07.013

Pradhan TK, Panigrahi PK (2018) Convection inside condensing and evaporating droplets of aqueous solution. Soft Matter 14:4335–4343. https://doi.org/10.1039/C8SM00205C

Ray A, Varma VB, Jayaneel PJ, et al (2017) On demand manipulation of ferrofluid droplets by magnetic fields. Sensors and Actuators, B: Chemical 242:760–768. https://doi.org/10.1016/j.snb.2016.11.115

Rea U, McKrell T, Hu L, Buongiorno J (2009) Laminar convective heat transfer and viscous pressure loss of alumina–water and zirconia–water nanofluids. International Journal of Heat and Mass Transfer 52:2042–2048. https://doi.org/10.1016/j.ijheatmasstransfer.2008.10.025

Ristenpart WD, Kim PG, Domingues C, et al (2007) Influence of Substrate Conductivity on Circulation Reversal in Evaporating Drops. Physical Review Letters 99:234502. https://doi.org/10.1103/PhysRevLett.99.234502

Rosensweig RE (1984) Ferrohydrodynamics. Cambridge University Press 1985 279

Rosensweig RE (1988) An introduction to ferrohydrodynamics. Chemical Engineering Communications 67:1–18. https://doi.org/10.1080/00986448808940374

Roy G, Gherasim I, Nadeau F, et al (2012) Heat transfer performance and hydrodynamic behavior of turbulent nanofluid radial flows. International Journal of Thermal Sciences 58:120–129. https://doi.org/10.1016/j.ijthermalsci.2012.03.009

Roy T, Sinha A, Chakraborty S, et al (2009) Magnetic microsphere-based mixers for microdroplets. Physics of Fluids 21:027101. https://doi.org/10.1063/1.3072602

Saliba A-E, Saias L, Psychari E, et al (2010) Microfluidic sorting and multimodal typing of cancer cells in self-assembled magnetic arrays. Proceedings of the National Academy of Sciences 107:14524–14529. https://doi.org/10.1073/pnas.1001515107

Saroj SK, Panigrahi PK (2019) Drying pattern and evaporation dynamics of sessile ferrofluid droplet on a PDMS substrate. Colloids and Surfaces A: Physicochemical and Engineering Aspects 580:123672. https://doi.org/10.1016/j.colsurfa.2019.123672

Schneider CA, Rasband WS, Eliceiri KW (2012) NIH Image to ImageJ: 25 years of image analysis. Nature Methods 9:671–675. https://doi.org/10.1038/nmeth.2089

Sefiane K (2014) Patterns from drying drops. Advances in Colloid and Interface Science 206:372–381. https://doi.org/10.1016/j.cis.2013.05.002

Şeşen M, Tekşen Y, Şendur K, et al (2012) Heat transfer enhancement with actuation of magnetic nanoparticles suspended in a base fluid. Journal of Applied Physics 112:064320. https://doi.org/10.1063/1.4752729

Shaker M, Birgersson E, Mujumdar AS (2014) Extended Maxwell model for the thermal conductivity of nanofluids that accounts for nonlocal heat transfer. International Journal of Thermal Sciences 84:260–266. https://doi.org/10.1016/j.ijthermalsci.2014.05.010

Shamsi MH, Choi K, Ng AHC, Wheeler AR (2014) A digital microfluidic electrochemical immunoassay. Lab on a Chip 14:547–554. https://doi.org/10.1039/C3LC51063H

Shang L, Cheng Y, Zhao Y (2017) Emerging Droplet Microfluidics. Chemical Reviews 117:7964–8040. https://doi.org/10.1021/acs.chemrev.6b00848

Shuchi S, Sakatani K, Yamaguchi H (2005) An application of a binary mixture of magnetic fluid for heat transport devices. Journal of Magnetism and Magnetic Materials 289:257–259. https://doi.org/10.1016/j.jmmm.2004.11.073

Sing CE, Schmid L, Schneider MF, et al (2010) Controlled surface-induced flows from the motion of self-assembled colloidal walkers. Proceedings of the National Academy of Sciences 107:535–540. https://doi.org/10.1073/pnas.0906489107

Singh D, Shyam S, Mehta B (2019) Heat Transfer Characteristics of Ferrofluidic Flow Between Parallel Plates Under the Influence of Static and Transient Magnetic Field. In: Proceeding of Proceedings of the 24th National and 2nd International ISHMT-ASTFE

Heat and Mass Transfer Conference (IHMTC-2017). Begellhouse, Connecticut, pp 43–48

Sommers AD, Yerkes KL (2010) Experimental investigation into the convective heat transfer and system-level effects of Al2O3-propanol nanofluid. Journal of Nanoparticle Research 12:1003–1014. https://doi.org/10.1007/s11051-009-9657-3

Souza PJ, Lira SHA, de Oliveira IN (2019) Wetting dynamics of ferrofluids on substrates with different hydrophilicity behaviors. Journal of Magnetism and Magnetic Materials 483:129–135. https://doi.org/10.1016/j.jmmm.2019.03.069

Stauber JM, Wilson SK, Duffy BR, Sefiane K (2014) On the lifetimes of evaporating droplets. Journal of Fluid Mechanics 744:R2. https://doi.org/10.1017/jfm.2014.94

Stefan Odenbach (2006) Magnetoviscous Effects in Ferrofluids

Strek T (2008) Finite Element Simulation of Heat Transfer in Ferrofluid. In: Modelling and Simulation. I-Tech Education and Publishing

Tan S-H, Nguyen N-T, Yobas L, Kang TG (2010) Formation and manipulation of ferrofluid droplets at a microfluidic T -junction. Journal of Micromechanics and Microengineering 20:045004. https://doi.org/10.1088/0960-1317/20/4/045004

Tice JD, Song H, Lyon AD, Ismagilov RF (2003) Formation of Droplets and Mixing in Multiphase Microfluidics at Low Values of the Reynolds and the Capillary Numbers. Langmuir 19:9127–9133. https://doi.org/10.1021/la030090w

Ting TH, Yap YF, Nguyen N-T, et al (2006) Thermally mediated breakup of drops in microchannels. Applied Physics Letters 89:234101. https://doi.org/10.1063/1.2400200

Tsai T-H, Liou D-S, Kuo L-S, Chen P-H (2009) Rapid mixing between ferro-nanofluid and water in a semi-active Y-type micromixer. Sensors and Actuators A: Physical 153:267–273. https://doi.org/10.1016/j.sna.2009.05.004

Tuckerman DB, Pease RFW (1981) High-performance heat sinking for VLSI. IEEE Electron Device Letters 2:126–129. https://doi.org/10.1109/EDL.1981.25367

Varma VB, Ray A, Wang ZMP, et al (2016) Droplet Merging on a Lab-on-a-Chip Platform by Uniform Magnetic Fields. Scientific Reports 6:37671. https://doi.org/10.1038/srep37671

Velev OD, Bhatt KH (2006) On-chip micromanipulation and assembly of colloidal particles by electric fields. Soft Matter 2:738. https://doi.org/10.1039/b605052b

Vilfan M, Potočnik A, Kavčič B, et al (2010) Self-assembled artificial cilia. Proceedings of the National Academy of Sciences 107:1844–1847. https://doi.org/10.1073/pnas.0906819106

Walsh PA, Egan VM, Walsh EJ (2010) Novel micro-PIV study enables a greater understanding of nanoparticle suspension flows: nanofluids. Microfluidics and Nanofluidics 8:837–842. https://doi.org/10.1007/s10404-009-0553-z

Wang X-Q, Mujumdar AS (2007) Heat transfer characteristics of nanofluids: a review. International Journal of Thermal Sciences 46:1–19. https://doi.org/10.1016/j.ijthermalsci.2006.06.010

Wang Y, Zhe J, Chung BTF, Dutta P (2008) A rapid magnetic particle driven micromixer. Microfluidics and Nanofluidics 4:375–389. https://doi.org/10.1007/s10404-007-0188-x

Washizu M (1998) Electrostatic actuation of liquid droplets for micro-reactor applications. In: IAS '97. Conference Record of the 1997 IEEE Industry Applications Conference Thirty-Second IAS Annual Meeting. IEEE, pp 1867–1873

Wen C-Y, Liang K-P, Chen H, Fu L-M (2011) Numerical analysis of a rapid magnetic microfluidic mixer. Electrophoresis 32:3268–3276. https://doi.org/10.1002/elps.201100254

Wen C-Y, Yeh C-P, Tsai C-H, Fu L-M (2009) Rapid magnetic microfluidic mixer utilizing AC electromagnetic field. Electrophoresis 30:4179–4186. https://doi.org/10.1002/elps.200900400

Wen D, Ding Y (2004) Experimental investigation into convective heat transfer of nanofluids at the entrance region under laminar flow conditions. International Journal of Heat and Mass Transfer 47:5181–5188. https://doi.org/10.1016/j.ijheatmasstransfer.2004.07.012

White AK, Heyries KA, Doolin C, et al (2013) High-Throughput Microfluidic Single-Cell Digital Polymerase Chain Reaction. Analytical Chemistry 85:7182–7190. https://doi.org/10.1021/ac400896j

Wi HS, Cingarapu S, Klabunde KJ, Law BM (2011) Nanoparticle Adsorption at Liquid–Vapor Surfaces: Influence of Nanoparticle Thermodynamics, Wettability, and Line Tension. Langmuir 27:9979–9984. https://doi.org/10.1021/la201791g

Wright B, Thomas D, Hong H, et al (2007) Magnetic field enhanced thermal conductivity in heat transfer nanofluids containing Ni coated single wall carbon nanotubes. Applied Physics Letters 91:173116. https://doi.org/10.1063/1.2801507

Wu Y, Fu T, Ma Y, Li HZ (2013) Ferrofluid droplet formation and breakup dynamics in a microfluidic flow-focusing device. Soft Matter 9:9792. https://doi.org/10.1039/c3sm51860d

Xing S, Harake RS, Pan T (2011) Droplet-driven transports on superhydrophobic-patterned surface microfluidics. Lab on a Chip 11:3642. https://doi.org/10.1039/c1lc20390h

Xu R (2002) Particle Characterization: Light Scattering Methods. Kluwer Academic Publishers, Dordrecht

Xu W, Leeladhar R, Kang YT, Choi C-H (2013) Evaporation Kinetics of Sessile Water Droplets on Micropillared Superhydrophobic Surfaces. Langmuir 29:6032–6041. https://doi.org/10.1021/la400452e

Xuan Y, Li Q, Ye M (2007) Investigations of convective heat transfer in ferrofluid microflows using lattice-Boltzmann approach. International Journal of Thermal Sciences 46:105–111. https://doi.org/10.1016/j.ijthermalsci.2006.04.002

Yang J, Park J, Lee J, et al (2007) Motions of magnetic nanosphere under the magnetic field in the rectangular microchannel. Journal of Magnetism and Magnetic Materials 317:34–40. https://doi.org/10.1016/j.jmmm.2007.04.008

Yarahmadi M, Moazami Goudarzi H, Shafii MB (2015) Experimental investigation into laminar forced convective heat transfer of ferrofluids under constant and oscillating magnetic field with different magnetic field arrangements and oscillation modes. Experimental Thermal and Fluid Science 68:601–611. https://doi.org/10.1016/j.expthermflusci.2015.07.002

Yunker PJ, Still T, Lohr MA, Yodh AG (2011) Suppression of the coffee-ring effect by shape-dependent capillary interactions. Nature 476:308–311. https://doi.org/10.1038/nature10344

Zhang Y, Nguyen N-T (2017) Magnetic digital microfluidics – a review. Lab on a Chip 17:994–1008. https://doi.org/10.1039/C7LC00025A

Zhang Y, Park S, Liu K, et al (2011) A surface topography assisted droplet manipulation platform for biomarker detection and pathogen identification. Lab on a Chip 11:398–406. https://doi.org/10.1039/C0LC00296H

Zhu G-P, Hejiazan M, Huang X, Nguyen N-T (2014) Magnetophoresis of diamagnetic microparticles in a weak magnetic field. Lab on a Chip 14:4609–4615. https://doi.org/10.1039/C4LC00885E

Zhu G-P, Nguyen N-T (2012) Rapid magnetofluidic mixing in a uniform magnetic field. Lab on a Chip 12:4772. https://doi.org/10.1039/c2lc40818j

Zhu T, Lichlyter DJ, Haidekker MA, Mao L (2011) Analytical model of microfluidic transport of non-magnetic particles in ferrofluids under the influence of a permanent magnet. Microfluidics and Nanofluidics 10:1233–1245. https://doi.org/10.1007/s10404-010-0754-5

Appendix A

INSTRUMENTATION

A.1. DETAILS OF IR CAMERA

Table A.1. Details of infrared camera.

Detector type	Uncooled microbolometer
Dynamic range	16 bit
Resolution	640 × 480
Optional temperature range	Up to 2000°C
Operational temperature range	-15°C to 50°C
Storage temperature range	-40°C to 70°C
Weight	0.92 kg
NETD (Noise equivalent temperature difference)	<30 ms
Frame rate (full window)	50 Hz
Maximum frame rate (at minimum window)	200 Hz (640×120)
Spectral range	7.5 – 14.0 µm
Time constant	<8 ms
Power	12/24 VDC, 24 W Absolute Max
Command and control	USB, Gigabit Ethernet, RS-232
Data	Gigabit Ethernet - Digital Camera Link - Digital Composite (BNC) - Analog Grayscale Video (NTSC or PAL)

A.2. UNCERTAINTY IN TEMPERATURE READINGS

In the present investigation the single sample analysis as proposed by Moffat (1988) are applied to the experimental data's. Considering a general case, let R be the result and it is a function of 'n' independent variables, X_i such that,

$$R = R(X_1, X_2, X_3, X_4, \dots\dots\dots\dots X_n) \quad \text{(A.1)}$$

X_i is the measured variable of the experiments. Then the existing uncertainties in the experimental results can be expressed as

$$U_R = \left\{ \sum_{i=1}^{i=n} \left(U_{X_i} \frac{\partial R}{\partial X_i} \right)^2 \right\}^{1/2} \quad \text{(A.2)}$$

U_{X_i} is the uncertainty of the measured quantity X_i and each term in the Eq. (A.2) represents the contribution in uncertainties on the overall results by each measured variable.

The heat power supplied to the system is calculated by measuring the electrical power delivered to the system as given by

$$\dot{Q} = V \cdot I \quad \text{(A.3)}$$

$$\frac{\delta \dot{Q}}{\dot{Q}} = \left\{ \left(\frac{\delta V}{V} \right)^2 + \left(\frac{\delta I}{I} \right)^2 \right\}^{1/2} \quad \text{(A.4)}$$

The heat transfer coefficient (h) is calculated as

$$h = q''/(T_w - T_f) \quad \text{(A.5)}$$

The Nusselt number (Nu) is calculated as

$$Nu = h \cdot D_h / k_f \quad \text{(A.6)}$$

Therefore, the uncertainty in the heat transfer coefficient is given by

$$\frac{\delta h}{h} = \left\{ \left(\frac{\delta \Delta T}{\Delta T} \right)^2 + \left(\frac{\delta q''}{q''} \right)^2 \right\}^{1/2} \quad \text{(A.7)}$$

Where $\Delta T = T_w - T_f$ and $\delta(\Delta T) = \left\{ (\delta T_w)^2 + \left(\delta T_f \right)^2 \right\}^{1/2}$

A.3. UNCERTAINTY IN VELOCITY READINGS

Errors in μPIV measurement may occur due to several reasons such as density difference between the seeded tracer particles and the fluid, Brownian motion of the particles. The density difference between the seeded particles and the bulk liquid, may cause settling of the tracer particles. Consequentially the tracer particles may incur a settling velocity as given by $U_g = d_p^2 (\rho_p - \rho) g / 18\mu$, where ρ is the density of the liquid, ρ_p is the density of the tracer particles, d_p is the diameter of the seeded particles (Pitzer et al. 1984). In the present

investigations the settling velocity of the seeded particles was found to be $\sim 10^{-8}$, and is therefore ignored. While the errors due to Brownian motion of the seeded particles can be reduced by averaging the results over several measurements. In this study, the μPIV experiments were repeated four times and the mean of these values were taken as the final result. For the present investigation the maximum uncertainty was found to be around 8%.

A.4. THERMOCOUPLE CALIBRATION

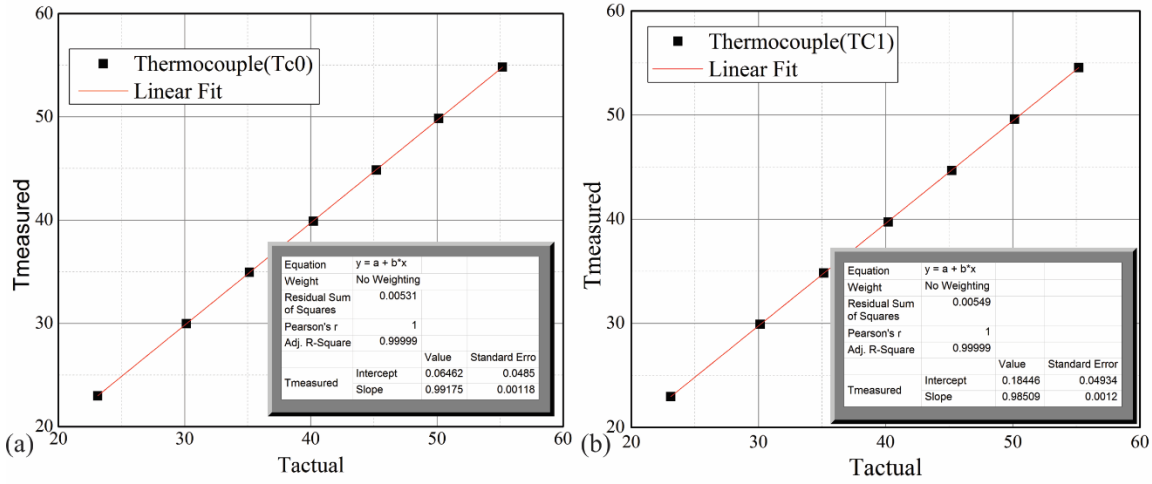

Fig. A.1 Calibration curve for thermocouples.

Appendix B

MAGNETIC FIELD DISTRIBUTION

B.1. THREE DIMENSIONAL MAGNETIC FIELD DISTRIBUTION

The governing equation describing the distribution of the magnetic field is based on the Ampere's law, which for a static case can be written as (Griffiths and Inglefield 2005):

$$\nabla \times \bar{H} = \bar{J} \tag{B.1}$$

where $\bar{H}$ is the magnetic field intensity, $\bar{J}$ is the current density which is given by (Griffiths and Inglefield 2005),

$$\bar{J} = \sigma(\bar{u}_c \times \bar{B}) + \bar{J}_e \tag{B.2}$$

$\bar{u}_c$ is the velocity of the conductor and $\bar{J}_e$ is the externally generated current density. This externally generated current density is given by $\bar{J}_e = (N\bar{I}/a_{coil})$, where N is the number of turns, $\bar{I}$ is the supplied current and a_{coil} is the cross-sectional area of the wire. Now, using magnetic scaler potential $\bar{A}_m$, the magnetic field flux can be written as

$$\bar{B} = \nabla \times \bar{A}_m \tag{B.3}$$

Employing the constitutive relationship $\bar{B} = \mu_0(\bar{H} + \bar{M})$; where $\bar{M}$ is the magnetization, the Ampere's law can be rewritten as

$$\sigma(\partial \bar{A}_m/\partial t) + \nabla \times (\mu_0^{-1} \cdot \mu_r^{-1} \cdot \bar{B}) - \sigma \bar{u}_c \times \bar{B} = \bar{J}_e \tag{B.4}$$

Note that μ_0 and μ_r in equation (B.4) are the permeability of the vacuum and the relative permeability, respectively. While solving the aforementioned equations, we use the tangential component of the magnetic potential ($\mathbf{n} \times \bar{A}_m = 0$) is zero at the boundary of the domain. The governing equations are solved in the finite element framework of COMSOL Multiphysics®. The parametric values considered for the present computations are as follows: $\bar{I} = 1.2A$, $a_{coil} = 2.82 \times 10^{-5} m^2$, $\mu_0 = 1.257 \times 10^{-6}\, H/m$ (Henry/meter), $\mu_r = 1$. Figure B.1 shows the magnetic field distribution in the ferrofluid droplet domain according to the experimental framework used in Chapter 5. Similarly Fig. B.2. shows the magnetic field distribution in the sessile ferrofluid droplet domain in accordance with the experimental arrangement as mentioned in Chapter 6.

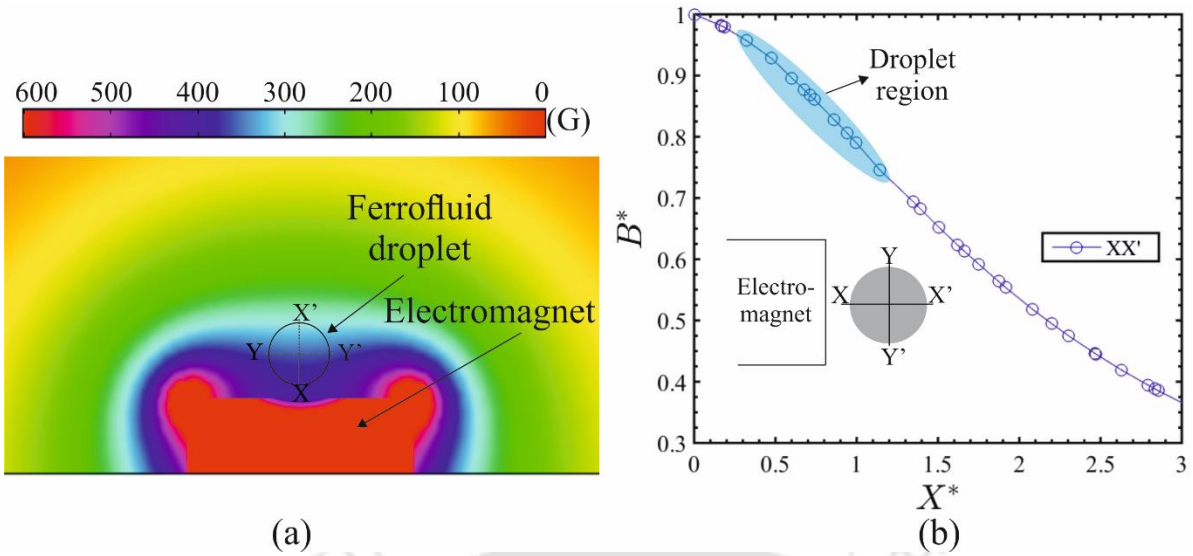

Fig. B.1. (a) Plot shows the distribution of magnetic flux density $(\bar{B})$ around the droplet region. The black circle denotes the ferrofluid droplet. $X - X'$ and $Y - Y'$ indicates the symmetric lines inside the ferrofluid droplet domain. (b) Plot depicts the variation of magnetic flux density $(\bar{B})$ along the $X - X'$ line of symmetry of the droplet. The blue-marked region denotes the droplet flow field area. The position $X = 0, Y = 0$ signifies the center of the droplet. The schematic in the inset denotes the electromagnet and the droplet assembly along with the line of symmetry. $B^* = \bar{B}/\bar{B}_0$, where $\bar{B}_0$ is the magnetic field flux density at the electromagnet surface. $X^* = X/D$, where D is the diameter of the ferrofluid droplet.

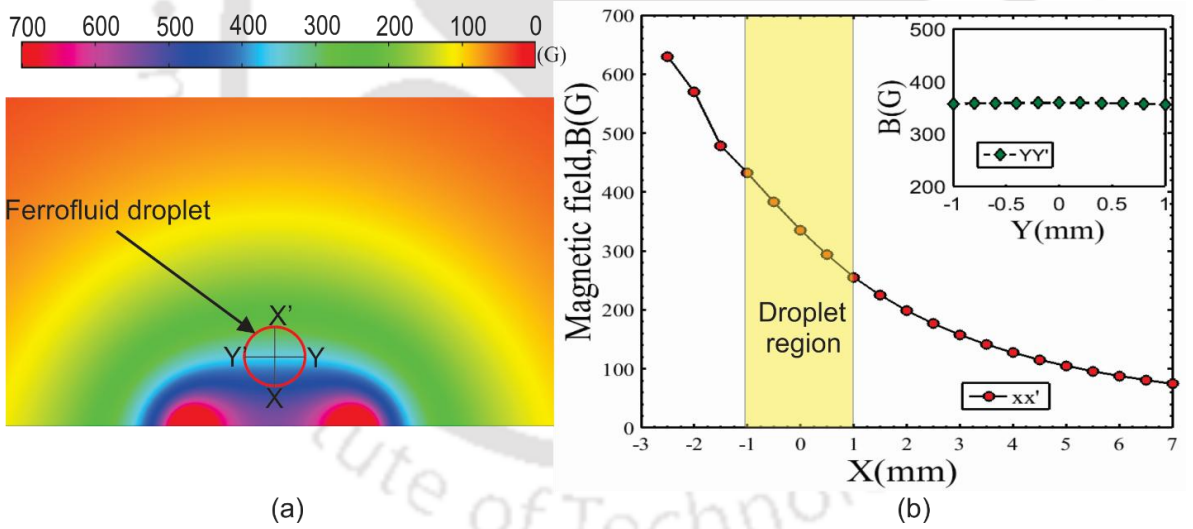

Fig. B.2. (a) The plot shows the distribution of magnetic flux density$(\bar{B})$ around the droplet region. The red circle denotes the ferrofluid droplet. $X - X'$ and $Y - Y'$ indicates the symmetric lines inside the ferrofluid droplet domain. (b) Plot depicts the variation of magnetic flux density $(\bar{B})$ along the $X - X'$ line of symmetry of the droplet. The yellow marked region denotes the droplet flow field. The inset shows the magnetic flux density variation along the $Y - Y'$. The position $X = 0, Y = 0$ signifies the center of the droplet.

LIST OF PUBLICATIONS

Journals

- **S. Shyam**, B. Mehta, P.K. Mondal, S. Wongwises, Investigation into the thermo-hydrodynamics of ferrofluid flow under the influence of constant and alternating magnetic field by infraRed thermography, **International Journal of Heat and Mass Transfer**, 135 (2019) 1233–1247. https://doi.org/10.1016/j.ijheatmasstransfer.2019.02.050.
- **S. Shyam**, M. Asfer, B. Mehta, P.K. Mondal, Z.A. Almutairi, Magnetic field driven actuation of sessile ferrofluid droplets in the presence of a time dependent magnetic field**, Colloids and Surfaces A: Physicochemical and Engineering Aspects**, (2020) 124116. https://doi.org/10.1016/j.colsurfa.2019.124116.
- **S. Shyam**, P.K. Mondal, B. Mehta, Field driven evaporation kinetics of a sessile ferrofluid droplet on a soft substrate, **Soft Matter**, 16 (2020) 6619–6632. https://doi.org/10.1039/D0SM00345J
- **S. Shyam**; P. K. Mondal, B. Mehta, Magnetofluidic mixing of a ferrofluid droplet under the influence of time-dependent external field, **Journal of Fluid Mechanics, (**2021**)** (Accepted for publication). DOI: :10.1017/jfm.2021.245

Conferences

- **S. Shyam**, B. Mehta, P.K. Mondal, Thermohydrodynamics of ferrofluidic flow with periodic pulsation under the effect of static and alternating magnetic field-: A numerical study, *16th International Heat Transfer Conference (IHTC), 10-15 August, 2018, Beijing, China, Paper no. IHTC16-23439.*
- **S. Shyam**, B. Mehta, P.K. Mondal, M. Asfer, Internal flow dynamics of ferrofluid droplet under the influence of magnetic field, *25th National and 3rd International ISHMT-ASTFE Heat and Mass Transfer Conference (IHMTC), 28-31 December, 2019, IIT Roorkee, India, Paper no. IHMTC2019-MPF-769.*